UNIVERSITY OF OKLAHOMA

GRADUATE COLLEGE

THEORY, DESIGN, AND FABRICATION OF FREQUENCY AGILE FILTENNAS

A THESIS

SUBMITTED TO THE GRADUATE FACULTY

in partial fulfillment of the requirements for the

Degree of

MASTER OF SCIENCE

By

MARC THIBODEAU
Norman, Oklahoma
2020

THEORY, DESIGN, AND FABRICATION OF FREQUENCY AGILE FILTENNAS

A THESIS APPROVED FOR THE
SCHOOL OF ELECTRICAL AND COMPUTER ENGINEERING

BY THE COMMITTEE CONSISTING OF

Dr. Hjalti Sigmarsson, Chair

Dr. Jessica Ruyle

Dr. Shahrokh Saeedi

Acknowledgements

I would not have been able to learn or achieve as much as I have over these past few years without the continued support of a small army of people. First and foremost, my advisor, Dr. Hjalti Sigmarsson, has been invaluable. He has entertained countless questions, brainstorming sessions, and wild ideas. I have greatly enjoyed and appreciated our technical discussions, not-so-technical discussions, and his advice along the way. I have undoubtedly become a better researcher and been prepared for my future steps due to his influence.

I would also like to thank the other two members of my committee, Dr. Jessica Ruyle and Dr. Shahrokh Saeedi. Dr. Ruyle taught me about the strange world of antennas from scratch, including tolerating some eccentric questions that were far outside the bounds of traditional antenna theory. I have gained confidence in antenna design due to her help. Dr. Saeedi has also been a mentor to me throughout my time at the Advanced Radar Research Center (ARRC). He always made time to answer my questions and taught me so much about fabrication and measurement of microwave devices. His explanations were thorough yet easy to understand, and I have become better at the entire research process due to his mentorship.

I would also like to thank many current and former members of the ARRC. These include other professors who have offered their expertise to help me understand different aspects of my thesis, but also many other students. The open nature of the ARRC has helped me tremendously, allowing me to freely bounce my ideas off of others and gain valuable insights. I would like to thank Dr. Nathan Goodman, Dr. Jay McDaniel, Chris

Walker, Clayton Blosser, Eivy Arroyo Diaz, Stephen Bass, Paul Winniford, Nick Peccarelli, Ashley Palmer, Garrett Robinson, Alex Pham, and Andrew Schaeffer for directly helping me in development of the content of my thesis. However, there are many others at the ARRC who have aided me, both professionally and otherwise, including Alex Moreno, Matthew Judy, William Clark, Russell Kenney, Jon Knowles, Rachel Jarvis, and so many others. The ARRC is truly a wonderful place to do spend multiple years doing research and I am grateful for the friends and experiences I've gained during my time here.

Finally, I would like to thank all of those who have supported me entirely non-academically. My friends from back home, my family, and the friends I made in Oklahoma have all been incredibly supportive and I am truly thankful that they are in my life. I am lucky to have friends and family that care as much as they do.

Table of Contents

List of Tables

List of Figures

Abstract

With the development of modern wireless systems, the spectral environment has become increasingly crowded. This has spawned a strong interest in frequency, bandwidth, and pattern reconfigurable RF front ends, which can adaptively tune their response to reduce interference. A filtenna ('filter' and 'antenna') is a device that combines an antenna and at least one other resonator together to achieve the same or better performance as an antenna and filter cascade in a smaller and lighter package. Most frequency reconfigurable filtennas tune by using microelectromechanical systems, pin diodes, or varactors. These tuning techniques are ill-suited for high power applications due to breakdown, non-linear effects, and/or high loss. These problems can be solved by the use of mechanical tuning. In this thesis, a piezoelectric actuator tuned, 2nd order filtenna is presented. The design is based upon changing the capacitive loading of an antenna and an evanescent-mode cavity resonator, thereby altering the resonant frequency. Loading agility is achieved through physical displacement of a metal disk. A time domain based tuning method is applied to tune the filtenna, allowing highly accurate tuning with only access to S_{11}. The filtenna is simulated to have a 2nd order response and tune across S-band (2-4 GHz, 2:1 ratio). Simulations also show a greater than 65% radiation efficiency and greater than 3 dBi broadside gain throughout the entire tuning range. This filtenna demonstrates the feasibility of a widely tunable, highly linear, and compact front end for modern RF systems, as well as a design methodology to allow for future development of frequency agile filtennas.

Chapter 1

Introduction

1.1 Overview

Modern RF systems must deal with increasingly dense and crowded spectral environment. This demand is universal across application, but the supply is inherently limited, since spectrum is a finite resource. This demand for efficient use of spectrum has pushed operational bands closer. Additionally, interferers can appear in a system. They can take the form of another broadcaster in a neighboring band having excessive spectral leakage, another legitimate transmitter drowning out the desired signal (such as many devices trying to connect to a single Wi-Fi router), or malicious transmitters attempting to disrupt communication. This overcrowding and interference problem has increased the prevalence of multi-band systems, allowing a user to switch channels and still operate effectively. All of these new use cases have demanded better performing and agile RF elements. A sample of the frequency allocations for S-band (2-4 GHz) is shown in Figure 1.1, showing how many different technologies are competing for spectrum usage.

Traditionally, a high performance RF system consists of a wideband antenna on the front end with a filter bank behind the antenna to reject any unwanted signals. To accommodate bands operating closer together, typically the order of the filters was increased, requiring more resonators and more space and weight to accommodate those resonators.

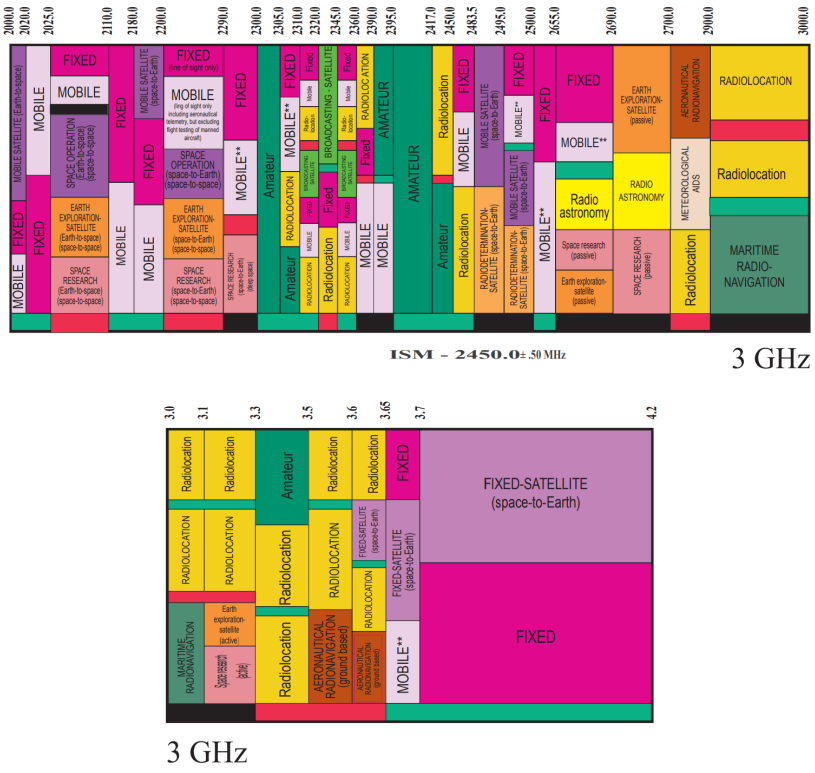

Figure 1.1: Frequency allocations for S-band (2-4 GHz) showing how many users are competing for close and overlapping bands. Adapted from [1].

Adding multi-band operation requires the antenna to cover all of the bands and the creation of a switchable filter bank, where the system would have a high order filter for each band of operation and the user would switch between each to look at the frequency of interest. This again increases size and weight requirements, but also increases power requirements due to the control system needed.

All of these additions would be acceptable, but there is also a constant demand for decreases in Size, Weight, and Power (SWaP) for all use cases. In cases such as satellite applications where space is at a premium, power needed is driven by solar (which has its own SWaP requirements), and each additional *gram* costs a minimum of $1.40 [2], it can be seen how much SWaP matters. To address SWaP concerns, many antenna and filter technologies today are incorporated into printed circuit board (PCB) design processes, but

the requirement for smaller and lighter systems still stands. If there were some way to reduce the number of elements required, but maintain PCB manufacturability, that would fundamentally decrease the size and weight requirements of a system and be a desirable technology.

1.2 Reconfigurable Filters

One attractive solution to the filter bank issue is to make the filters reconfigurable. A single filter can simply be tuned to operate in different bands, replacing the large bank of filters with a single tunable filter. If this tunability is fine enough, a tunable filter can provide more agility than any realizable filter bank. While there are increases in complexity and sometimes power consumption to make a filter tunable, the savings on size and weight make a single filter system a highly appealing option. Tunability is normally accomplished through strategic loading of the structure with an adjustable complex impedance. This adjustable impedance, or loading element, causes a corresponding change in frequency response of the device. Unfortunately, tunability normally comes at the sacrifice of other parameters. Quality factor, and therefore insertion loss, can suffer as the loading elements contribute loss. Power handling can also decrease since many loading elements (varactors, ferrites, etc.) cannot handle large amounts of power without experiencing non-linearities, degradation in performance due to thermal effects, or complete failure [3].

One promising technology that offers balanced performance and tunability is the tunable evanescent-mode cavity based filter. An evanescent-mode cavity is a cavity resonator that is loaded in such a way that it operates well below the resonant frequency one would expect from the outer dimensions. The lowest frequency possible in a traditional cavity is the frequency with an effective wavelength twice that of the largest dimension [5]. This creates a 'half-wavelength' resonator within the cavity. Evanescent-mode cavities exploit

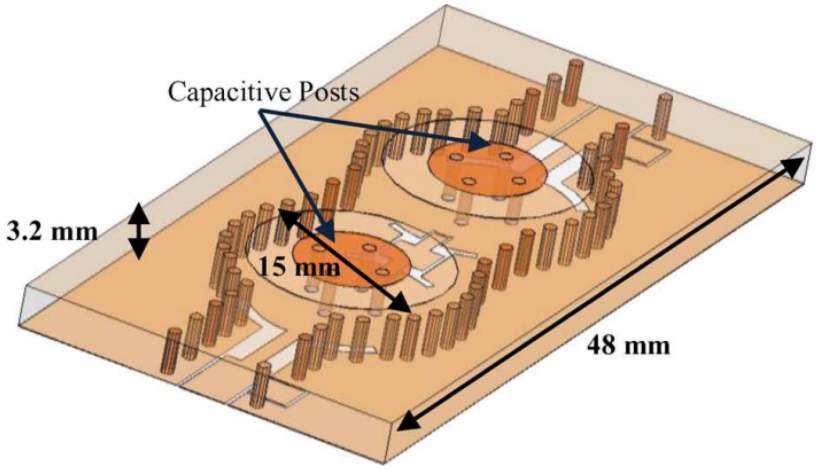

Figure 1.2: Tunable evanescent-mode cavity based filter from [4].

loading of the cavity, typically with a capacitive post, to lower the resonant frequency. This enables the resonator to fit in a much smaller package. Evanescent-mode cavities provide a balance between high tunability [6], high power handling [7], high Q [4], [8], [9], high linearity, low power consumption, and small size that make them a good candidate for high-performance microwave systems. They can be implemented as metal wall cavities, but they can also be integrated into substrates, making manufacturing and inclusion into overall systems much simpler [10]. An example of a 2^{nd} order, substrate integrated, tunable filter from [4] is shown in Figure 1.2.

There has been extensive work done to model the performance of evanescent-mode cavities [11] and they have been used in complex filter designs [12]. Linearity is not sacrificed despite the wide tuning range, as the cavities can be tuned mechanically. They have also been demonstrated to handle at least tens of Watts while maintaining high tunability [7]. The common method of tuning these resonators using piezoelectric actuators demands little power to tune and practically zero power to maintain position.

Thus, evanescent-mode cavities open the door for replacement of filter banks with a single tunable filter. This new filter would be able to maintain high performance while

improving significantly on traditional levels of SWaP. However, despite this drastic improvement, there are still strides to be made.

1.3 Reconfigurable Antennas

An additional improvement to the SWaP problem of the broadband antenna plus filter bank idea is to make the antenna itself reconfigurable. Using a narrowband antenna offers a better noise figure performance [5] and includes a 'filtering' element at the very front end of the device, reducing the required filter order to accomplish the same rejection characteristics. To cover multiple bands, however, the antenna must be reconfigurable in frequency. This system aims to save on SWaP by reducing the order required for each filter in the bank; it does not eliminate the need for a filter bank itself.

There has been much research on reconfigurable antenna designs, with many focusing on adaptive antenna loading as a tuning mechanism. Common loading mechanisms include varactors [13], [14], microelectromechanical systems (MEMS) [15], and pin diodes [16]–[18]. Figure 1.3 shows a varactor tuned slot antenna from [13]. While these systems offer many benefits when it comes to reliability, incorporation into current PCB design processes, size, and weight, they suffer in one key region: power handling. Their physical properties cause serious limitations due to breakdown and undesirable non-linear effects. These effects have limited the adoption of these highly adaptive antennas in high power applications like radar. Next generation systems need to operate in narrow frequency bands without risking spectrum pollution due to non-linearities. Mechanical actuation of metal offers a combination of linearity, power handling, and tuning range that is difficult to find in other tuning methods.

Tuning using movement of metal has been around since the earliest days of radio [19]. It has been reliably used in systems such as radios, radars, and telecommunications. Fac-

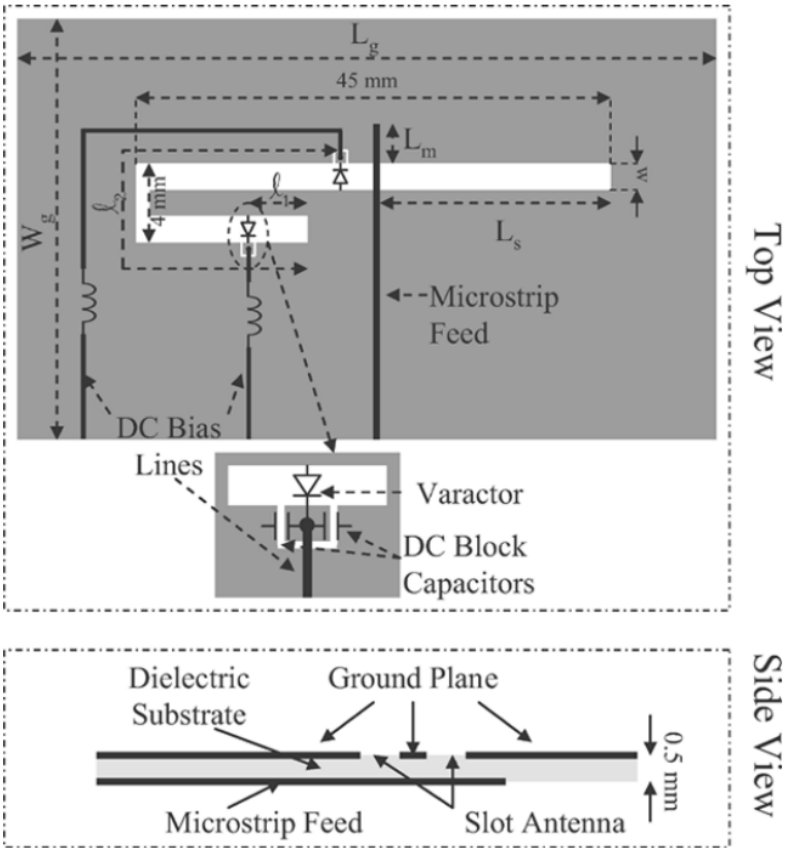

Figure 1.3: Tunable multi-band slot antenna tuned by varactors from [13].

tory mechanical tuning is currently commonplace in microwave components, such as using screws for fine tuning of new cavity filters [5]. For many decades, active, electrically controlled, mechanical tuning has been well established in the higher frequency domain of microwave components. Work has largely focused on the use of piezoelectric discs or rotating cam shafts with stepper motors as a movement mechanism. Both offer precise control of movement, power handling, and spurious frequency rejection benefits [4], [8], [9], [20]. Unfortunately, cam shaft actuation requires complex construction and, for antenna applications, requires large rotating pieces directly over the antenna. The piezoelectric discs have a fairly small deflection distance and therefore are limited to high loading applications to cause large changes in capacitance. The piezoelectric discs consist of a piezoelectric crys-

tal and a nickel alloy coating. Both of those materials are lossy, preventing the effective use of piezoelectric discs in areas of high field density without serious impacts on efficiency due to ohmic losses.

Recent advancements in piezoelectric actuators, which use multiple piezoelectric crystals stacked up and active feedback loops in a single package, have partially solved these problems. They allow for comparable degrees of control to piezoelectric discs but with much greater deflection distances. These actuators can often cover millimeter distances with micrometer accuracy, allowing for much larger deflection than is possible with a single piezo disc while maintaining precise control. For example, the M3-L Micro Linear Actuator by New Scale Technologies can move up to 6 mm along an axis in 0.5 μm steps, Another key aspect is that the actuator itself is far away from the antenna, distancing it from the strongest fields and thereby reducing loss and radiation disturbance.

With these steps in reconfigurable antenna design, there can be further improvement in SWaP while maintaining desirable radiation efficiency, antenna pattern, and linearity. The combination of a tunable filter and a tunable antenna is already a drastic improvement from a wideband antenna and filter bank, but there is yet another step that can be taken.

1.4 Reconfigurable Filtennas

With traditional antenna plus filter bank systems, the antenna is often treated as a separate entity, bolted on and entirely disjoint from the filter system. Therefore, to get a desired frequency response there are limits to SWaP, since the size of antennas and filters positively correlating with gain, power handling, and tunability. Therefore it becomes difficult to shrink the system and maintain a certain level of performance. Additionally, the transmission line in between the antenna and filter bank inherently adds noise to the system. A particular element will tend to have a larger effect on the signal the earlier it is in the receive

chain, meaning the transmission line can influence the performance significantly [5]. The impact of the transmission line can vary widely with the length or geometry of the line, but the potential for impact is quite large in systems where the antenna is separated far from the filters.

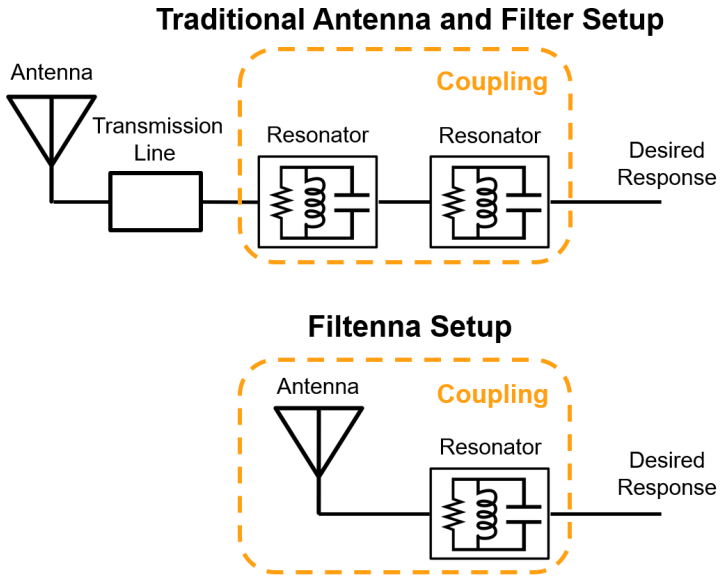

Figure 1.4: Block diagram comparing a traditional 2nd order receive chain to a filtenna 2nd order receive chain

Filtennas (a portmanteau of 'filter' and 'antenna') can offer several unique advantages over the traditional treatment of antennas and filters as separate entities. For filtennas, the antenna is treated as another resonator in a filter block, where the fields of the antenna directly overlap and interact with the fields of the filter block. First and foremost, this allows for the removal of a resonator in the filter block while maintaining the same frequency response. Instead of a wide-band antenna and a second order filter, for example, a single antenna and a single resonator coupled together into a filtenna can provide that same second order filter response. This immediately promises improvements in SWaP. Additionally, the direct coupling of the antenna to the filter allows for the removal of a transmission line between the two systems, bringing them closer together, improving noise performance,

and again offering improvements in SWaP. The reduction from a traditional system to a filtenna is shown in Figure 1.4.

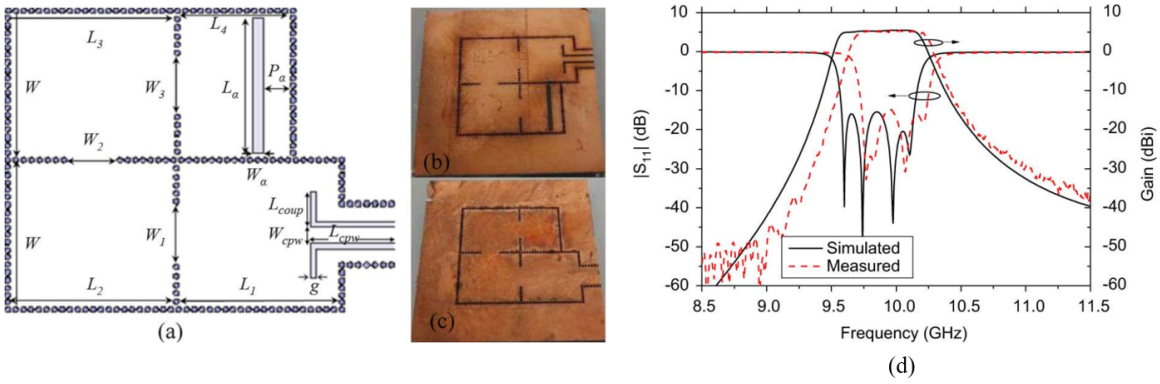

Figure 1.5: Multi-order filtenna found in [21]. Layout of filtenna (a), photograph of the slot antenna side (b) and coaxial feed side (c) with the simulated versus measured response seen in (d). See [21] for dimensions and further discussion.

Several avenues for the creation of filtennas have been pursued before. They have varied from introducing loading structure in horns to using leaky wave structures in cavity resonators [21]–[24]. Static filtenna have been demonstrated with as high as 4th order Chebyshev responses while maintaining high efficiency [21], demonstrating their capability as radiating and filtering structures. The 4th order filtenna layout and response is shown in Figure 1.5. Additionally, a time domain tuning method has been applied to tune these filtennas [21], [24]–[26], allowing for higher order tuning with only access to the input port. However, all of this work has been on static filtennas, and tunability is a key element in reducing SWaP.

Adding tunability to a filtenna allows a single tunable filtenna to perform the same function as an antenna and filter bank in a traditional design. There has been much published work on tunable 'filtennas', but much of the work published is only a tunable filter with an antenna attached to the end; there is no additional benefit to performance from coupling to the antenna [28]–[30]. Lovato has recently introduced a few true tunable filtennas, making use of varactor loading to load the elements [27], [31]. These filtennas are as high as 3rd

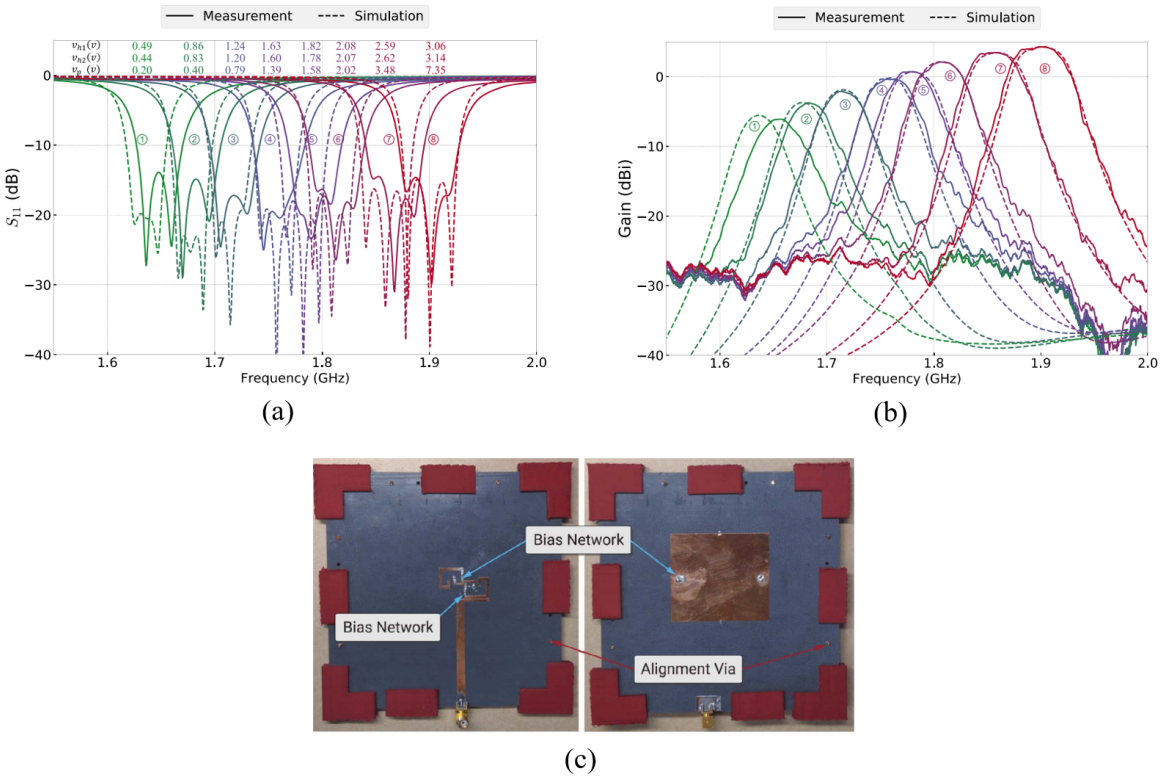

Figure 1.6: Multi-order, tunable, fixed bandwidth filtenna found in [27]. Measured and simulated S_{11} response (a), measured and simulated gain response (b) and image of tunable filtenna. See [27] for dimensions and further discussion.

order and have been demonstrated to have as high as a 1.68:1 tuning ratio. Lovato has additionally demonstrated bandwidth tunability within a frequency tunable filtenna, showing static bandwidth is possible [27]. This bandwidth and frequency reconfigurable filtenna is shown, along with results, in Figure 1.6. However, while impressive, all of these designs have relied on varactor tuning elements. These inherently limits the power handling, linearity, and efficiency of these devices, leading to low radiation efficiency and low gain at high loading. All of the filtennas demonstrated a maximum of -3 dBi gain at the lowest frequency, indicating low radiation efficiency. Due to the non-linear nature of the varactors, it is also likely that these filtennas would experience non-linear effects in higher power operation. This is to be expected since high power handling normally comes at the cost of

tunability. However, a filtenna with high power handling, full octave tunability, and comparable performance to a traditional antenna plus filter system would be a highly desirable technology. The goal of this thesis is to demonstrate a device capable of meeting those expectations.

1.5 Outline

This thesis aims to demonstrate methods of conceptualization, simulation, tuning, and fabrication of the elements of a high power handling, frequency reconfigurable filtenna. As such, it will be broken into several sections to cover the building blocks of the proposed filtenna.

Chapter 2 covers tunable evanescent-mode cavity theory, with a focus on modeling of the structure. Discussion of previous work and modeling will be presented, and an adjusted closed-form method for predicting the resonant frequency of the cavity will be shown to account for manufacturing techniques. An example cavity will be conceived, simulated, and fabricated, with results shown and discussed. The cavity will be shown to be able to tune across S-band (2-4 GHz), and maintain a high Q throughout the tuning range.

Chapter 3 focuses on the development and refinement of a highly tunable slot antenna. This antenna will be demonstrated to tune across S-band (2-4 GHz) while maintaining a good match and radiation efficiency. The conceptualization, simulation, and fabrication of the antenna will be presented with results discussed. The primary focus will be on how the tuning mechanism affects the performance of the base slot antenna used. Guidelines of tunability and radiation efficiency trends will also be discussed.

Chapter 4 goes into extensive detail about the time domain method used to tune a filtenna. In a traditional filter, both ports are accessible for information about the nature of the filter. In a filtenna, only one port is available. Given that a filtenna may be designed

to be a symmetric filter, this can create issues for determining which part in the multi-resonator system is mistuned. The time domain method provides a way to directly analyze the parameters of the filtenna and provide direct insight into how the device needs to be tuned.

Chapter 5 demonstrates the design methodology, tuning process, and simulated performance of a 2nd order filtenna. The chapter begins with a discussion of filter theory in general and how it can be applied to filtennas. Then, the tunable antenna is adapted to allow incorporation into a filtenna. Input coupling techniques and characterization, internal coupling design, and and output coupling is also discussed. Finally, using all of the tools presented, a filtenna is conceived and simulated. The filtenna is tuned to 3 GHz using the time domain method, and is shown to be able to tune across all of S-band (2-4 GHz). The performance across all of S-band is presented.

Chapter 6 provides a summary of work including scientific contributions. The chapter also discusses possible improvements to the design and suggestions of future paths for this research.

Chapter 2

Evanescent-Mode Cavity Theory

When designing high-performance microwave resonators, there are several competing factors at play. It is highly desirable to have high Q, arbitrary bandwidth, and high linearity. However, these factors often compete with requirements for size constraints, manufacturing ease, and low cost. Tunable resonators offer a partial solution to the problem, as they can provide a wide operational bandwidth without a full filter bank, but often at the sacrifice of Q, linearity, and power handling due to the tuning elements. Traditional cavity resonators allow for high Q, high linearity, and high power handling, but their size is often determined by the wavelength of the frequency being filtered. Therefore, a highly tunable cavity resonator with some way to limit size is a highly desirable technology. Evanescent-mode SIW cavities provide an excellent balance between high tunability [6], high power handling [7], high Q [4], [8], [9], high linearity, and small size that make them an excellent candidate for this role. For these reasons, substrate integrated waveguide (SIW) evanescent-mode cavities were chosen for this project.

In order to fully make use of evanescent-mode cavities, full characterization is necessary to understand and predict the resonant frequency and quality factor of the cavity. Ideally, derivation of the resonant frequency would be possible from closed-form, simple expressions. This will be shown to be possible with some limitations. Quality factor derivation has been covered in previous work [12]. Expansion of models for quality fac-

tor to dielectric stacks was not done in this thesis, but would be a valuable path for future research. Next, characterization using full-wave solvers will be used to gain further insight. Lastly, the results of a manufactured evanescent-mode cavity will be compared to simulation and theory to demonstrate the robustness of each.

2.1 Evanescent-Mode Cavity Closed-Form Modeling

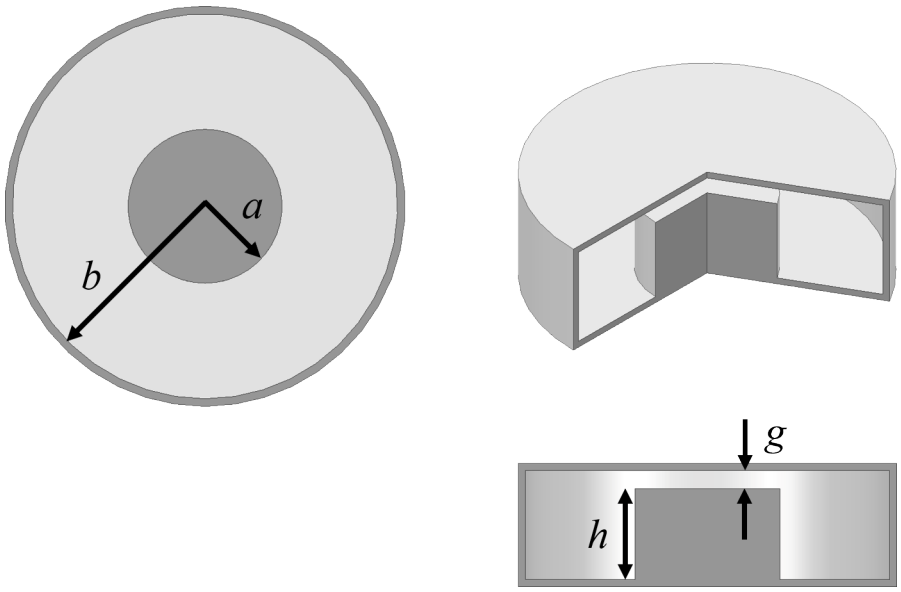

Figure 2.1: Cutaway simplified model of an evanescent-mode cavity resonator. The walls are a good conductor and it is assumed to be vacuum filled

It is useful to be able to predict the operational frequency of an evanescent-mode cavity given the physical dimensions. This predictive power can drastically increase the speed of the design process. A simplified evanescent-mode cylindrical cavity consists of only a few parts. An outer cylindrical cavity with radius b houses a concentric post, itself having a radius a. The post reaches a height of h and forms a gap with the interior of the cavity of size g. Therefore, the height of the interior of the cavity is $h + g$. The general dimensions

used to describe a cylindrical evanescent-mode cavity are shown in Figure 2.1. In general, many single resonators can be approximated as LC resonators. The resonant frequency of an LC resonator is known to be

$$f_0 = \frac{1}{2\pi\sqrt{LC}}, \tag{2.1}$$

where f_0 is the resonant frequency, L is the inductance, and C is the capacitance. The difficulty lies in finding what values to use for inductance and capacitance. Previous work has looked into the various models that may be used to predict these resonant frequencies [12]. The three main models given were a loaded coaxial line (LCL) model, a lumped element model (LEM), and a Green's function (GF) based model from a paper by Fujisawa [11]. All of these models rely on the assumption that $g << h$ to maintain accuracy. Note that this work will initially be dealing with comparing the predictions of the models, not derivation of the models themselves; see [12] for more detail. The LCL model predicts the resonant frequency as

$$f_0 = \frac{c_0}{\pi\sqrt{2a^2\left(\frac{h}{g}\right)\ln\left(\frac{b}{a}\right)}}, \tag{2.2}$$

where c_0 represents the speed of light in a vacuum, a is the radius of the post, h is the height of the first substrate/post, g is the size of the gap, and b is the radius of the cavity, as shown in Figure 2.1. There is technically another LCL model in [12], but it returns more similar results to the one presented here as g becomes a smaller fraction of h, so it is left out of this analysis due to the $g << h$ assumption.

The LEM gives the resonant frequency as a combination of lumped capacitances and an inductance in the cavity. The relations become

$$f_0 = \frac{1}{2\pi\sqrt{L_{coax}C_{tot}}}, \tag{2.3a}$$

$$L_{coax} = \frac{\mu_0 h}{2\pi} \ln\left(\frac{b}{a}\right), \tag{2.3b}$$

$$C_{tot} = C_{post} + C_{cavity} + C_{coax}, \tag{2.3c}$$

$$C_{post} = \frac{\varepsilon_0 \pi a^2}{g}, \tag{2.3d}$$

$$C_{cavity} = \frac{\varepsilon_0 \pi \left(b^2 - a^2\right)}{h + g}, \tag{2.3e}$$

$$C_{coax} = \frac{2\pi\varepsilon_0 h}{\ln\left(\frac{b}{a}\right)}, \tag{2.3f}$$

where ε_0 refers to the permittivity of free space, μ_0 is the permeability of free space, and the rest of the variables are the same as previously defined.

Fujisawa's model starts from a basis of using Green's functions to analyze the fields inside the cavity. This analysis method gives the inductance of the resonator as

$$L = \frac{\mu_0 (h + g)}{2\pi} \ln\left(\frac{b}{a}\right). \tag{2.4}$$

It is notable that this is the same inductance relation one would get if calculating the inductance of a coaxial line traditionally as in [5]. This is also the same inductance relation as seen in (2.3b), with a minor variation where the length of the coaxial line is assumed to be the full height of the cavity, instead of only the height of the post. Again, due to the assumption that $g << h$, this has little effect on the overall prediction. The capacitance is modeled in two parts, with their sum equalling the total capacitance of the system. The first part is the parallel plate capacitance between the post and the top of the cavity, where

$$C_{post} = \frac{\varepsilon_0 \pi a^2}{g}. \tag{2.5}$$

This post capacitance is again the same post capacitance seen in the LEM and (2.3d).

Therefore, the key difference in the GF approach lies in the second capacitance, which represents the capacitance modeling of the cavity. The second capacitance is novelly derived by Fujisawa as

$$C_{cavity} = 4\varepsilon_0 a \ln\left(\frac{e\sqrt{(b-a)^2+(h+g)^2}}{2g}\right), \tag{2.6}$$

where e is the mathematical constant (e = 2.71828...), and the rest of the variables are the same as previously defined. Bringing it all together, the predicted frequency based on the dimensions of the cavity becomes

$$f_0 = \frac{1}{2\pi\sqrt{L\left(C_{post}+C_{cavity}\right)}}, \tag{2.7a}$$

or, expanded out

$$f_0 = \frac{c_0}{2\pi\sqrt{a\left(h+g\right)\ln\left(\frac{b}{a}\right)\left[\frac{a}{2g}-\frac{2}{\pi}\ln\left(\frac{2g}{e\sqrt{(b-a)^2+(h+g)^2}}\right)\right]}}. \tag{2.7b}$$

In these models, the size of g plays a dominant role. The way in which it is used to control tuning is readily apparent, but the way in which its rate of change affects the rate of change of the resonant frequency is less obvious. To a very rough approximation, in all of the models, a quadrupling of g is fundamentally limited to a halving of the resonant frequency. Considering that g is a physical size, this corresponds to smaller gap sizes rapidly causing shifts as they are easier to quadruple, with larger gap sizes being more difficult to shift. This also plays a major part in the trade-off between power handling and tuning range. For example, the gap size needs to be *at least* quadrupled to get an octave of tuning, and limitations of tuning ranges are often measured absolutely, not relatively. Therefore, the minimum distance must be chosen to allow for this quadrupling to happen, but the smaller

the minimum distance, the less power handling available due to the decrease in voltage needed to induce dielectric breakdown. In practice, a change of gap size of about 5:1 is often needed to get an octave of tuning, so this power restriction is limited even further.

2.1.1 Resonant Frequency Model Comparison

In an effort to fully generalize the resonant frequency equations, further research was pursued to see how robust these equations were at predicting the resonant frequency at various post radii, cavity heights, and gap sizes. To test this range, the cavity radius was kept constant at 7 mm. Then each combination of three different post radii (0.5 mm, 1 mm, and 4 mm) and three different cavity heights (30 mils, 60 mils, and 125 mils) was generated. On each iteration, a sweep of the post gap from 5 to 50 μm was performed and the predicted resonant frequency for each method logged. The cavity heights were chosen to align with commercially-available substrate thicknesses. The post radii were chosen to cover a range where the models aligned and then started to diverge based on the data presented in [7]. The sweep range of the gap was chosen based on previous experience with likely ranges/-magnitudes in tunable evanescent-mode cavity designs. The cavity radius was chosen to be a round number analogue to the value presented in [12]. To test the accuracy of the results, Eigenmode simulations in ANSYS HFSS, a finite element method (FEM) time-harmonic electromagnetic (EM) solver, were performed and treated as truth.

The full comparison of the various closed-form predictive methods to FEM simulation is seen in Figure 2.2. In general, all models do best when the post radius and cavity height are larger fractions of the cavity radius. The models also improve when the gap is a smaller fraction of the cavity height. This makes sense as the parallel plate capacitance starts to dominate and the $g << h$ assumption becomes more accurate. With a post radius that is a significant fraction of the cavity radius (a = 4 mm), all models roughly match the FEM

simulation at all tested gap sizes and cavity heights, supporting the claim that any one would work well enough for design purposes. However, as the ratio of post radius to cavity radius decreases, and to a lesser extent as ratio of cavity height to cavity radius decreases, the models rapidly diverge in their predicted frequency. The only model that maintains any semblance of accuracy at smaller post-to-cavity radius ratios is the GF method. In the cases tested, the LEM has percent error as high as 56% and the LCL method as high as 60%, while the GF method peaked at 20% error. Qualitatively, the GF method takes much more time to diverge from FEM results and stays on track through a variety of post radii, cavity heights, and gap sizes. Considering the relative complexity of the derivation of each method, the GF method should be a more accurate model, and this is reflected in the data.

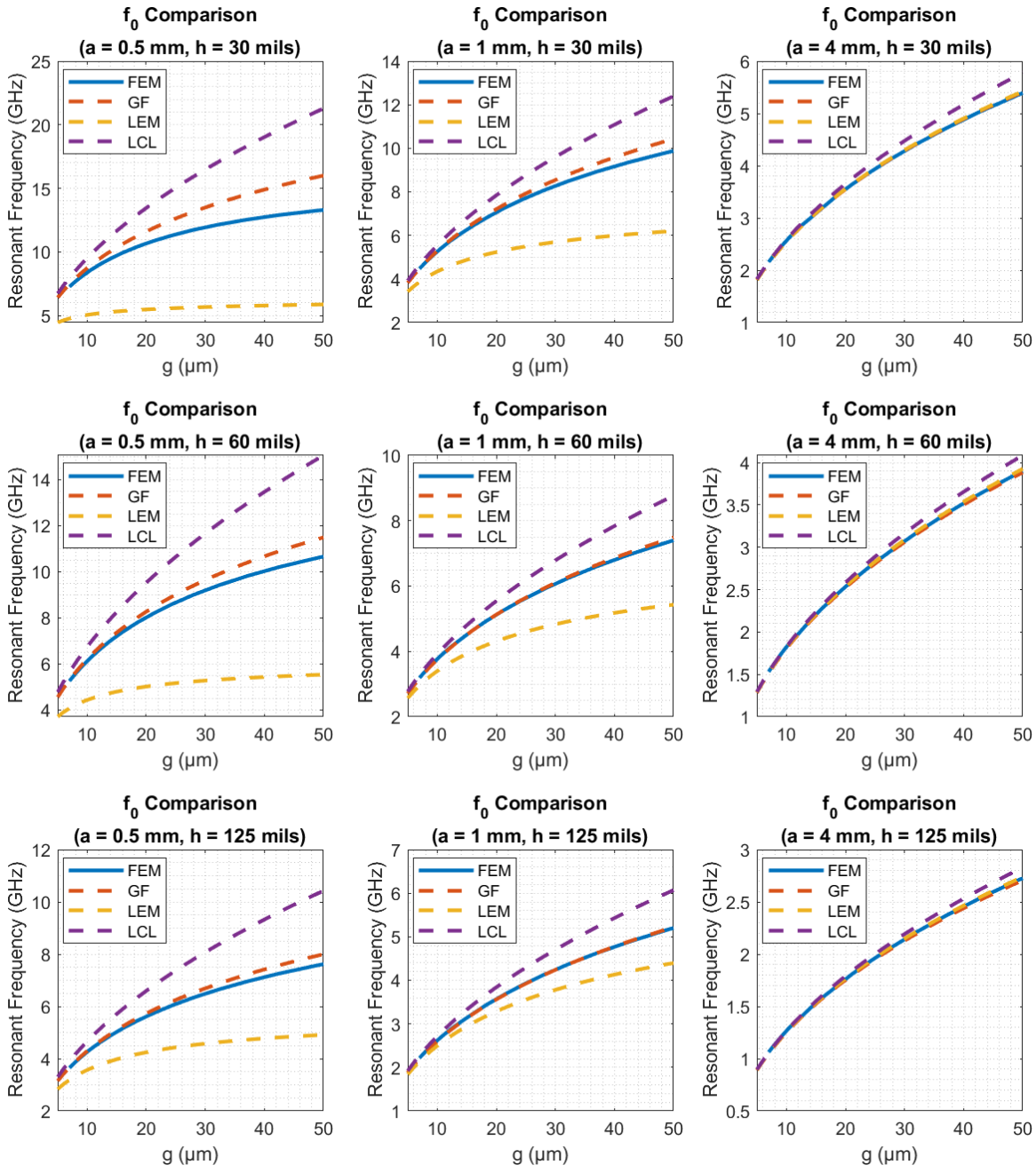

Figure 2.2: Comparison of evanescent-mode cavity resonant frequency predictions from closed-form expressions (Green's function (GF) method, lumped element method (LEM), and loaded coaxial line (LCL) method) to finite element method (FEM) analysis using HFSS. The figure demonstrates that the GF method is the most accurate method tested over a range of geometries.

2.1.2 Resonant Frequency Modeling with Dielectric Stack

Due to the superior accuracy of the GF method for predicting the resonant frequency of the cavity in a wide variety of geometry cases, it was chosen to predict the cavity resonant frequency in this project. However, it is notable that the relation does not take into account any sort of dielectric that the cavity is made up of. The model assumes that the cavity is vacuum filled and has perfect metal walls. For the purposes of this project and for the generalizability of the model to SIW based cavities, Fujisawa's equations were extended to include dielectric materials inside of the cavity. It is important to note that the loss in the conductor walls and the loss that will be introduced by the dielectric should not affect the resonant frequency of the cavities; it should only affect the quality factor. Since these equations are solely being used to determine the resonant frequency, the loss of each component is ignored.

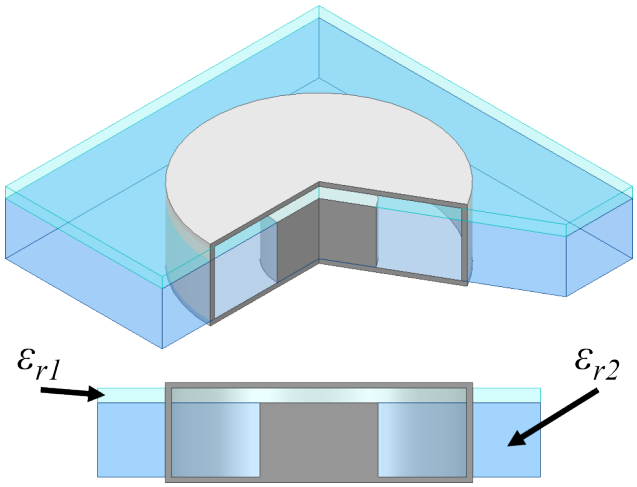

Figure 2.3: Cutaway simplified model of evanescent-mode cavity resonator built using a dielectric stack. The walls are a good conductor and it is assumed to be filled with two layers of differing dielectric. One dielectric (ε_{r1}) fills the gap between the post and the top of the cavity, while the other dielectric (ε_{r2}) surrounds the post.

Adjusting for the dielectric stack is a simple procedure given a few key assumptions. The first assumption is that the parallel plate capacitance is entirely unaffected by loading from the second dielectric. In an idealized parallel plate capacitor, there are no fringing fields that can interact with material exterior to the parallel plates. This allows (2.5) to be reorganized to

$$C_{post} = \frac{\varepsilon_0 \varepsilon_{r1} \pi a^2}{g}, \tag{2.8}$$

where ε_{r1} is the relative permittivity of the top dielectric. The second assumption is to continue with $g << h$. This allows the dielectric stack up inside of the cavity to be ignored, as the second dielectric will dominate in loading the cavity capacitance and the first dielectric will have minimal effect. Therefore, (2.6) becomes

$$C_{cavity} = 4\varepsilon_0 \varepsilon_{r2} a \ln\left(\frac{e\sqrt{(b-a)^2 + (h+g)^2}}{2g}\right), \tag{2.9}$$

where ε_{r2} is the relative permittivity of the bottom dielectric. The last assumption is that the dielectrics have a permeability about the same as free space. This is most often the case, but if one wanted to adjust for it, then all that would be needed is to add the relative permeability of the bottom dielectric (μ_{r2}) to the inductance equation. However, since the vast majority of dielectrics have a relative permeability very close to one, this part is left off for the rest of the analysis.

Bringing the adjusted equations together and simplifying and adjusting a few things, the new relation for the resonant frequency of a cavity with a dielectric stack becomes

$$f_0 = \frac{c_0}{2\pi\sqrt{a\,(h+g)\ln\left(\frac{b}{a}\right)\left[\frac{a\varepsilon_{r1}}{2g} + \frac{2\varepsilon_{r2}}{\pi}\ln\left(\frac{e\sqrt{(b-a)^2+(h+g)^2}}{2g}\right)\right]}}. \tag{2.10}$$

For brevity and to differentiate between the two Green's function methods, the Green's function based method that is based on (2.7b) and assumes a vacuum filled cavity will be referred to as the Green's Function Vacuum (GFV) model. The Green's function based method that is based on (2.10) and assumes a dielectric stack inside the cavity will be referred to as the Green's Function Dielectric (GFD) model.

An alternative expression that limits the inductance calculation to the height of the post and not the total height of the cavity was also tested, but this was found to be generally less accurate. In some cases it performed slightly better, but not enough to be the equation of choice. With this new expression that includes dielectrics, it is important to test the accuracy. Again, HFSS Eigenmode simulations were treated as truth with the same variances in post radius, cavity height, and gap size as before. However, various dielectrics were introduced in a dielectric stack. The top dielectric was left at a relative permittivity of one (ε_{r1} = 1), as most tunable cavities have an air cavity as the top dielectric. Note that all testing was done with ε_{r1} = 1, so the veracity of the model with top dielectrics other than air is unknown. However, the relative permittivity of the bottom dielectric was swept through a variety of values that span the range of many commercially available dielectrics. The ε_{r2} values chosen were 1, 1.5, 3.27, and 10. A ε_{r2} value of 1 was chosen as a control, 1.5 as a gradual step, 3.27 as the value of Rogers TMM® 3 (the material used in this project), and 10 as a large dielectric constant close to materials such as Rogers TMM® 10 (ε_r = 9.8), sapphire (ε_r = 10), and Rogers RT/duroid® 6010.2LM (ε_r = 10.2).

The GFD model was run through the same dimension permutations as before (a = 0.5 mm, 1 mm, 4 mm; h = 30 mils, 60 mils, 125 mils; g = 5 to 50 μm) as well as the same relative permittivity values (ε_{r1} = 1; ε_{r2} = 1, 1.5, 3.27, and 10). The predicted frequencies were recorded and compared to the GFV model and FEM analysis. The results for ε_{r2} = 1.5 are seen in Figure 2.4, ε_{r2} = 3.27 in Figure 2.5, and ε_{r2} = 10 in Figure 2.6. The results for ε_{r2} = 1.0 were exactly the same as before (as expected) and thus are omitted.

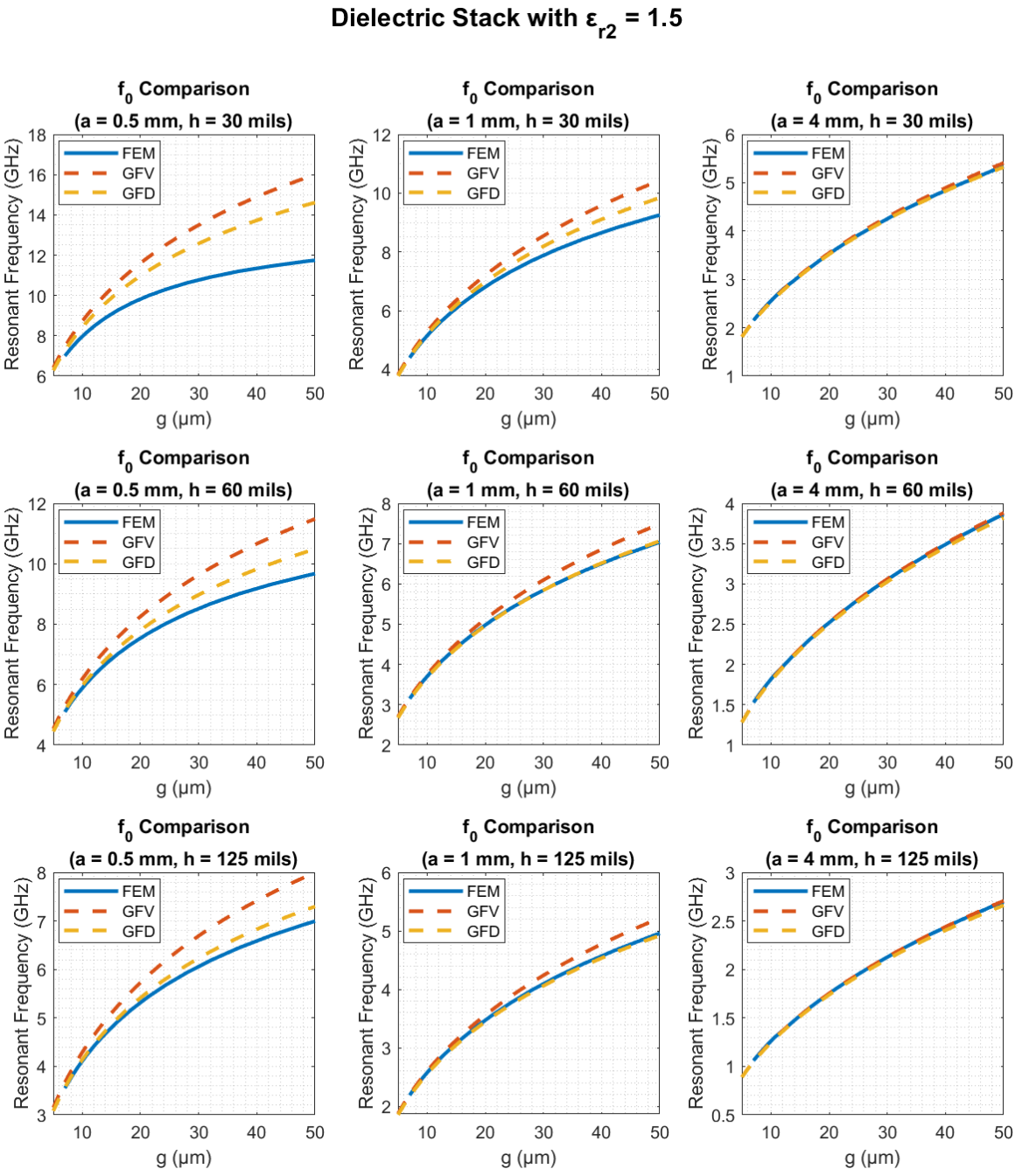

Figure 2.4: Comparison of closed-form models (GF vacuum (GFV) and GF dielectric (GFD) models) to FEM analysis for evanescent-mode cavities with dielectric stacks (ε_{r1} = 1, ε_{r2} = 1.5). GFV, based on (2.7b), is a control and assumes a vacuum filled cavity ($\varepsilon_{r1} = \varepsilon_{r2}$ = 1). GFD, based on (2.10), compensates for dielectric loading. The FEM model includes a dielectric stacks and is treated as truth.

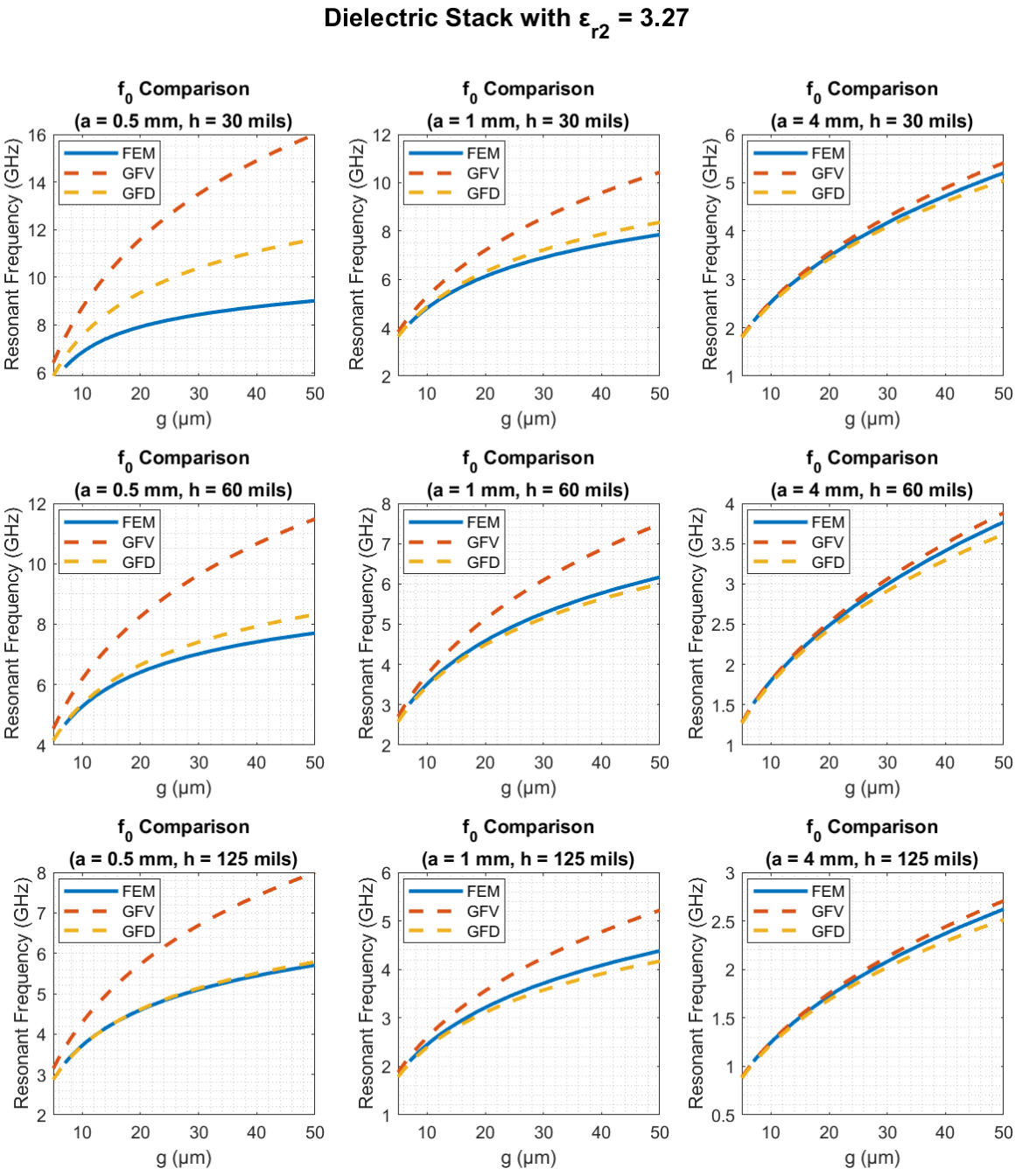

Figure 2.5: Comparison of closed-form models (GF vacuum (GFV) and GF dielectric (GFD) models) to FEM analysis for evanescent-mode cavities with dielectric stacks ($\varepsilon_{r1} = 1$, $\varepsilon_{r2} = 3.27$). GFV, based on (2.7b), is a control and assumes a vacuum filled cavity ($\varepsilon_{r1} = \varepsilon_{r2} = 1$). GFD, based on (2.10), compensates for dielectric loading. The FEM model includes a dielectric stacks and is treated as truth.

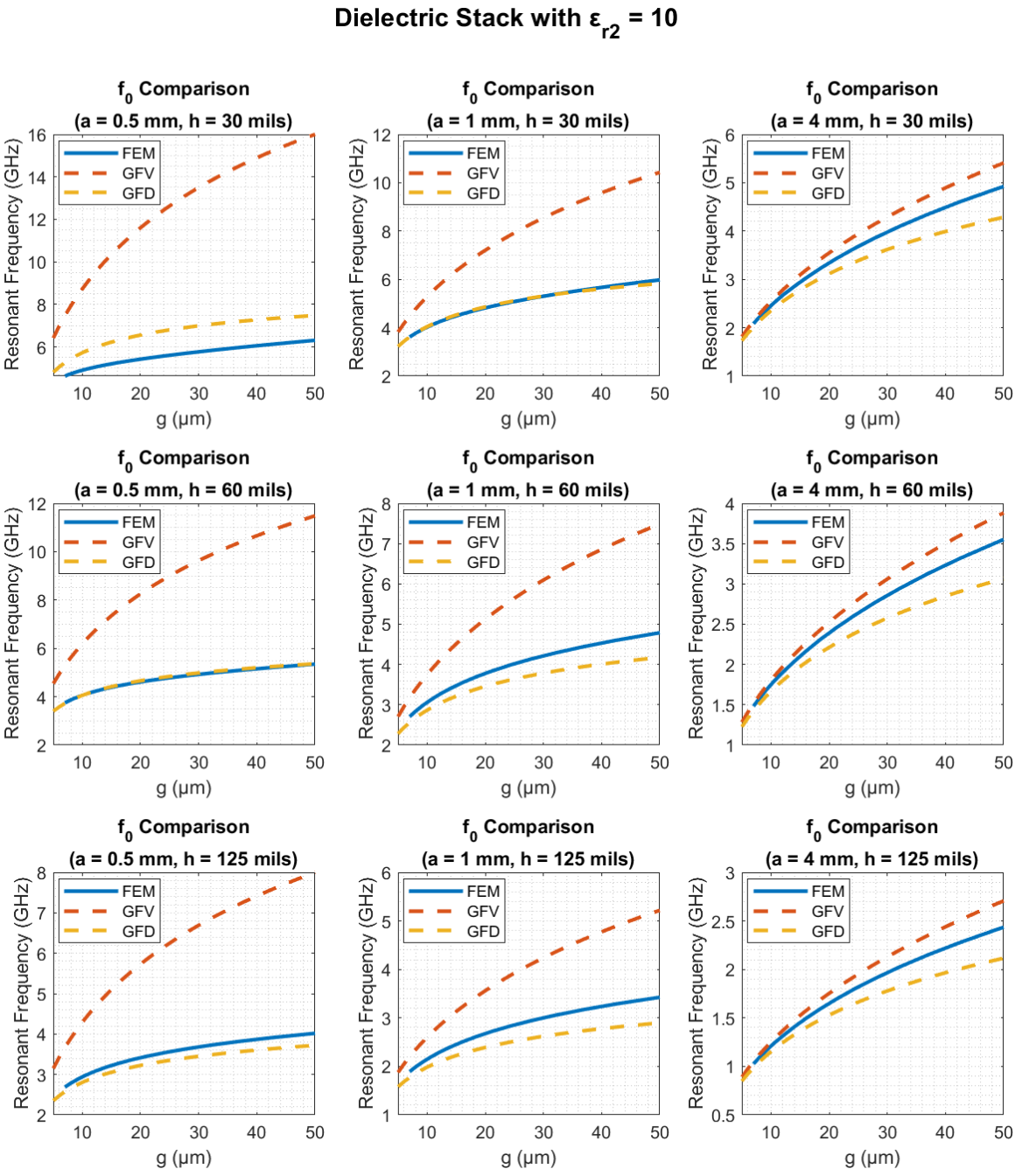

Figure 2.6: Comparison of closed-form models (GF vacuum (GFV) and GF dielectric (GFD) models) to FEM analysis for evanescent-mode cavities with dielectric stacks (ε_{r1} = 1, ε_{r2} = 10). GFV, based on (2.7b), is a control and assumes a vacuum filled cavity ($\varepsilon_{r1} = \varepsilon_{r2}$ = 1). GFD, based on (2.10), compensates for dielectric loading. The FEM model includes a dielectric stacks and is treated as truth.

A few general trends are seen in these plots. First, the GFD model actively compensates for the loading of the dielectric and drastically improves the accuracy of the predictions as the post radius decreases, height of the cavity increases, and the relative permittivity increases. However, as the post radius increases to become a significant portion of the total radius of the cavity, the GFD model starts to overcompensate for loading and will predict a much lower frequency than the FEM model. In some cases, especially as the dielectric constant gets larger, the GFD model has equal to or even greater error than the GFV model. Since at larger post radii and smaller dielectric constants the GFD and GFV models are very close in prediction, a switch point between the two methods should be used. An approximate relation based on these results is

$$f_0 = \begin{cases} \dfrac{c_0}{2\pi\sqrt{a\,(h+g)\ln\left(\frac{b}{a}\right)\left[\frac{a\varepsilon_{r1}}{2g} + \frac{2\varepsilon_{r2}}{\pi}\ln\left(\frac{e\sqrt{(b-a)^2+(h+g)^2}}{2g}\right)\right]}} & \text{for } \dfrac{a}{b} < 0.5 \\ \dfrac{c_0}{2\pi\sqrt{a\,(h+g)\ln\left(\frac{b}{a}\right)\left[\frac{a\varepsilon_{r1}}{2g} + \frac{2}{\pi}\ln\left(\frac{e\sqrt{(b-a)^2+(h+g)^2}}{2g}\right)\right]}} & \text{for } \dfrac{a}{b} > 0.5 \end{cases} . \quad (2.11)$$

It is often preferable to reverse parts of (2.11), particularly when extracting a gap size from a desired resonant frequency. Despite extensive effort, no closed-form method was found to put g as a function of f_0. This can be circumvented by curve fitting a generated curve from (2.11). A second order exponential tends to fit the plots extraordinarily well (often times with R^2 values of 1.0000). This equation takes the form

$$g = x_1 e^{y_1 f_0} + x_2 e^{y_2 f_0}, \quad (2.12)$$

where x_1, y_1, x_2, and y_2 can be found using MATLAB's curve fitting app, `cftool`. Another benefit of having this curve fitting function in place is that it is essential in generating

fits for the frequency versus gap curves of the Eigenmode simulations, allowing for quick tuning of the simulated resonators.

2.2 Finite Element Method (FEM) Modeling

While closed-form models are particularly expedient and valuable tools for cavity design, they are fundamentally limited by the assumptions they make. These assumptions are necessary to reduce the system to a solvable point, but they introduce error into the system. A method that relies on far fewer assumptions and can achieve much more accurate results is simulation software, in particular software that makes use of FEM analysis. One of the most popular pieces of FEM software for EM simulation is ANSYS HFSS. Within HFSS there are further subdivisions of modeling methods, with the two used in this thesis being Eigenmode and Driven Modal. Eigenmode simulations offer rapid and less computationally intensive solutions, but with limits in accuracy and a lack of ports. A lack of ports makes it difficult to accurately include the impact of excitation or feeding geometry. Driven Modal increases the solution time and computational demands, but offers better potential for accuracy by including feeding networks, includes support for ports, and adds other features, such as accurate radiation modeling, not present in Eigenmode.

Unfortunately, using HFSS is not as straightforward as plugging in parameters to a closed-form model. HFSS is a tool that requires practice to wield effectively, and therefore there are some key considerations to make when building models. As of HFSS 2018, by far the most important to ensure accurate results for evanescent-mode cavities is to add mesh operations in the gap, as the default meshing algorithm does not mesh the gap between the post and the top of the cavity finely enough to fully capture the capacitance of the post. These mesh operations should be added in both Eigenmode and Driven Modal simulations. Anecdotally, a good rule of thumb that balances accuracy and simulation time

is to set the maximum element length in the mesh operation to a fifth of the post radius. Additionally, if the mesh operation is performed on a non-model object, that object must be an unedited (no subtractions, unions, translations, rotations, etc.) rectangular plane or rectangular prism. If not done on one of these objects, HFSS may not give an error or any indication of a problem, but it will ignore any mesh operation you place on invalid objects. This means that a square, non-model box is required over the round post for mesh operations, or HFSS will ignore the mesh operation and defaults back to the inaccurate default meshing algorithm. Alternatively, the mesh operation can typically be performed on any model object, but the effect of that object must be considered for the simulation.

The recommended course of action for designing evanescent-mode cavities is to figure out the dimensions needed to meet specification with the closed-form expressions. Then, build a simplified model in Eigenmode in HFSS (with a mesh operation) to verify the resonant frequency, Q, etc. and make adjustments. After fine tuning, move the model over to a Driven Modal simulation and add realism (vias, coupling ports, etc.) and continue tuning. This should result in a model that meets specification, gives the most realistic results for center frequency, Q, etc., and is ready to be exported for fabrication.

2.3 Realization of Evanescent-Mode Cavity

Despite the high potential accuracy of Driven Modal simulations in HFSS, to know if models or simulations match reality, they must be verified with measurements. To demonstrate the accuracy of the closed-form models, Eigenmode simulations, and Driven Modal simulations, two SIW evanescent-mode cavities were designed, simulated, fabricated, and measured. The author is incredibly thankful to Eivy Arroyo Diaz for taking on the bulk of responsibility for fabrication and measurement. The cavity was designed to tune from 2-4 GHz, maintain a high Q, and be manufacturable through printed circuit board (PCB)

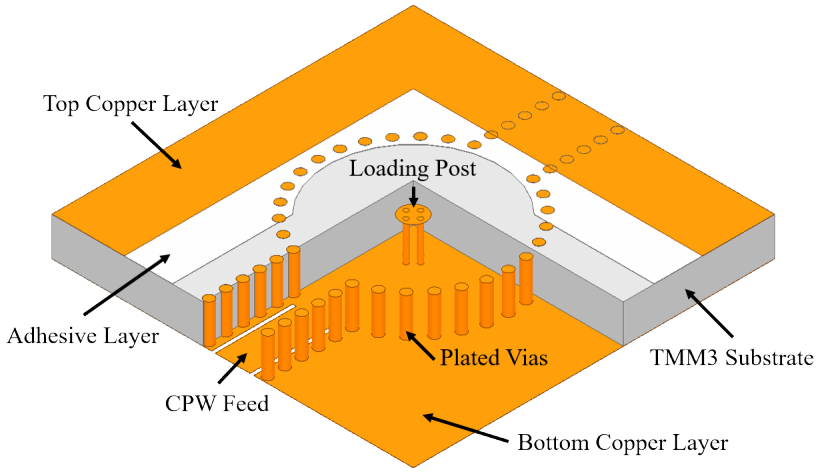

Figure 2.7: Structure of SIW evanescent-mode cavity with cutaway to depict layers

design techniques.

The cavity was designed to be $\lambda/10$ at the lowest frequency, 2 GHz. The diameter of the cavity was therefore 15 mm, so the radius, b, was 7.5 mm. The cavity diameter also needs to be bigger than the piezoelectric disc (piezo) that was used to tune the gap size, g, or tuning range will suffer due to the material constricting the movement of the piezo. The piezo chosen has a diameter of 12.7 mm (0.5 in), so it will fit within the cavity diameter. The lower substrate was Rogers TMM3® (ε_{r2} = 3.27) with a thickness, h, of 3.175 mm (125 mils). TMM3 was chosen for its stability, close to copper Coefficient of Thermal Expansion (CTE), and availability in substrate thicknesses and copper cladding thicknesses desired for this project. The upper dielectric was air (ε_{r1} = 1) to allow for easy tuning and higher Q due to a negligible loss tangent. The loss tangent of the top dielectric is a particularly important design consideration since 90% of the electric-field energy is typically stored in the gap above the post [32]. The piezo has a tuning range of $\pm$ 20 µm, so to accommodate a roughly typical 5:1 gap change ratio per octave, the minimum gap size must be around 10 µm. Plugging in these initial parameters to (2.11), the necessary post radius, a, to make the cavity resonate at 2 GHz is about 1.2 mm.

With these initial design parameters in mind, an Eigenmode simulation was performed with a simple model to verify the starting frequency and geometry of the cavity. After the Eigenmode results and minor tuning, the model was moved over to a driven modal simulation and made much more realistic. The resulting model is seen in Figure 2.7, with an exploded view showing the layers in Figure 2.8.

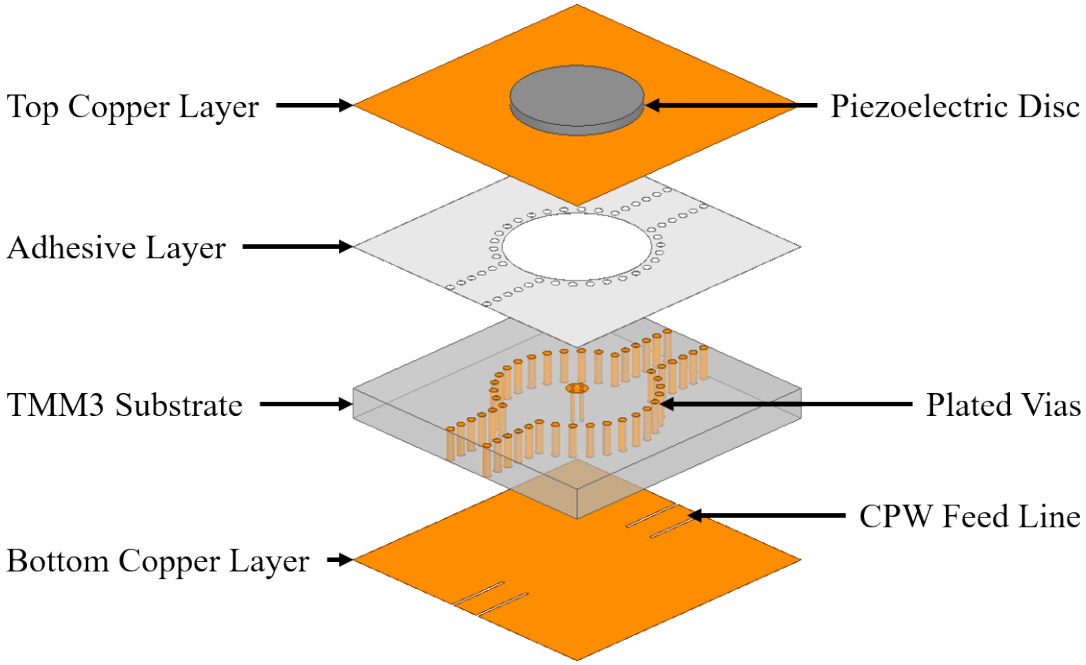

Figure 2.8: Exploded view of SIW evanescent-mode cavity showing many layer nature of the design

Vias were added to act as the cavity walls and enable the loading post. A rule of thumb of 60% conductivity of copper was applied to the plated vias to ensure accurate representation. Via diameter and center-to-center spacing is another key consideration when designing SIW components, as too much space between small vias can result in power leakage, while too little spacing with small vias increases manufacturing time and reduces the structural integrity of the board. In general, keeping the via center-to-center spacing (also known as pitch) greater than $\lambda_c/20$ but less than $\lambda_c/4$ is ideal, where λ_c is the wave-

length of the frequencies of interest in the material [33]. For this resonator and tuning range, the bounds are greater than λ_c/20 at the lowest frequency (2 GHz) and less than λ_c/4 at the highest frequency (4 GHz). Thus, the via spacing should fall between 2.07 mm and 2.07 cm. In addition, the larger the pitch-to-via-diameter ratio, the more the vias will act like an ideal metal wall, as long as the condition of the pitch being less than λ_c/4 is also met. The approximation converges to the ideal case as the via diameter and pitch go to zero and the number of vias goes to infinity. However, the smaller the via hole, the more difficult it is to drill and plate without error. Therefore, a balance between having as small as possible vias and ease of manufacture must be met. Based on previous experience, a 0.8 mm via diameter was chosen. Since TMM3 is such a stiff material, the limit of 2.07 mm was also relaxed and the minimum via spacing in the cavity walls is 1.4 mm, thus ensuring closer agreement to sheet wall models. Smaller vias were used for the post vias to allow multiple to fit on the loading post without significantly impacting the area. The diameter of the post vias is 0.4 mm.

An adhesive layer was added to create the air cavity above the post. The adhesive used was DuPont Pyralux LF0200 with a thickness of 51 μm. Unfortunately, DuPont has only published the dielectric constant of Pyralux at two points. The material has a relative permittivity, ε_r, of 3.6 at 1 MHz and 3.0 at 10 GHz. Therefore, to simplify the design, the adhesive layer was assumed to have the same dielectric constant as TMM3 (ε_r = 3.27), which is in between the dielectric constants seen at 1 MHz and 10 GHz.

A 50 Ω co-planar waveguide (CPW) was added on each side of the cavity to feed it. The CPW line coupled into the cavity due to magnetic coupling at the shorted ends of the line. Therefore, to have low coupling and accurate measurement of the unloaded Q of the resonator, the shorts were placed far back from the cavity. Low coupling is desirable due to the nature of how the Q's of the elements interact, whereby the measured Q is a function of the Q of the cavity and the Q of the coupling mechanism. The measured Q is commonly

referred to as the loaded Q (Q_L), the Q of the cavity as the unloaded Q (Q_u) and the Q of the coupling mechanism as the external Q (Q_{ext}). The relation between all of these Q's is

$$\frac{1}{Q_L} = \frac{1}{Q_u} + \frac{1}{Q_{ext}}. \tag{2.13}$$

Therefore, as the external coupling gets lower, and correspondingly Q_{ext} gets bigger, the measured Q becomes closer and closer to the actual Q of the cavity itself. In the first cavity designed and built, Prototype 1, the coupling was too strong to accurately measure Q_u, but it was able to demonstrate full tuning across S-band. To accurately measure Q_u, a rule of thumb is that the peaks of S_{21} should be below -20 dB. Therefore, in second cavity built, Prototype 2, the short was pushed farther away from the cavity to enable accurate measurement of Q_u.

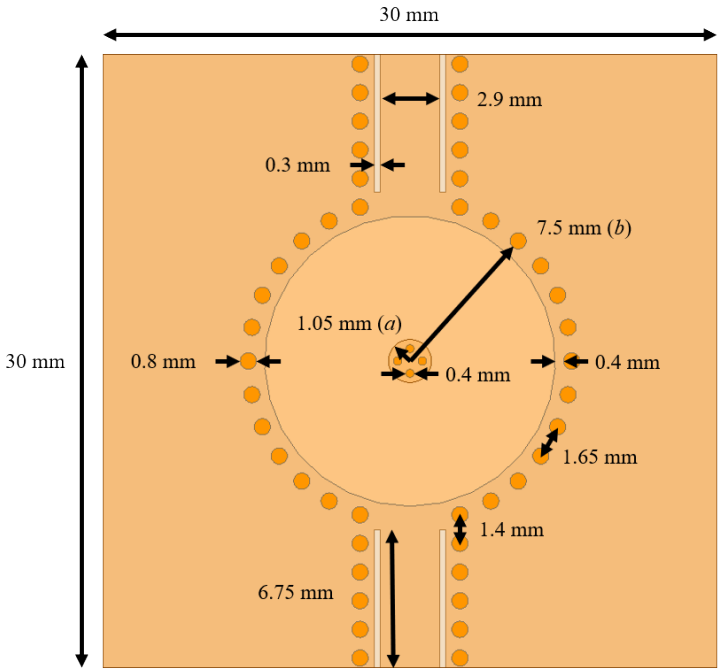

Figure 2.9: Top-down view of SIW evanescent-mode cavity with various dimensions labeled. CPW short location is reflective of the design of Prototype 2.

The addition of feed lines also functionally increases the size of the cavity, resulting in a small lowering of the resonant frequency. To adjust for this and other additional loading, the size post radius was reduced to 1.05 mm and the initial gap size was reduced to 8.4 µm. See Section 5.3 for more extensive discussion of the coupling of CPW lines into evanescent-mode cavities.

The most important design dimensions of the cavity are seen in Table 2.1, while a more detailed overview is seen in Figure 2.9.

Table 2.1: Summary of essential design dimensions for evanescent-mode cavity

Parameter	**Value**
Post radius (a)	1.05 mm
Cavity radius (b)	7.50 mm
Substrate height (h)	3.175 mm (125 mils)
Initial Gap Size (g_0)	8.40 µm
Gap Variation (Δg)	40 µm

The HFSS simulated response of Prototype 2 is seen in Figure 2.10, depicting full octave tuning. The magnitude of the response also indicates very low coupling, allowing for accurate extraction of Q_u.

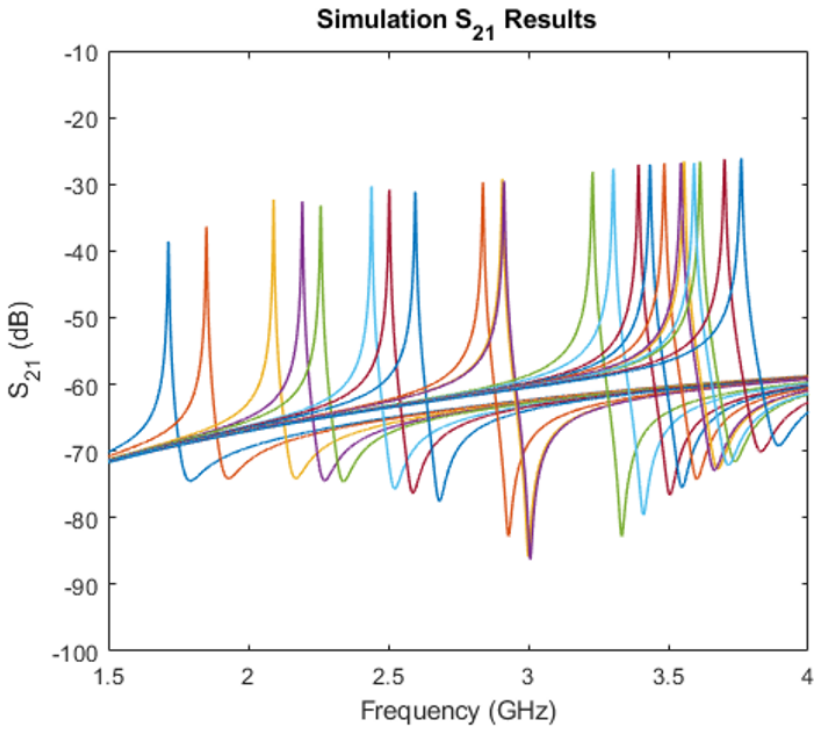

Figure 2.10: Transmission response (S_{21}) of Prototype 2

Two prototype resonators were built, and after soldering on coaxial connectors, attaching copper tape leads to bias the piezos, and calibrating the Agilent Technologies N5225A, the cavities were measured. The fabricated cavity of Prototype 2 is seen in Figure 2.11, depicting the piezo, attached bias lines, soldered connectors, and CPW feed lines. Measured results are seen in Figure 2.12.

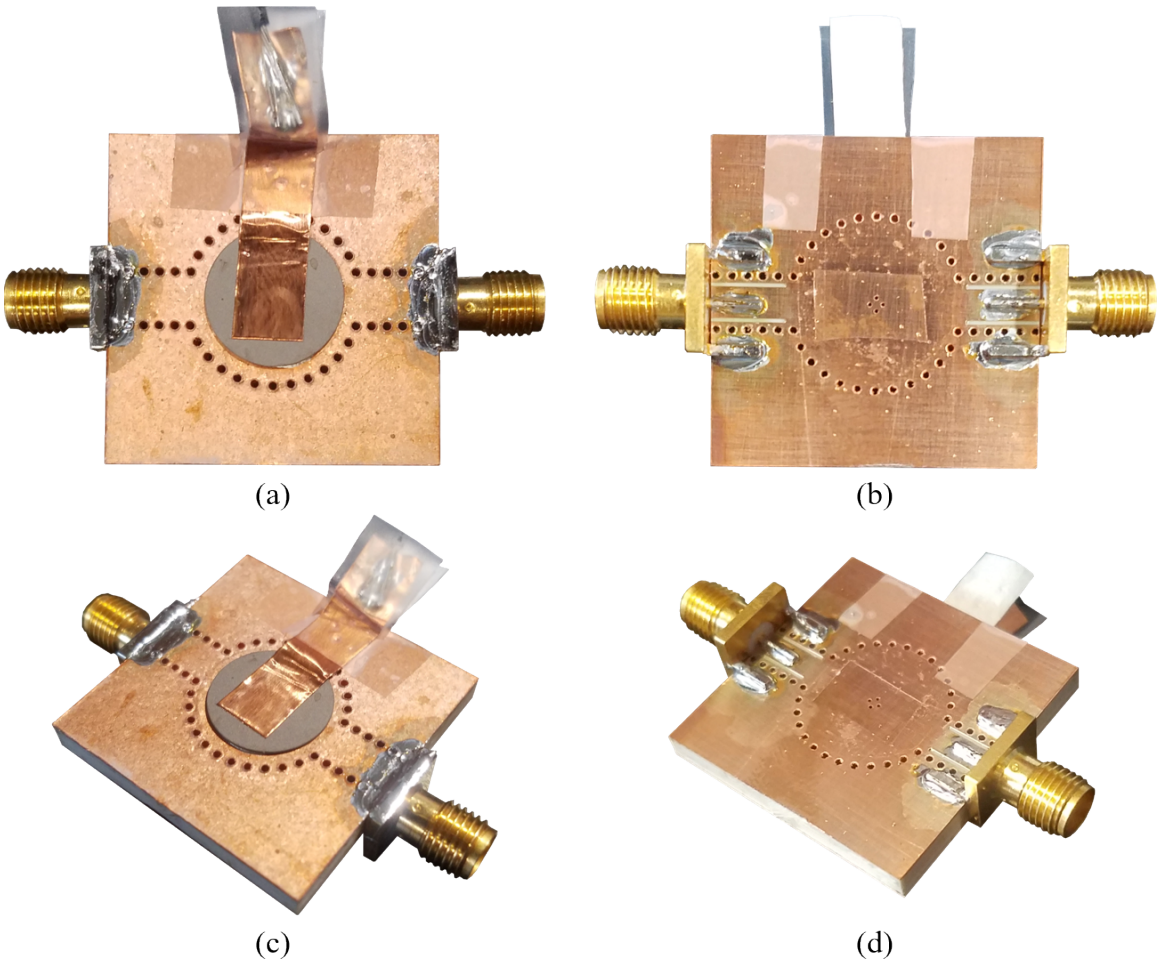

Figure 2.11: Fabricated Prototype 2. The top-down view (a) and top isometric view (b) show the piezo and attached bias lines, while the bottom-up view (c) and bottom isometric view (d) shows the CPW feed lines.

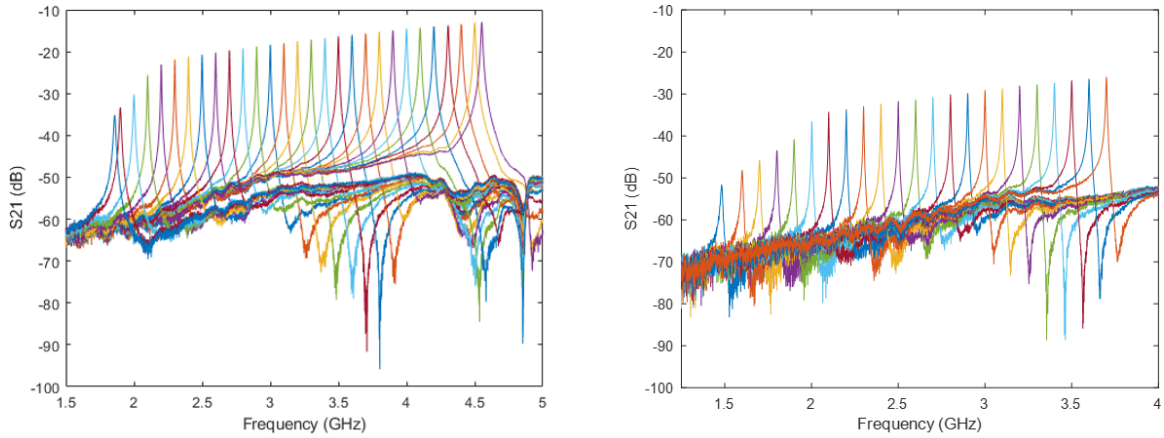

Figure 2.12: Measured S_{21} response of Prototype 1 (a) and Prototype 2 (b). Prototype 1 shows full 2-4 GHz tuning is possible, while Prototype 2 has external coupling weak enough to allow for accurate measurement of Q_u.

As seen in Figure 2.12a, the cavity is fully capable of tuning from 2-4 GHz with the piezo, proving that full octave tuning is possible with this technology. Figure 2.12b depicts significantly decreased input coupling, allowing for accurate extraction of Q_u. To extract the unloaded Q from the loaded Q, a few relations can be used. The first is

$$Q_u = \frac{Q_L}{1 - |S_{21}|}, \tag{2.14a}$$

where Q_L is found as

$$Q_L = \frac{f_0}{\Delta f_{3dB}}. \tag{2.14b}$$

In (2.14b), Δf_{3dB} represents the 3 dB bandwidth of the resonator. It is seen that in (2.14a), as the coupling decreases further, and therefore the magnitude of S_{21} decreases, Q_u converges to Q_L. With less than 30 dB of coupling, treating Q_u as Q_L introduces at most 0.1%

error, and therefore at extremely low couplings the relation becomes

$$Q_u = \frac{f_0}{\Delta f_{3dB}}. \tag{2.15}$$

A comparison of the calculated Q_u from simulation and measurements is seen in Figure 2.13.

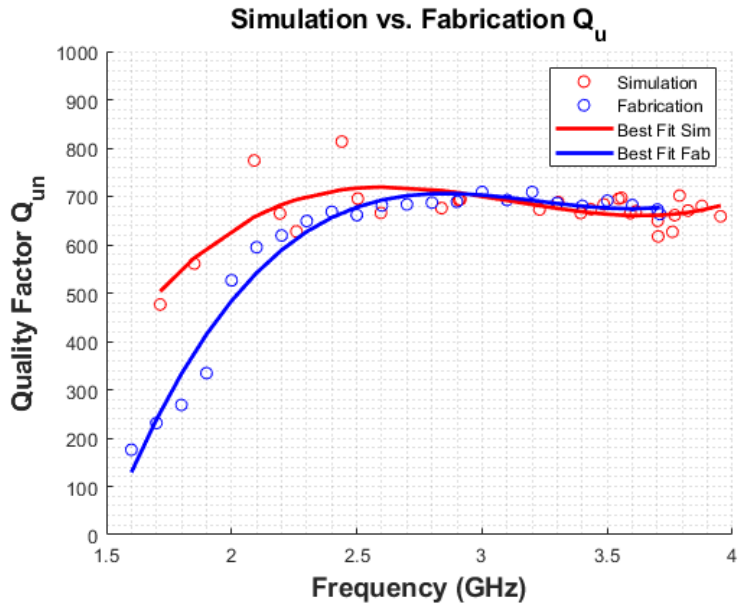

Figure 2.13: Calculated Q_u from simulated and measured response of Prototype 2. Due to the high rate of change of S_{21}, some roughness in calculated values can exist, so a line of best fit was applied to each data set.

Unloaded Q varies from roughly 500 to 800 across 2-4 GHz, a sufficiently high Q for the project. Agreement between measured and simulated results is also demonstrated, indicating that simulation will give valuable insights into the performance of the cavities. It is worth noting that as the frequency is extended below the desired range, the Q rapidly degrades, so it is important to design these resonators such that they are not too heavily loaded, as this causes a decrease in Q.

2.4 Power Handling Investigation

Due to the nature of evanescent mode cavities previously demonstrating high power handling capability, an investigation of the theoretical power handling of this cavity was completed. In evanescent-mode cavities with micrometer range gap sizes, the predominate limit on power is discharge through the dielectric in the gap. In these particular cavities, the dielectric in the gap is air, so gas discharge is the main limiting factor. Three different physical phenomena contribute to gas discharge: electron impact ionization, secondary electron emission, and field emission. In copper-walled devices at atmospheric pressure, at gap sizes less than 0.5 μm, field emission is the predominate contributor to discharge, but in gap sizes greater than 5 μm, field emission contributes less than 5% to the total discharge [34]. In gap sizes greater than 10 μm, the contribution of field emission becomes negligible [35]. If gas discharge occurs, plasma etching and metal deposition inside of the cavity may take place. These effects have permanent impacts on performance of the cavity, often leading to an increase in loss and a decrease in resonant frequency. For copper-walled devices at atmospheric pressure, gas discharge occurs at specific electric field strength in the gap. This value is reported as 7.9 V/μm [36]. From this value, a limit on power handling can be estimated from the simulated field strength inside of the cavity [7].

To begin, an ideal model is created with admittance inverters to represent coupling. For this example, a coupled resonator with a 2% fractional bandwidth was conceived. The resonator was tuned across S-band (specifically to 2, 3, and 4 GHz) to extract the predicted power handling of the cavity across the band. A coupled resonator was selected to test the power handling with a specific bandwidth. A 2% fractional bandwidth was selected to match later designs of the filtenna, which has a 2% FBW. Since the capacitance of the system increases to lower the frequency, the area of the capacitor does not change, and the gap size decreases, the strength of the electric field will likely increase as the resonant

frequency decreases. This increase in field strength will likely correspond to a lower ability to handle power since the breakdown field strength will be reached at lower input power.

Following the method of [7], the model was scaled so that it had an input power of 1 W. A constant capacitance value of 1 pF was chosen and everything else scaled accordingly. Additionally, the quality factor of model was scaled to match the extracted quality factor from measurements (Q_u = 500 at 2 GHz, 700 at 3 and 4 GHz). The model was simulated in AWR's Microwave Office. The maximum stored energy was found to be 6.5759 nJ at 2 GHz, 4.6214 nJ at 3 GHz, and 3.4660 nJ at 4 GHz. The decrease in stored energy is due to the increase in absolute bandwidth of the resonator as it is tuned across the band as well as the increase in relative loss in the resonator at lower frequencies. The absolute bandwidth increases from 40 MHz at 2 GHz to 80 MHz at 4 GHz, despite the fractional bandwidth staying the same. The resistor value could be kept the same, but in this method the capacitor value is kept constant across frequency. If instead the capacitor was changed to keep the resistor the same, the energy stored would also decrease due to a decrease in voltage across the capacitor. Both effects result in an identical values in stored energy at each frequency and the downward trend will hold.

Following the extraction of stored energy in the model, an Eigenmode simulation was performed to extract the field strength in the gap. The simulation stored energy was set to 1 nJ. The resulting field distribution at 2 GHz can be seen in Figure 2.14. The fields were extracted from the center of the gap to limit simulation artifacts that result in unrealistic peaks in electric field at sharp conductor/dielectric boundaries. The electric field energy is highly concentrated above the center post of the cavity, and is correspondingly the location of highest field strength. Due to the planar nature and sharp edges of the top of the post, current crowding occurs on the outer edge of the post, leading to a stronger electric field presence. The maximum electric field in simulation was 3.4251 V/μm at 2 GHz, 1.8357 V/μm at 3 GHz, and 1.0636 V/μm at 4 GHz.

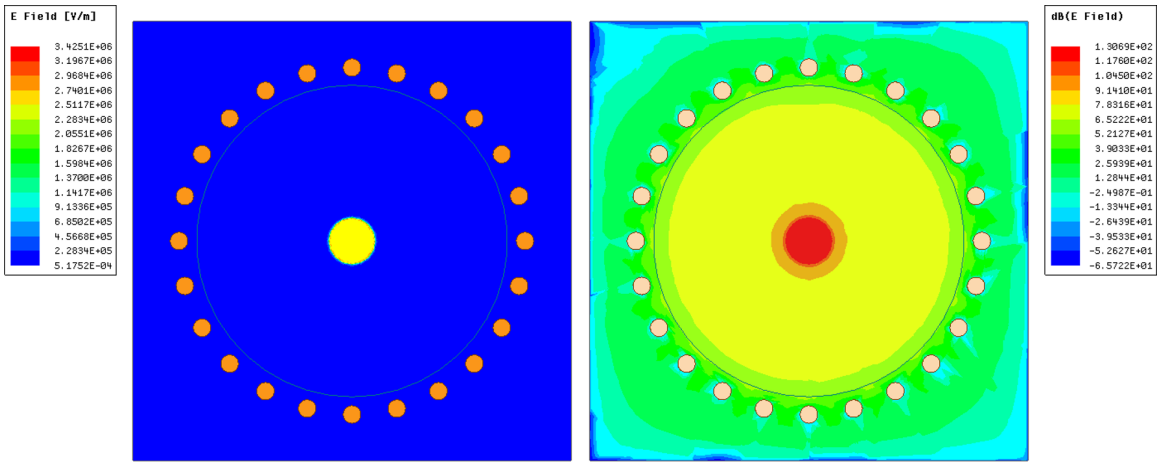

(a) (b)

Figure 2.14: Electric field strength and distribution in capacitive gap of an evanescent mode cavity tuned to 2 GHz. The electric fields are represented in V/m (a) and in dB of V/m (b), highlighting the large concentration of fields above the center post of the cavity.

The stored power of the Eigenmode simulation can be directly scaled to the maximum stored power before breakdown. The relation is

$$W_{max} = \left(\frac{E_{br}}{E_{eigen}}\right)^2 W_{eigen} \tag{2.16}$$

where W_{max} is the maximum stored power before breakdown occurs, E_{br} is the breakdown electric field strength (7.9 V/μm), E_{eigen} is the maximum observed electric field strength in the Eigenmode simulation, and W_{eigen} is the Eigenmode stored energy. Once the maximum stored energy is known, it can be directly scaled against the model to find the maximum power. The relation becomes

$$P_{max} = \left(\frac{P_{model}}{W_{model}}\right) W_{max} \tag{2.17}$$

where P_{max} is the predicted maximum power handling (or input power) of the evanescent mode cavity, P_{model} is the input power of the model (1 W), W_{model} is the maximum stored

energy of the model, and W_{max} is the maximum stored power before breakdown occurs. Combining (2.16) and (2.17) yields

$$P_{max} = \left(\frac{E_{br}}{E_{eigen}}\right)^2 \left(\frac{W_{eigen}}{W_{model}}\right) P_{model} \tag{2.18}$$

For the evanescent-mode cavity designed, the maximum power handling was predicted to be 0.8089 W (29.0790 dBm) at 2 GHz, 4.0075 W (36.0288 dBm) at 3 GHz, and 15.9171 W (42.0186 dBm) at 4 GHz. The power handling increases exponentially with frequency, leading to a rapid decrease in power handling in highly loaded cavities. This confirms the trade-off between power handling and tunability.

2.5 Conclusions

An overview of previous work with SIW evanescent-mode cavity resonators was presented. Modeling of these resonators, from closed-form expression all the way to complex FEM design was discussed with guidelines and improvements to previous work also included. An adjusted and improved closed-form expression based on Green's functions and including compensation for dielectric stacks was presented and limitations and design parameters discussed. Improvements in modeling within HFSS and a design workflow was presented, enabling future researchers to easily design these cavities. An example cavity was fabricated using this process and the measured results compared to simulation. Simulation and measurement showed good agreement, verifying both the closed-form modeling and the simulated results. Finally, a prediction for power handling of the cavity was presented, indicating that the cavity can handle over 29 dBm for the entire tuning range, up to a maximum of 42 dBm at 4 GHz.

Additionally, the lessons learned from this design process can be readily applied to the

proposed filtenna design and analysis techniques, increasing the speed and ease with which these filtennas can be made. The models also provide valuable insight into design parameter interactions and the strength of those interactions, making exploration of the design space easier to understand and optimize. With this in mind, insight into antenna performance and design was also needed, and so a tunable antenna was designed, simulated and fabricated.

Chapter 3

Loaded Slot Antenna Theory

In order to create a widely tunable, high-power filtenna, it is first necessary to demonstrate a widely tunable, high-power handling antenna is possible. As mentioned previously, little research has been done into antennas with this combination of traits. In order to demonstrate this is possible, a mechanically actuated, tunable slot antenna was conceived. It is mechanically actuated as that is the only technology that currently allows for a combination of high-power handling and high linearity, but if new technology arrives, the lessons learned still apply. Slot antennas offer a planar nature, low manufacturing complexity, desirable radiation patterns, and efficient operation. Slot antennas also offer a key benefit: they can be made as a single layer. Shunt components can be placed directly on the antenna without having to connect through a substrate, making the addition of tunability a simpler process [13].

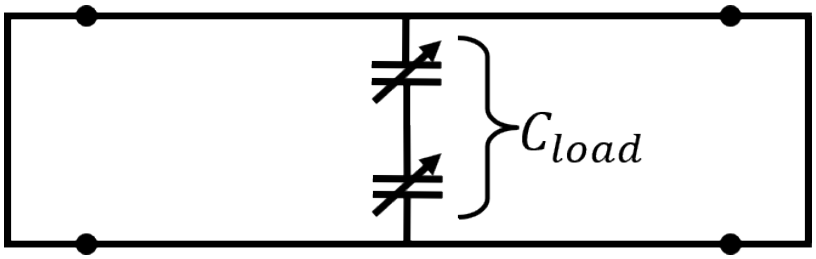

Figure 3.1: Equivalent transmission line model of slot antenna with capacitive load in the center

In this chapter, a tunable antenna is introduced that can tune a full octave across all of S-band (2-4 GHz) while maintaining high efficiency. A capacitive plate is positioned above a slot antenna, acting as two tunable capacitors in series, themselves shunt across the slot. A transmission line representation of this idea is depicted in Figure 3.1. Displacing the plate changes the capacitive load seen by the antenna, causing the antenna to appear electrically larger or smaller. A series of capacitor plate geometries were examined for simplicity and efficiency, and a circular capacitive plate was chosen for its high efficiency, sensitivity, and resistance to positional error. Two prototype designs were simulated, built, and measured to demonstrate the feasibility of such an antenna. The measured results are compared to simulation and the lessons learned from this project are taken to the full filtenna design.

3.1 Piezo-Actuator Slot Antenna Design

There are several factors to consider when designing a tunable capacitively loaded slot antenna. One of the main concerns with this antenna is the ability to handle high power. Similar to the evanescent-mode cavities, to maximize power handling, the minimum capacitive gap needs to be as large as possible to limit dielectric breakdown. However, as one increases the minimum capacitive gap, the area of the capacitive plate must increase to give an equivalent amount of loading. A large metal plate above a slot antenna causes undesirable interference in the radiation pattern. A large plate also forms a less sensitive capacitor as a larger portion of the plate is farther from the center, which is the location of strongest E-field [37].

The second main factor is tunability. A highly loaded slot antenna is much easier to tune than a lightly loaded one, as comparative changes in capacitance are much more easily achieved with small movement distances. However, more loading makes the antenna electrically smaller as compared to its operational frequency, which consequently results

in more loss and therefore lower radiation efficiency [38]. Therefore, a balance between amount of loading, efficiency, tuning range, and power handling must be met.

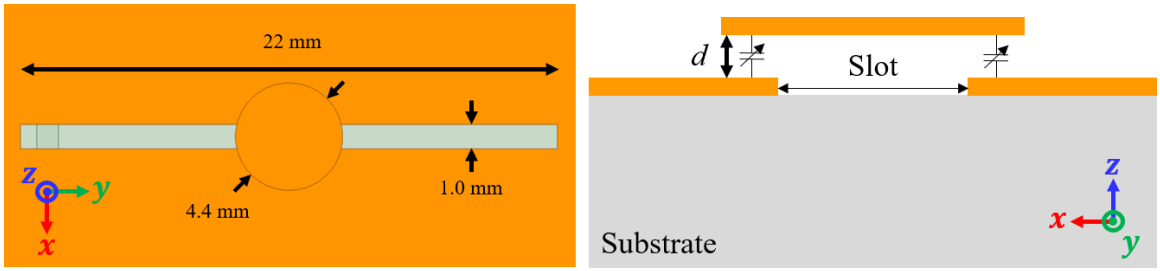

Figure 3.2: Model of tuning mechanism on 22x1 mm slot. The distance, d, is varied over the entire plate to adjust the capacitive loading of the slot. The antenna is fed with a lumped port.

As discussed previously, if the device (cavity resonator or antenna) is modeled as an RLC resonator, the ability to at least quadruple capacitive loading and therefore a quadruple parallel plate distance is necessary to achieve a full octave of tuning. This minimum assumes that the loading capacitor acts like a parallel plate capacitor and the resonator has minimal capacitance itself. In an evanescent-mode cavity, the cavity itself has some capacitance and the parallel plate model holds fairly well due to the small gap size, resulting in a close-to-ideal 5:1 typical tuning ratio needed for the capacitive gap. Unfortunately, with observed loaded slot antennas, the non-uniform field distribution along a slot causes a divergence in the tuning ratio needed, with a roughly 14:1 ratio in capacitance or plate distance needed for an octave. This effect was tested in HFSS with the geometry seen in Figure 3.2, where the capacitive plate is free-floating above the slot and the antenna is fed with a lumped port at the 50 Ω point. The capacitive gap was tuned from 15 µm to 212 µm (14:1 tuning ratio), resulting in a resonant frequency change from 2-4 GHz. The radiation efficiency remained above 70% for the whole range. Figure 3.3 demonstrates the tuning capability of this antenna design across all of S-band.

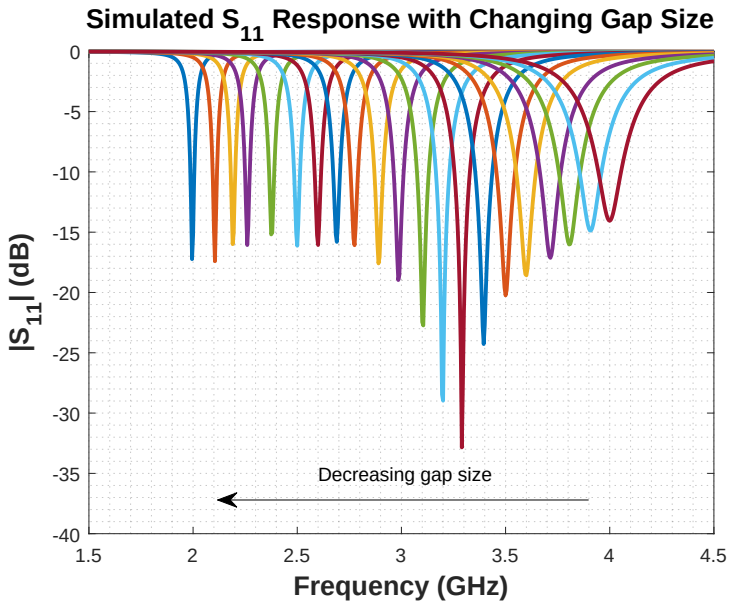

Figure 3.3: Reflection response (S_{11}) of capacitive plate loaded slot antenna. Demonstrates 2-4 GHz tuning while maintaining a greater than 15 dB return loss at each tuning point.

Due to this drastic increase in tuning ratio compared to the evanescent-mode cavities, a new method of actuation is necessary. The required minimum distance for a 14:1 tuning ratio is about 3 µm given 40 µm of actuation, far too small for any sort of high-power system. To overcome this limitation, new actuators were looked into, with the M3-L Micro Linear Actuator by New Scale Technologies (seen in Figure 3.4) selected as the final candidate. The M3-L can actuate a total distance of 6 mm, giving a minimum distance of 462 µm with a 14:1 tuning ratio, which is enough to handle a significant amount of power. This large tuning distance comes with an advertised step size resolution of 0.5 µm and an internal control loop to compensate for piezo drift.

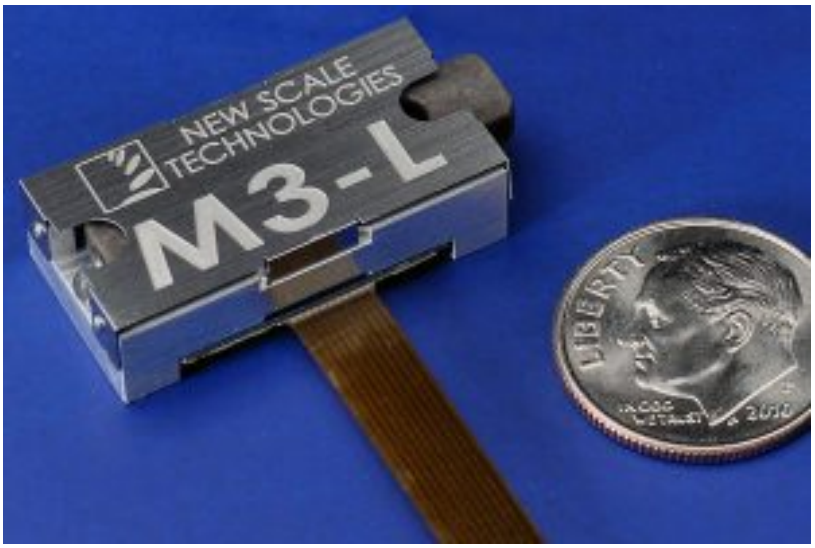

Figure 3.4: M3-L Micro Linear Actuator by New Scale Technologies in reference to a dime. From [39].

It is necessary to mount the actuator above the capacitive disc such that the linear actuation can move the plate up and down over the antenna. To this end, a mounting structure was designed. In addition, the main body of the piezo-actuator is a large metal box. There were concerns on what effect putting a large metal box above an antenna would have on its radiation pattern, loading, efficiency, etc. To see what effect all of these structures would have, a simulated model with a mounting structure for the piezo-actuator, a simplified piezo-actuator, and feeding structure was created in HFSS. A Dyson balun [40] was chosen to feed the slot due to its reliable and simple manufacture. It was necessary to put the feeding point close to the end of the slot to ensure a good impedance match. In addition, to ensure accurate results it is again encouraged to include a mesh operation in the gap between the capacitive plate and the slot antenna. The rule of thumb of setting the maximum element length to a fifth of the plate radius also applies here. The resulting model is seen in Figure 3.5, and was the first design fabricated and tested, thus Prototype 1.

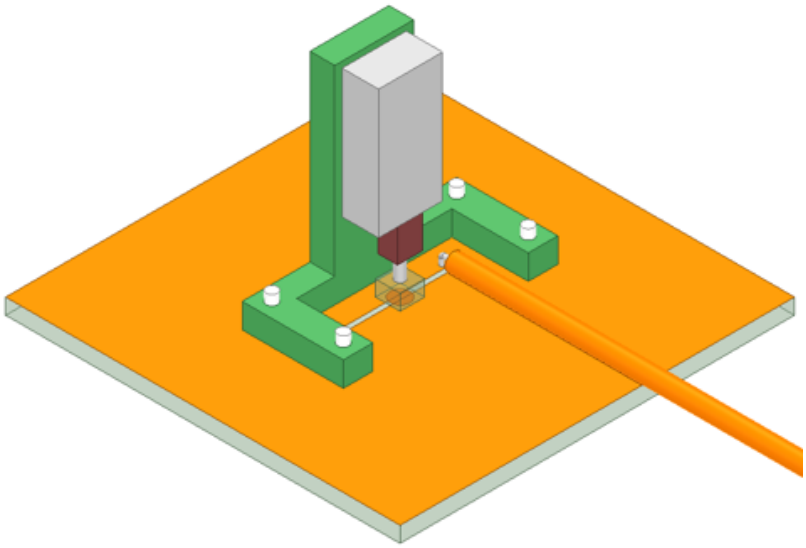

Figure 3.5: HFSS model of the slot antenna with tuning mechanism included, showing how the physical model was approximated in simulation. Grey is aluminum, green/brown is plastic ($\epsilon_r = 2.5, tan(\delta) = 0.1$), white is PVC Plastic (simulating the nylon screws), and orange is copper. The copper is on a 125-mil-thick TMM3 dielectric substrate. The coaxial cable is modeled according to the specifications of a RG402/U Coaxial Cable. This model represents Prototype 1.

However, this design was found to have tuning and manufacturing difficulties. The capacitive plate was difficult to align to be perfectly flat, as the attachment method would cause deflection. Super glue was used to attach the plate to the actuator, and the surface tension and contraction while drying would both lead to unpredictable alignment. The mount itself would flex back and forth, as described in Figure 3.6, causing drift in the frequency tuning of the antenna as the flexing caused the gap to change size. The antenna otherwise performed as expected, but the drift was difficult to account for in measurement, so a second mount type was developed.

The new mount type, a render of which is seen in Figure 3.7, includes several features

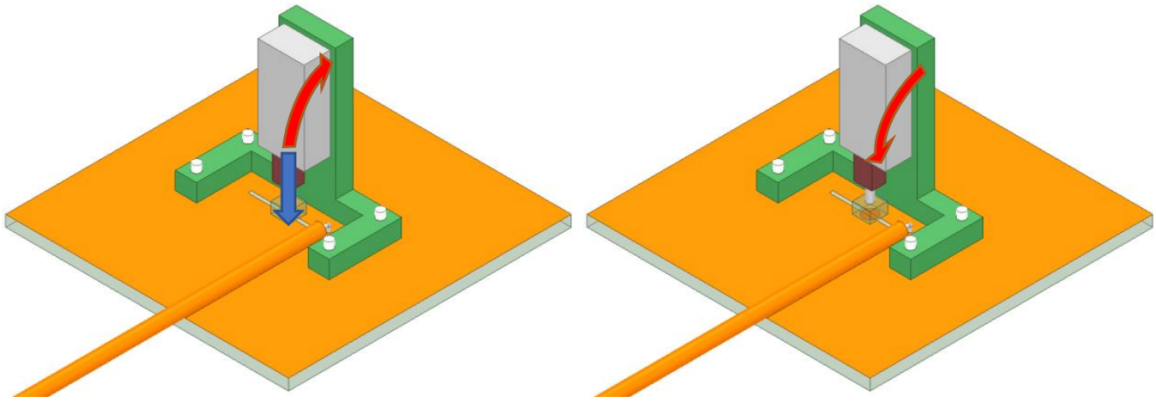

(a) (b)

Figure 3.6: In (a), pressure put on disc by actuator (blue arrow) can cause the mount to deflect backwards (red arrow). When pressure is relaxed (b), gravity and internal tension can cause the mount to deflect forwards, slowly decreasing the capacitive gap.

to fix the issues of the previous design. The mount is mostly symmetric, with anchors to the substrate on both sides to limit bending. Reinforcement beams are included to limit deflection further. Additionally, an alignment mechanism is included in the design. The 'X' like pattern on the bottom is removable, with the intention that the capacitive plate is attached to the bottom of the center of the 'X' and the actuator to the top. This allows for the epoxy for each to set while the plate is held in place, limiting manufacturing error. The legs of the 'X' can be removed with clippers once the epoxy has set.

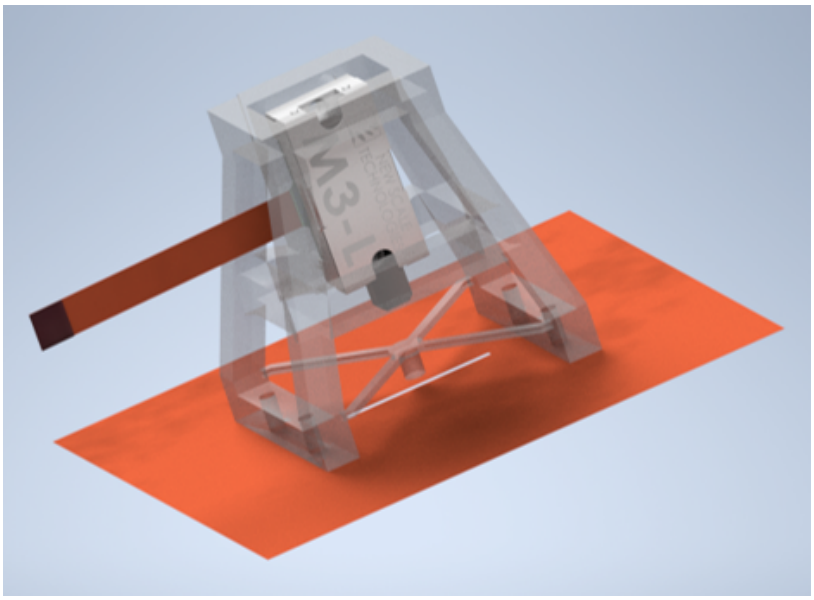

Figure 3.7: Rendering of mounting mechanism for Prototype 2. The alignment 'X' can be seen near the slot and below the actuator.

With this new mount designed, a simplified model was imported into HFSS to test its effect on the performance of the tunable antenna. To determine which parts affected the antenna the most, the addition of structures was done in two steps. First, only the simplified models of the structure and the mount were added, with the antenna still fed with a lumped port. Second, a Dyson balun was added to the structure along with the mount and actuator.

3.1.1 Mount and Actuator Effects

A simplified model of the structure and mount was created in HFSS, shown in Figure 3.8. However, modeling the mount presented an issue. The material eventually used for the mount is Grey Resin from Formlabs, which is a proprietary mixture and Formlabs does not have the dielectric constant published. However, based on data showing Grey Resin having a similar dielectric constant profile to ABS at terahertz frequencies [41], photoresins in general seeming to decrease in dielectric constant as frequency increases [42], and the

dielectric constant of ABS seemingly around 3 at our frequencies of interest [43], an educated guess was taken. Grey Resin was assumed to have a ε_r of 3, with a loss tangent of 0.02.

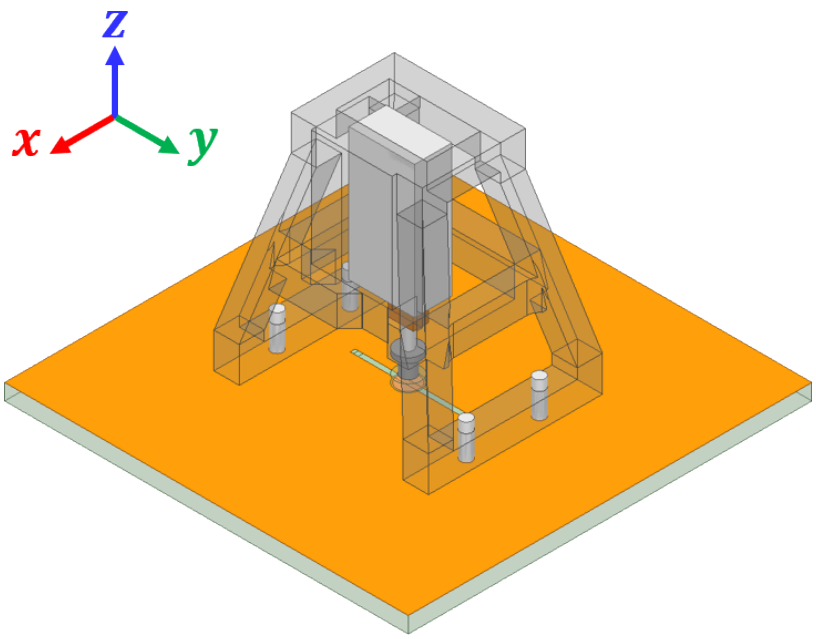

Figure 3.8: HFSS model of slot antenna with simplified mount and actuator.

Despite this fairly lossy structure introduced to the design, the addition of the mounting structure had surprisingly little effect on the performance of the antenna. The tuning range needed to be increased slightly due to the additional loading added by the mount, from 15 µm to 245 µm, bumping the tuning ratio to roughly 16:1. There was also a slight change in the match of the antenna, which is reflected in the S_{11} response, seen in Figure 3.9. The match improved at lower frequencies and degraded at higher frequencies, but still maintained a good match across all of S-band.

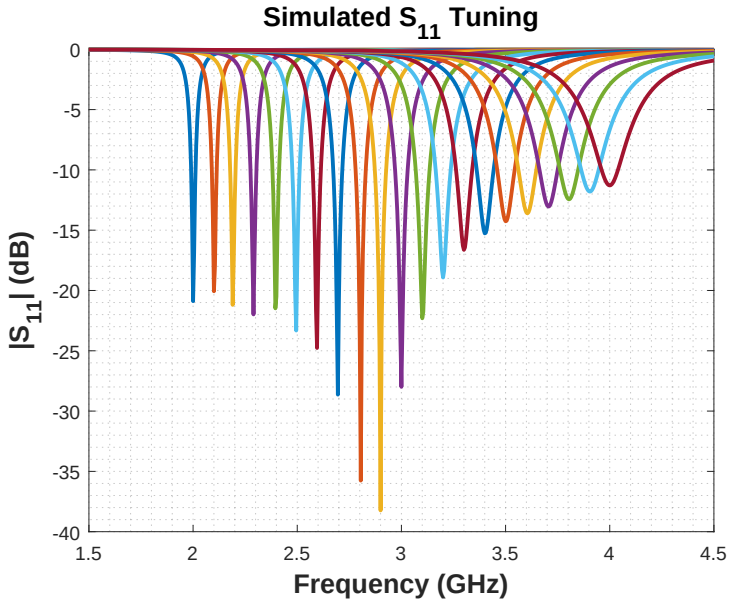

Figure 3.9: Simulated reflection response (S_{11}) of the loaded slot antenna with the Prototype 2 mount design.

The radiation pattern of the antenna was also slightly impacted, but not drastically, with the gain shifted in the direction of the mount. The broadside gain on the mount side of the slot saw a roughly 1 dB increase on average compared to the suspended plate simulation, while the gain opposite the mount side saw a roughly 0.25 dB decrease on average. The comparative gain plots can be seen in Figure 3.10 and more a more detailed numerical summary can be seen in Table 3.1.

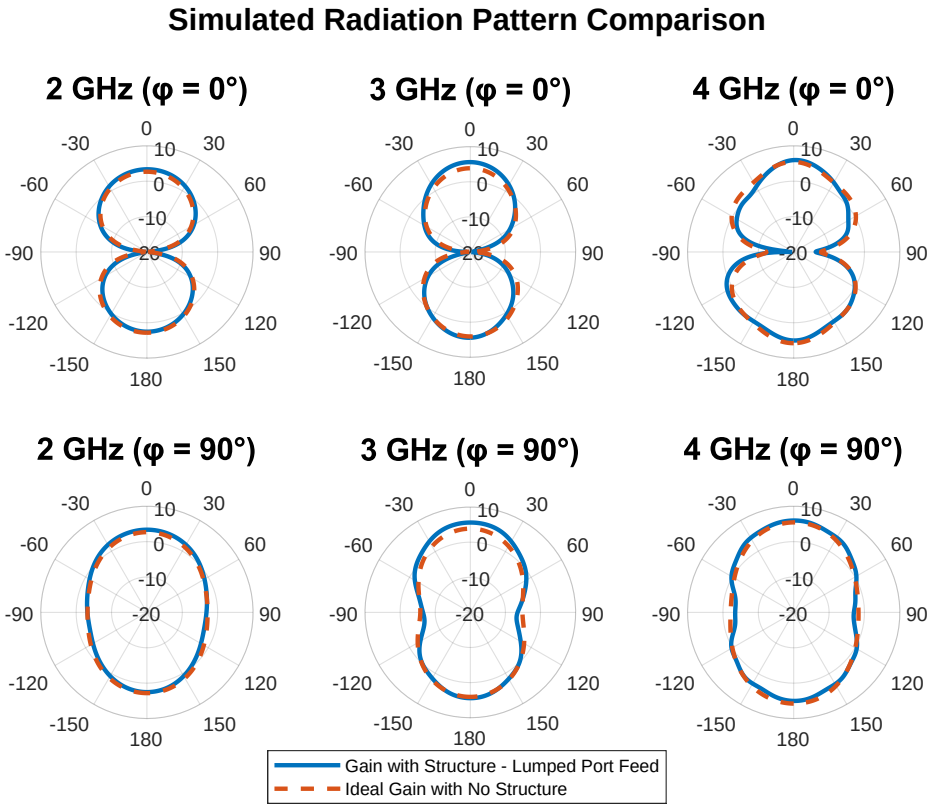

Figure 3.10: Comparison of simulated gain patterns of the free-floating plate design and the Prototype 2 mount and actuator design.

Table 3.1: Summary of broadside gain values for the tunable slot antenna. Comparison of simulated gain values of the free-floating plate design and Prototype 2 mount and actuator design.

	2 GHz	3 GHz	4 GHz
Gain with Structure ($\theta = 0°$)	2.76 dBi	5.09 dBi	4.42 dBi
Ideal Gain with No Structure ($\theta = 0°$)	2.06 dBi	3.44 dBi	3.95 dBi
Gain with Structure ($\theta = 180°$)	1.86 dBi	3.92 dBi	3.13 dBi
Ideal Gain with No Structure ($\theta = 180°$)	2.29 dBi	3.75 dBi	4.55 dBi

These results support the idea that the actuator and mount are small enough such that they do not significantly affect the pattern or match of the antenna. This is surprising, since at the highest frequency, the actuator itself is a metal box roughly a third of a wavelength long. However, the lack of impact, and to some extent improvement of gain, is a good result for the purposes of this project, so the next step of adding the balun was taken.

3.1.2 Mount, Actuator, and Balun Effects

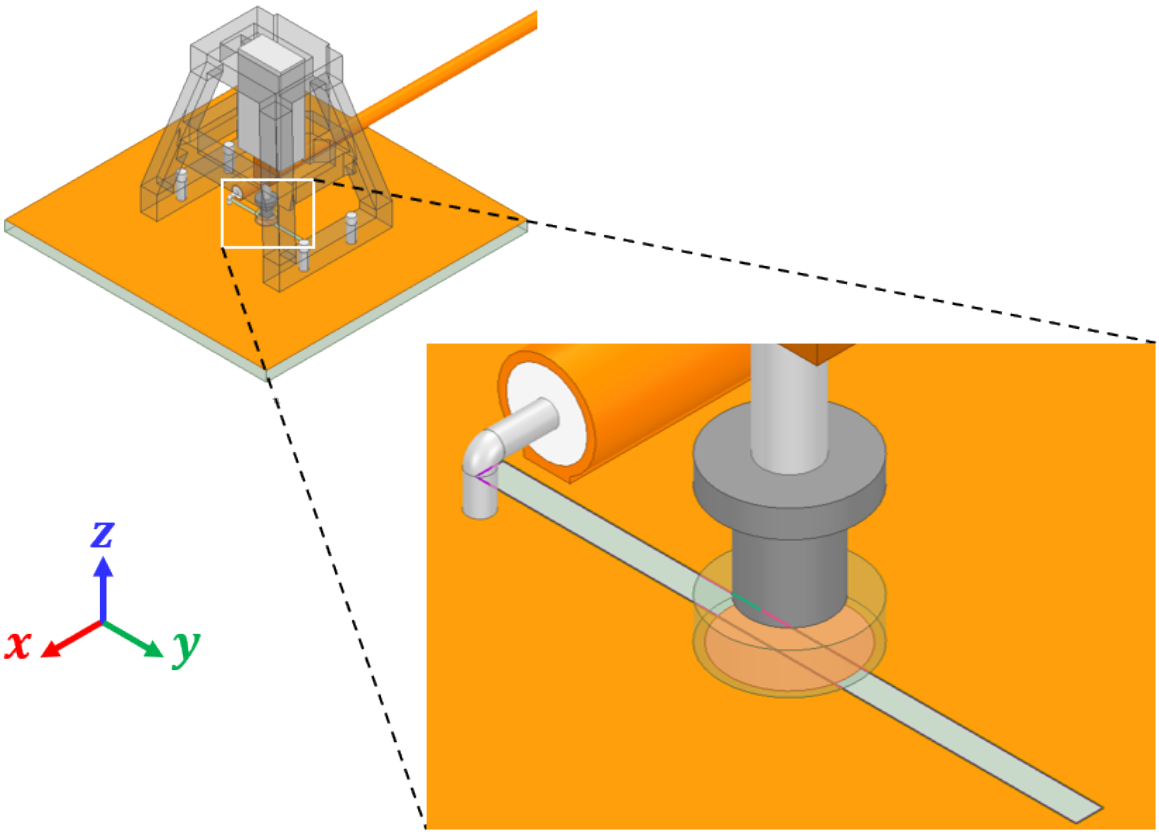

Figure 3.11: HFSS model of slot antenna with simplified mount, actuator, and Dyson balun feed. Includes close up of the feed connection to the slot antenna.

Continuing on with the design, a feeding system based off of a Dyson balun was added. A Dysun balun is a stripped coaxial cable (coax), with the center conductor bridging and then

shorting to the opposite side of the slot. A balun (a shortened version of a balanced-to-unbalanced transformer) is necessary to prevent cable currents from contributing unwanted radiation [37]. In the case of this antenna, currents going from the unbalanced coax to the balanced slot can instead travel back along the outside of the coax. The exterior currents can then radiate, causing a decrease in polarization purity and otherwise disrupting the desired radiation characteristics of the antenna. The outer conductor is soldered along the ground plane to encourage these exterior currents to dissipate into the ground plane instead of traveling back along the coax. The coax used in this project is the RG402/U Coax, and so the model included the stated dimensions of that coax. A depiction of the new antenna with balun is seen in Figure 3.11, including a zoomed-in section that shows the feed connection to the slot.

After the addition of the balun, simulations were again run to determine the effect on the performance of the antenna. The balun, as expected, affected all of the previously inspected parameters, but the effect was again small. The tuning range again changed, but in the opposite direction, resulting in a range from 15.5 μm to 227 μm, decreasing the tuning ratio to roughly 15:1. The match changed slightly, but in the opposite way, resulting in the reflection response, shown in Figure 3.12, moving back towards what it was like in the free-floating design. The rate of change of match also changed, indicating a less broadband match, which one would expect with a realistic feed versus an ideal port. The 10-dB return loss fractional bandwidth of the antenna increases with frequency, being 0.84% at 2 GHz, 2.18% at 3 GHz, and reaching 3.13% at 4 GHz.

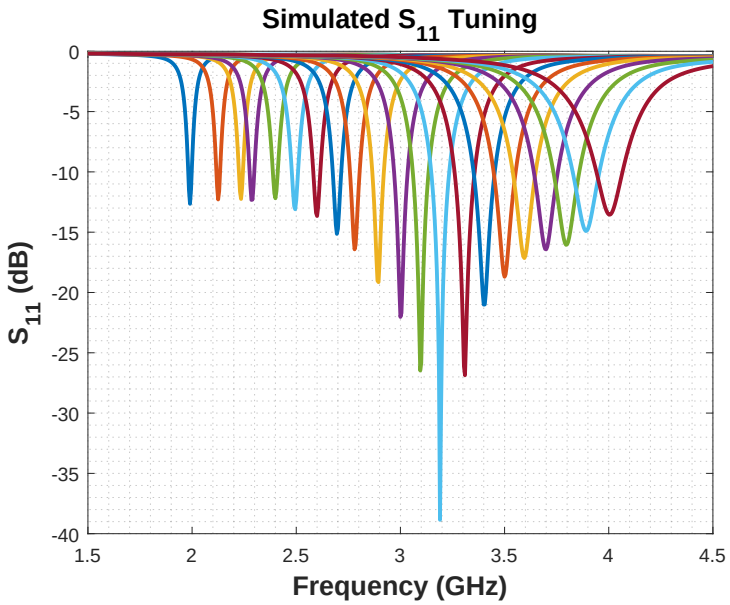

Figure 3.12: Simulated reflection response (S_{11}) of the loaded slot antenna with the Prototype 2 mount design and Dyson balun feed.

The radiation pattern also changed slightly, with an decrease in performance when comparing realized gain to gain of the free-floating design. This was expected, as mismatch loss is included in realized gain but not in normal gain, but the difference should be noted. In the direction of the mount, the broadside realized gain of the slot saw a roughly 0.15 dB increase on average over the gain from the free-floating plate design. Opposite the mount, the broadside realized gain saw a roughly 1 dB decrease on average. Qualitatively, the radiation pattern deflected more from ideal in general, with comparatively large deflections at the highest frequencies and about 35° off broadside. The comparative radiation pattern plots are shown in Figure 3.13 and more a more detailed numerical summary can be seen in Table 3.2..

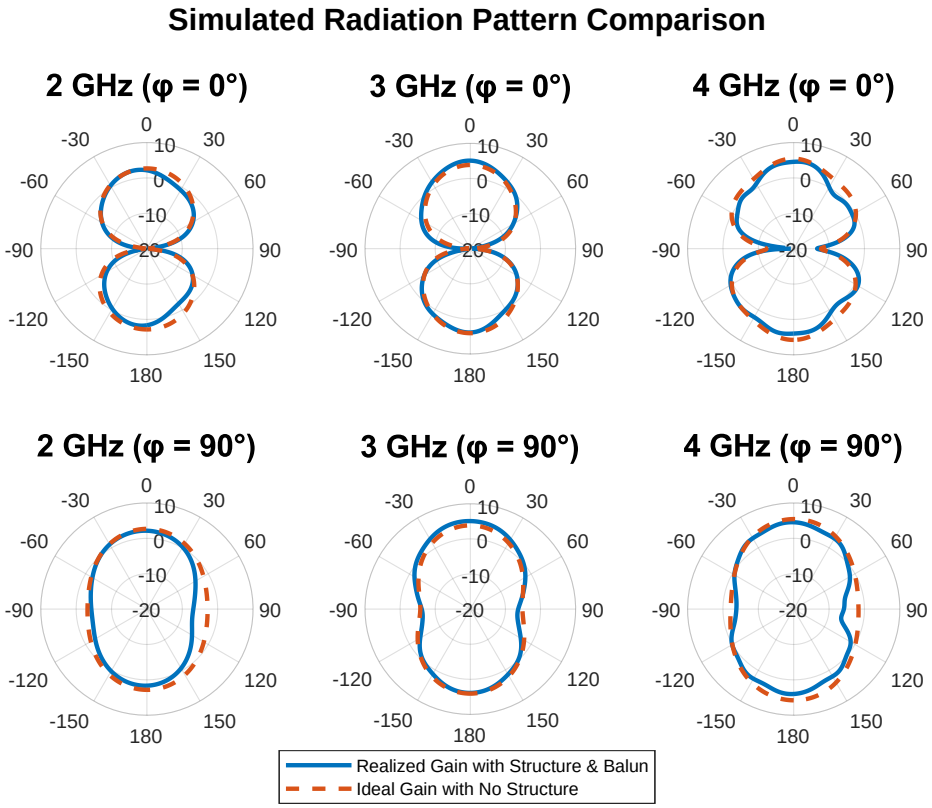

Figure 3.13: Comparison of simulated realized gain patterns of the free-floating plate design and the Prototype 2 mount, actuator, and balun design.

Table 3.2: Summary of broadside gain values for the tunable slot antenna. Comparison of simulated gain values of the free-floating plate design and Prototype 2 mount, actuator, and balun design.

	2 GHz	3 GHz	4 GHz
Realized Gain with Structure ($\theta = 0°$)	1.76 dBi	4.77 dBi	3.44 dBi
Ideal Gain with No Structure ($\theta = 0°$)	2.06 dBi	3.44 dBi	3.95 dBi
Realized Gain with Structure ($\theta = 180°$)	1.07 dBi	3.67 dBi	2.40 dBi
Ideal Gain with No Structure ($\theta = 180°$)	2.29 dBi	3.75 dBi	4.55 dBi

Following the analysis of radiation pattern and match, radiation efficiency was investigated to see the impact of the various elements. The resulting comparison is seen in Figure 3.14. The addition of the mount, actuator, and feed seem to have a minimal effect on the radiation efficiency of the antenna, with only a few percentage points decrease in overall efficiency at the worst, but an increase by a few points at the best.

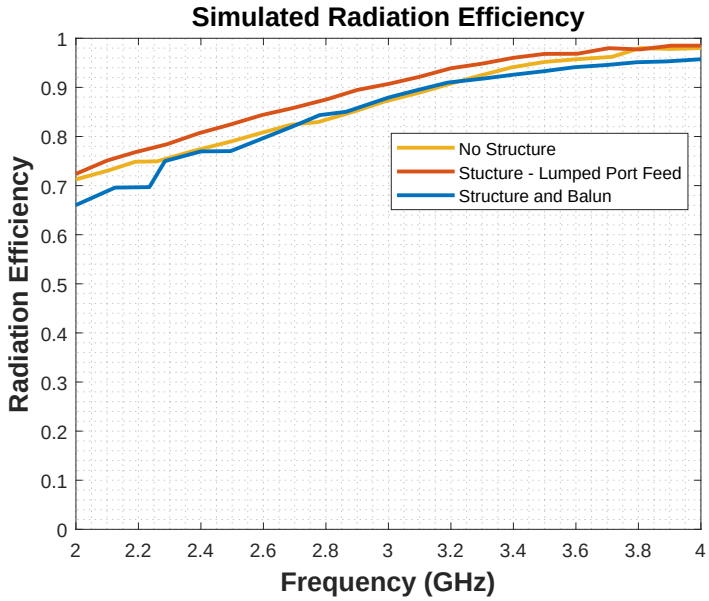

Figure 3.14: Simulated radiation efficiency over the 2-4 GHz tuning range. The structure slightly decreased the radiation efficiency overall, with a new minimum of 65.74% and new maximum of 95.75%.

With these promising simulation results, fabrication is necessary to verify simulation and show that the antenna functions as expected.

3.2 Piezo-Actuator Antenna Fabrication

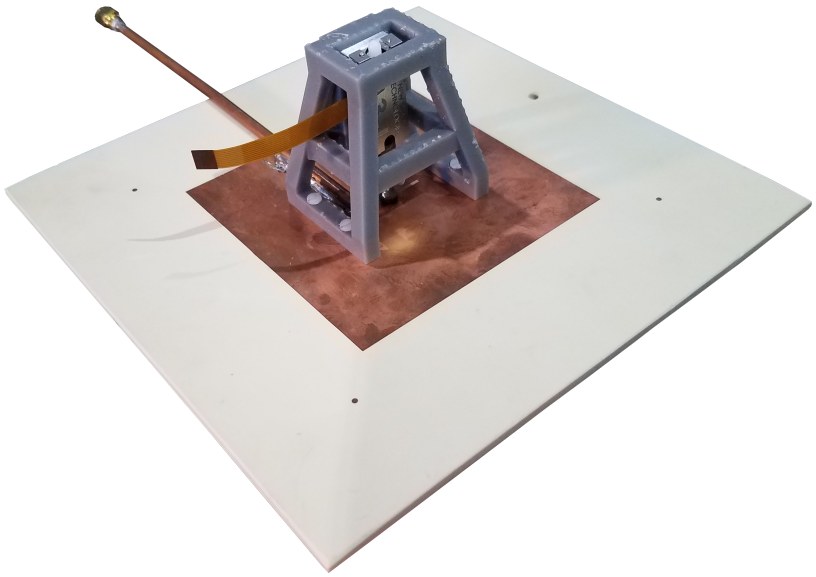

Figure 3.15: Photograph of the fabricated slot antenna with the tuning mechanism.

Following simulations verifying the capabilities of the antenna, the design was fabricated. The slot was etched from copper-clad 125-mil-thick TMM3 using photolithography. A balun was cut from a length of RG402/U Coax and soldered to the etched board. The mount for the piezo actuator was 3D printed using Grey Resin on a Formlabs Form 2 SLA Printer and attached to the substrate with nylon bolts and nuts. The capacitive plate was cut from a copper-clad 60-mil-thick RO4350B dielectric slab using a LPKF ProtoMat S103, forming a puck of copper-clad dielectric. Of particular sensitivity for the design is the mounting of the capacitive plate onto the piezo-actuator. Since the tuning changes significantly on the micrometer scale, a small departure from a perfectly parallel plate could result in different tuning performance. Great care was taken in mounting, with the sacrificial 'X' structure on the mount used for alignment. The puck was placed under the 'X' structure and the piezo-actuator, with screw attachment, was slowly lowered to the opposite side, but the screw attachment did not touch the puck. J-B Weld ClearWeld Quick Setting Epoxy was

used to bond the puck and actuator to the 'X' structure due to its high rigidity and lack of shrinkage while setting. A fully assembled version of the antenna and tuning structure is seen in Figure 3.15.

After fabrication, tunability testing was performed by measuring S_{11} with an Agilent Technologies N5225A PNA Network Analyzer. The fabricated antenna tunes fully from 2-4 GHz, with a greater than 8 dB return loss at each tuning point across the range. This is a little less than the standard 10 dB return loss, but could likely be improved with a better balun and more precise feeding. The feed point of the balun is highly sensitive, so by-hand alignment and soldering can skew the match. The response at various tuning points is seen in Figure 3.16.

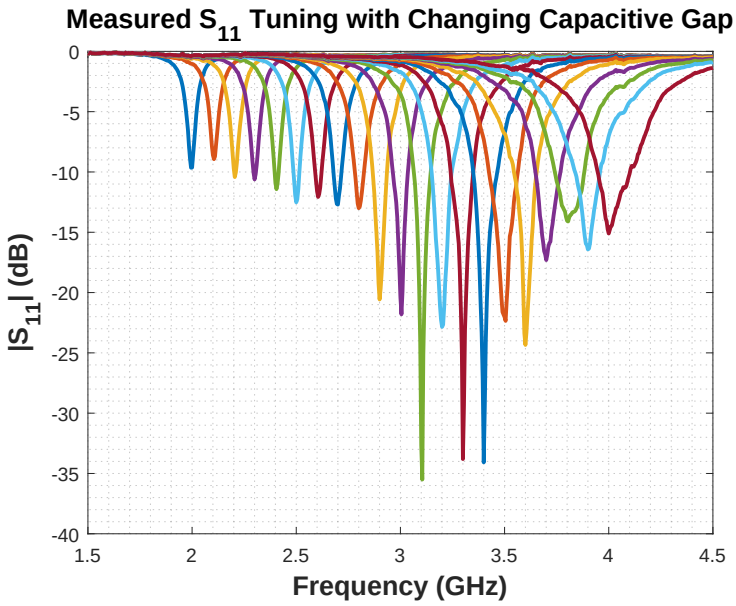

Figure 3.16: Measured reflection response (S_{11}) of the loaded slot antenna with the Prototype 2 mount design and Dyson balun feed.

The distance between the capacitive plate and slot ground plane could not be measured directly, so only relative distance was measured. Despite this, a rough comparison of frequency versus capacitive gap distance is seen in Figure 3.17. The antenna is highly

responsive at smaller distances, rapidly changing frequency with a small change in gap. As the gap size increases, the operational frequency changes less rapidly. This is expected as the relative difference in capacitance changes as the gap size increases. The two plots line up extremely well, lending confidence that the manufacturing methods used resulted in little error compared to simulation.

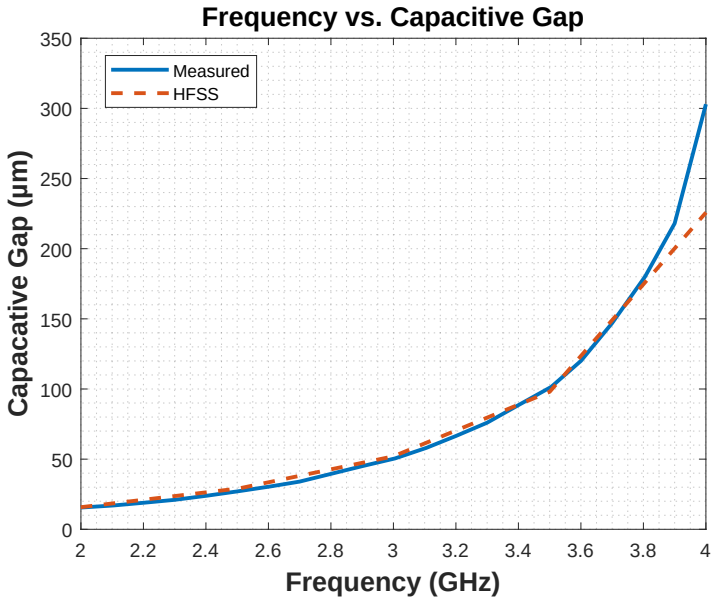

Figure 3.17: Operational frequency of the tunable slot antenna as a function of the capacitive plate offset from the ground plane. The simulated results are precise, while the measured results have an approximated starting gap of 15.5 µm, which is the same as simulation.

A comparison of S_{11} between measured and simulated results is seen in Figure 3.18, showing excellent agreement. The maximum return loss across the entire tuning range remained above 8 dB, which is a 7 dB reduction compared to the simulated results, but on average the plots line up extraordinarily well. The depth and shape of the reflection response matches well to simulation, again inspiring confidence in fabrication and simulation methods.

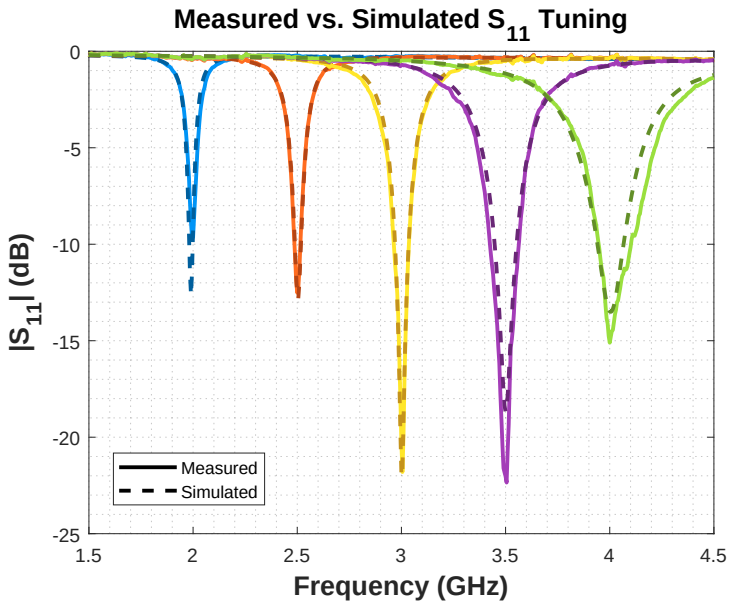

Figure 3.18: Comparison of the measured and simulated S_{11} response.

The final test to see if the antenna is truly performing as expected is to look at radiation patterns, specifically the realized gain. To this end, the antenna was put in an anechoic chamber, the chamber calibrated with calibration horns, and then the realized gain measured. The co-polarization and cross polarization were also measured to see the polarization purity of the antenna. Part of the measurement setup is shown in Figure 3.19. The mount is constructed from ROHACELL® 51 HFstructural foam to match air as much as possible. The setup also consists of a USB cable to control the actuator as well as a cardboard clamp to hold the antenna in place. The measurement setup includes structures to limit how much of the cable feeding the antenna was parallel to the main polarization direction, as the radiated fields can couple into the cable creating cable currents. These cable currents can effectively re-radiate waves that hit the cables, causing large variances in the radiation pattern and skewing the results.

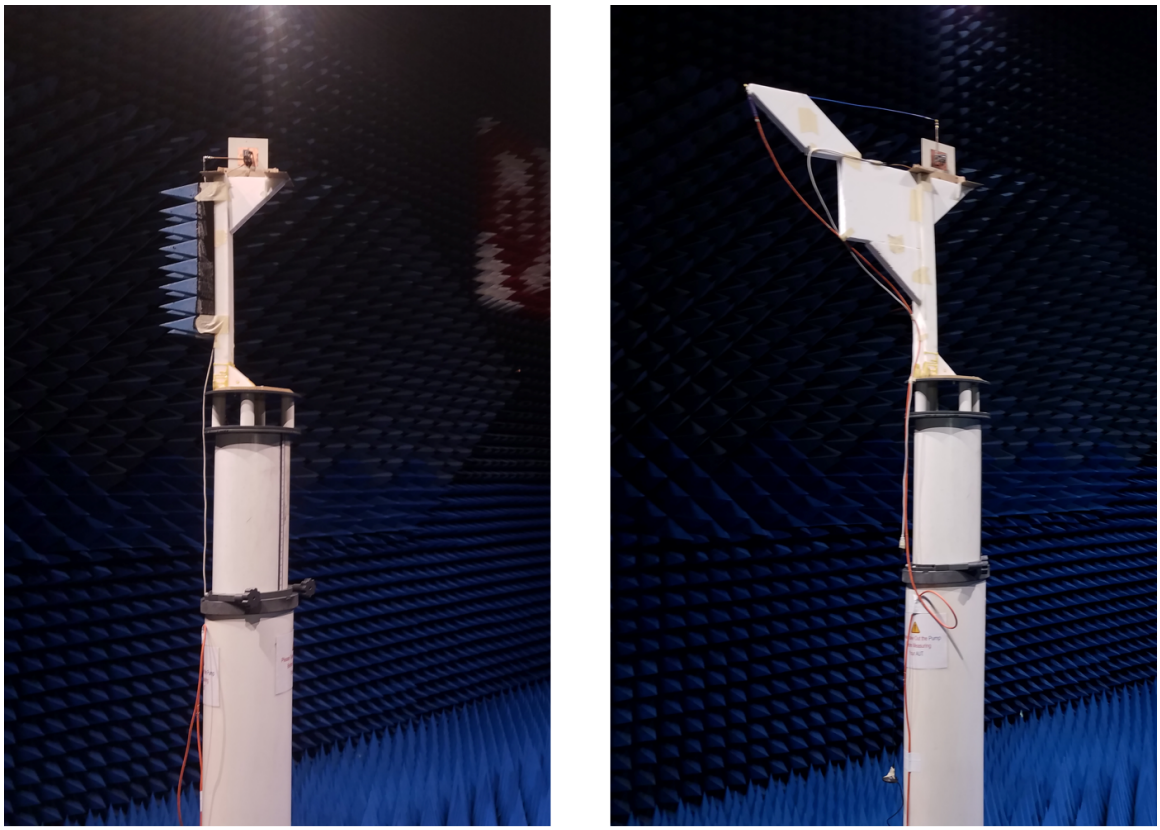

(a) (b)

Figure 3.19: Measurement setup for realized gain cut of the slot antenna. Note the variance in mount to limit cable interaction with the fields of the slot. The setup in (a) is for a vertically oriented, and thus horizontally polarized, slot antenna. The setup in (b) is for a horizontally oriented, and thus vertically polarized, slot antenna.

With this design in place, radiation pattern cuts at three different frequencies (2, 3, and 4 GHz) were taken. The results are summarized in Figures 3.20, 3.21, and 3.22. It can be seen that the general shapes line up fairly well in form and magnitude compared to simulation. There is some more variance in the intensity of the pattern, and that is likely due to measurement error introduced by the mount and cable. The cross-polarization is also much higher in the measured results, again likely due to the cable and mount interfering with the radiation pattern, as well as the balun not fully preventing unwanted cable currents. Despite

these issues, the antenna maintains roughly 15 dB of polarization purity on average across frequencies and angles. This is not exactly ideal for a functional system, but can likely be improved drastically by a better feed system, a better balun, and improved measurement.

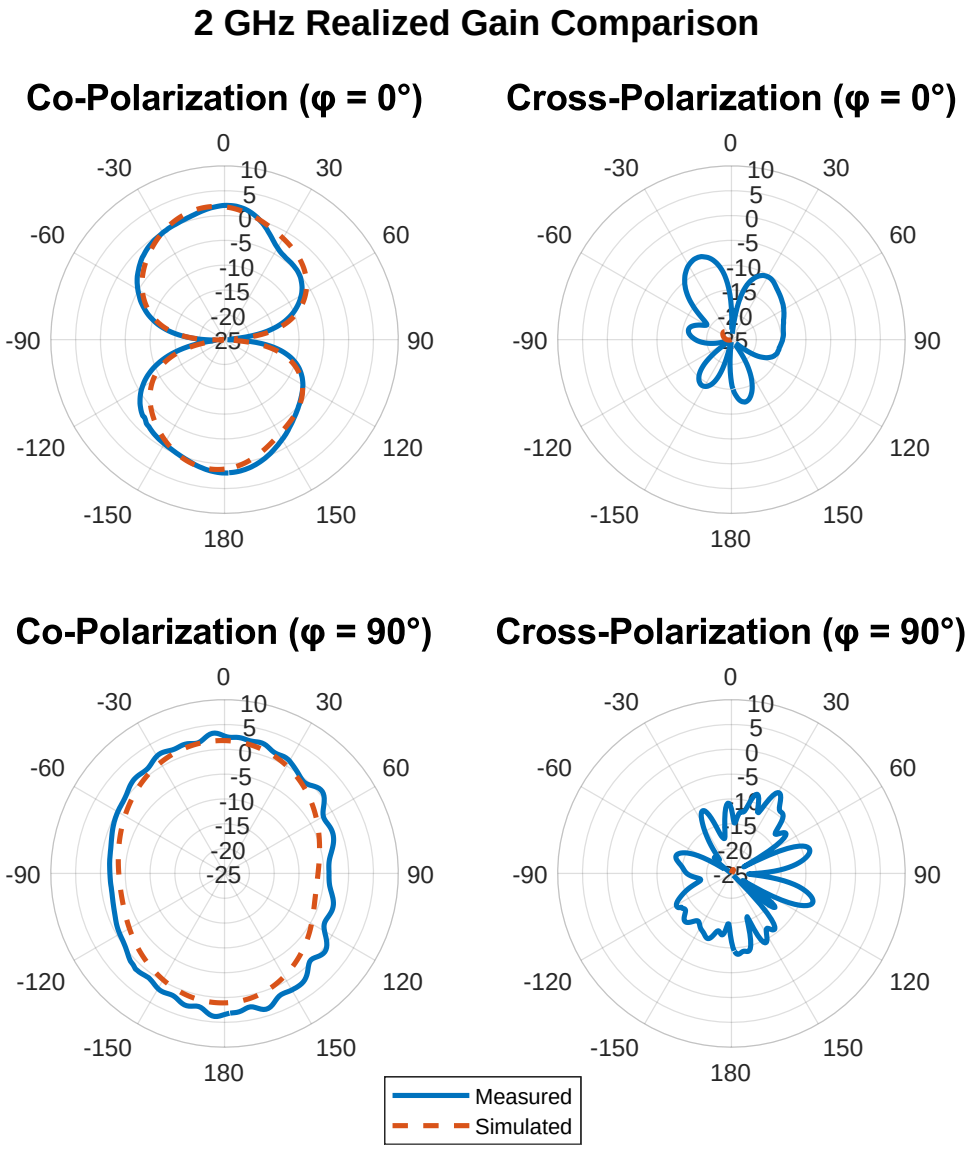

Figure 3.20: Realized gain pattern and polarization comparison at 2 GHz between the measured results and the simulated results of Prototype 2 with mount, actuator, and balun.

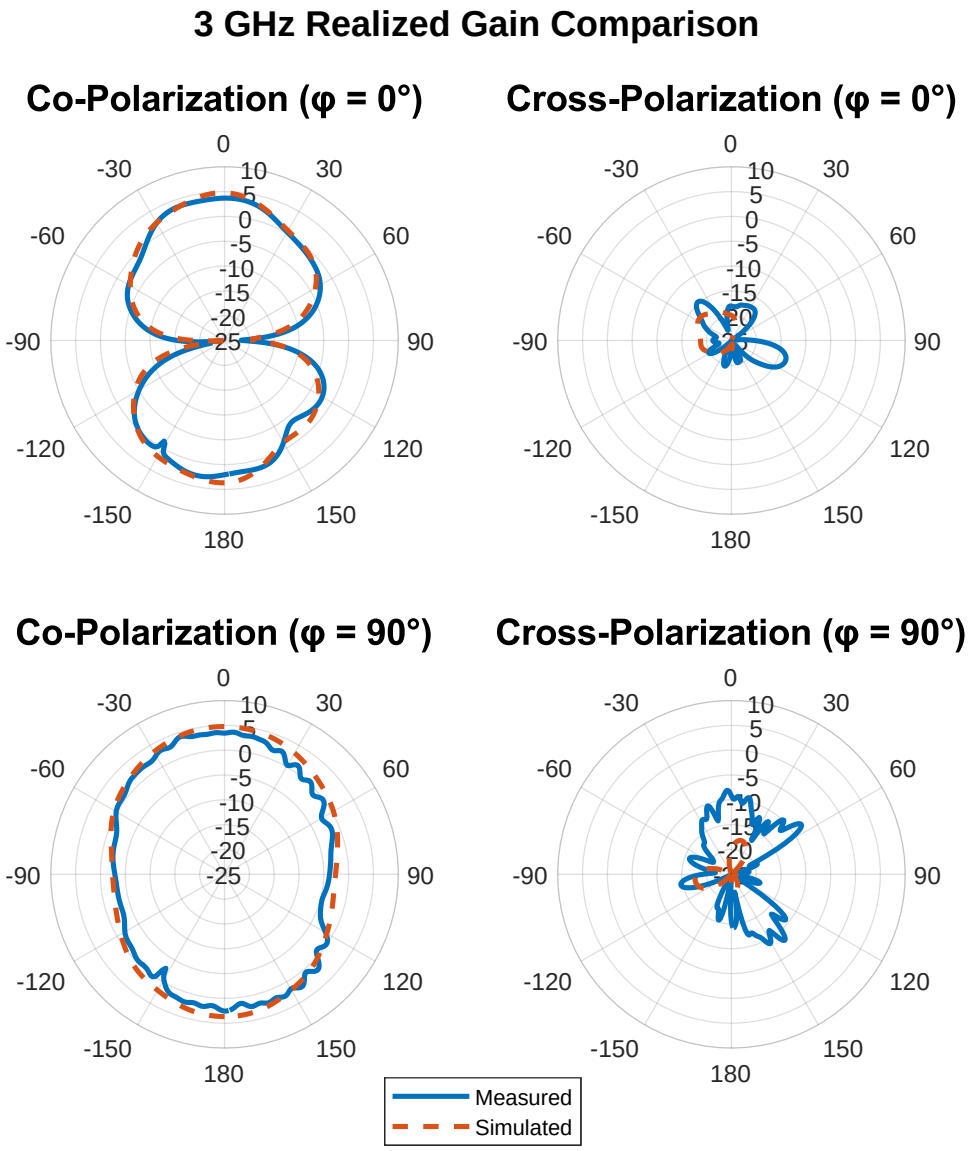

Figure 3.21: Realized gain pattern and polarization comparison at 3 GHz between the measured results and the simulated results of Prototype 2 with mount, actuator, and balun.

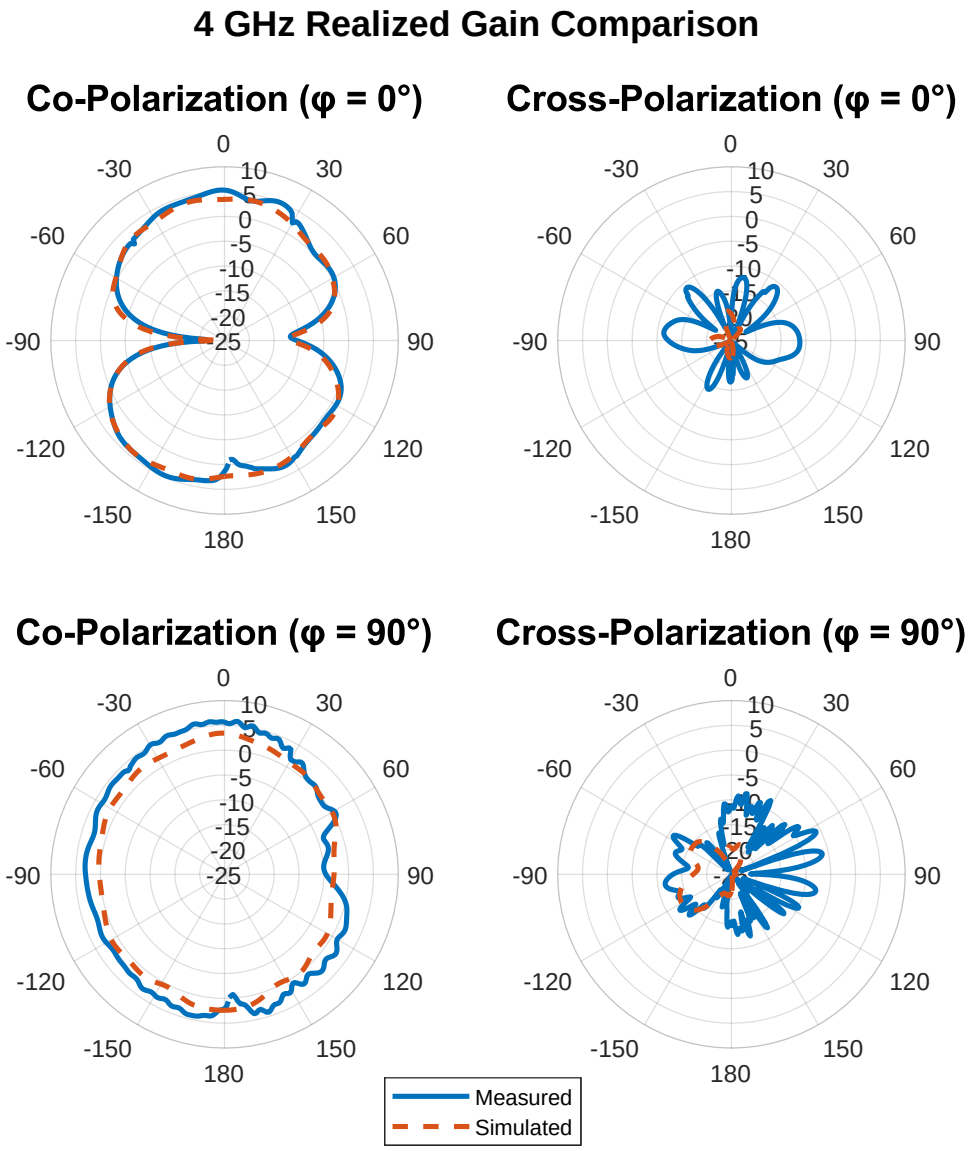

Figure 3.22: Realized gain pattern and polarization comparison at 4 GHz between the measured results and the simulated results of Prototype 2 with mount, actuator, and balun.

A summary of the measured and simulated values can be seen in Table 3.3. Note that due to variance in measurement, the realized gain values for the $\varphi = 0°$ cutplane and $\varphi = 90°$ cutplane at $\theta = 0°$ and $\theta = 180°$ did not agree perfectly. To account for this, the

values were averaged together. The values had an average difference of 0.67 dB with a maximum difference of 1.55 dB for the co-polarization. For the cross-polarization, the average difference was 6.61 dB, with a maximum difference of 8.85 dB.

Table 3.3: Summary of broadside realized gain values for the tunable slot antenna. Comparison of measured to simulated values. Measured values are averaged between the two cuts.

	2 GHz		3 GHz		4 GHz	
	Co-Pol	X-Pol	Co-Pol	X-Pol	Co-Pol	X-Pol
Measured Realized Gain (θ = 0°)	2.36 dBi	-14.19 dBi	3.55 dBi	-11.69 dBi	5.47 dBi	-13.75 dBi
Simulated Realized Gain (θ = 0°)	1.76 dBi	-23.63 dBi	4.75 dBi	-19.94 dBi	3.42 dBi	-19.70 dBi
Measured Realized Gain (θ = 180°)	2.70 dBi	-13.07 dBi	2.30 dBi	-17.72 dBi	1.73 dBi	-15.60 dBi
Simulated Realized Gain (θ = 180°)	1.07 dBi	-35.06 dBi	3.66 dBi	-23.30 dBi	2.39 dBi	-21.54 dBi

With these measurements, the concept was shown to closely match simulation and perform to expectation. This again inspired confidence in the accuracy of simulation going forward.

3.3 Power Handling Investigation

Similarly to Section 2.4, an investigation into the power handling of the antenna was warranted to determine its feasibility within a high-power setup. However, instead of using a model and Eigenmode simulations, the power handling can be directly predicted from scaling the results of a Driven Modal simulation. A Driven Modal simulation has a port with a selectable input power, allowing the determination of maximum input power from the maximum observed electric field strength in the device. The input power was left at the default of 1 W. The fields were extracted from the center of the capacitive gap to limit simulation artifacts that result in unrealistic peaks in electric field at sharp conductor/dielectric boundaries.

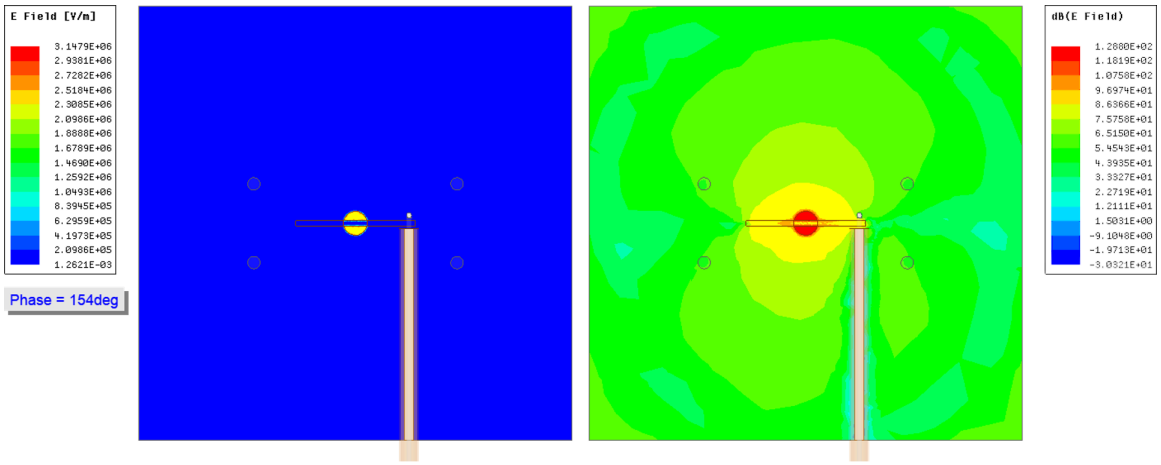

(a) (b)

Figure 3.23: Electric field strength and distribution in capacitive gap of slot antenna tuned to 2 GHz. The electric fields are represented in V/m (a) and in dB of V/m (b), highlighting the large concentration of fields below the capacitive plate of the antenna.

The resulting field distribution at 2 GHz can be seen in Figure 3.23. The electric field energy is highly concentrated below the capacitive plate of the antenna, and is correspondingly the location of highest field strength. Due to the planar nature and sharp edges of the capacitive plate and slot antenna, current crowding occurs on the outer ring and slot edges, leading to a stronger electric field presence. The maximum electric field in simulation was 3.1479 V/µm at 2 GHz, 0.7011 V/µm at 3 GHz, and 0.1030 V/µm at 4 GHz.

A simplified version of (2.18) was used to scale the power up to breakdown, becoming

$$P_{max} = \left(\frac{E_{br}}{E_{sim}}\right)^2 P_{sim} \tag{3.1}$$

where P_{max} is the predicted maximum power handling (or input power) of the antenna, E_{br} is the breakdown electric field strength (7.9 V/µm [36]), E_{sim} is the maximum observed electric field strength in the Driven Modal simulation, and P_{sim} is the input power

of the Driven Modal simulation (1 W). The maximum power handling was predicted to be 6.2981 W (37.9921 dBm) at 2 GHz, 126.9789 W (51.0373 dBm) at 3 GHz, and 5.8827 kW (67.6958 dBm) at 4 GHz. The power handling increases exponentially with frequency, leading to a rapid decrease in power handling for a highly loaded antenna. This confirms the trade-off between power handling and tunability.

3.4 Conclusion

A tunable slot antenna allows efficient operation in a noisy spectrum. The tunable antenna introduced in this chapter has been simulated and measured to tune over all of S-band. It does so while maintaining low disturbance in radiation pattern, low mismatch loss, and efficient operation. The antenna does all of this while maintaining the ability to handle high power applications without non-linear effects or the threat of breakdown. The measurements are shown to closely match simulation and demonstrate that HFSS is a valuable and accurate tool for the creation of these antennas. The tunable antenna was predicted to handle high power, with over 37 dBm for the entire tuning range, up to a maximum of 67 dBm at 4 GHz. After the demonstration of these antennas, a widely tunable cavity resonator and widely tunable antenna have both been demonstrated using mechanical tuning. Thus the building blocks of a filtenna have been demonstrated and what remains is to put them together.

Chapter 4

Time Domain Tuning

When creating multi-order filters, and by extension filtennas, one of the most important tools is one that enables intelligent tuning the filter to specification. No physical filter will come out exactly as predicted by closed-form equations, so some tuning is almost always necessary for high-performance filters. In order to tune a filter, however, there has to be some semblance of being able to determine what is wrong with the filter so that that error can be fixed. Trial and error is a potential solution, but it is excessively time intensive and cannot guarantee the desired outcome. The issue is exacerbated with passive symmetric filters. In these filter designs, two different issues can produce *identical* S-parameter responses. Take a 4$^{\text{th}}$ order Chebyshev filter with f_0 of 1 GHz, Δf of 50 MHz, and return loss ripple (L_R) of 20 dB, as an example. The prescribed filter response is shown in Figure 4.1.

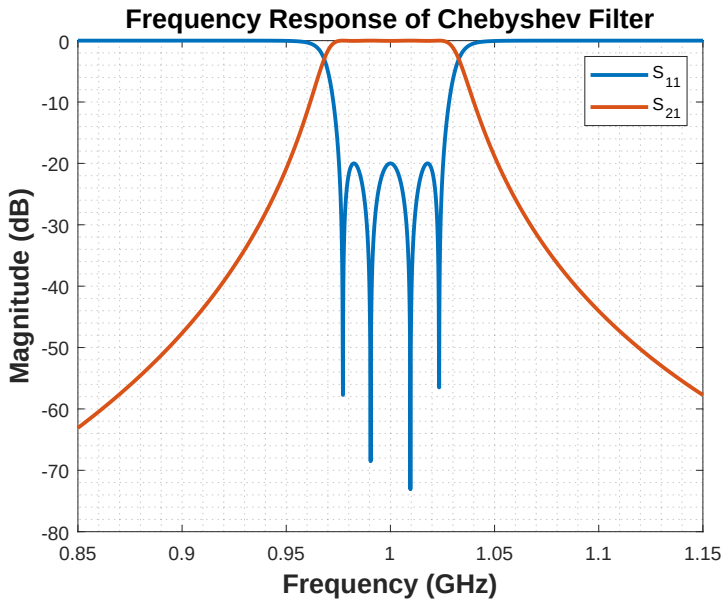

Figure 4.1: Frequency response of 4$^{\text{th}}$ order Chebyshev filter (f_0 = 1 GHz, Δf = 50 MHz, L_R = 20 dB).

If one of the resonators is mistuned, the filter response will be distorted. In one case, the second resonator was mistuned to 990 MHz by increasing the capacitance. In another case, the third resonator was mistuned to 990 MHz by increasing the capacitance. Both changes result in an identical magnitude plot of the S-parameters, which is shown in Figure 4.2. Without some way of characterizing the filter, it would take a fair amount of trial and error to get to the correct response.

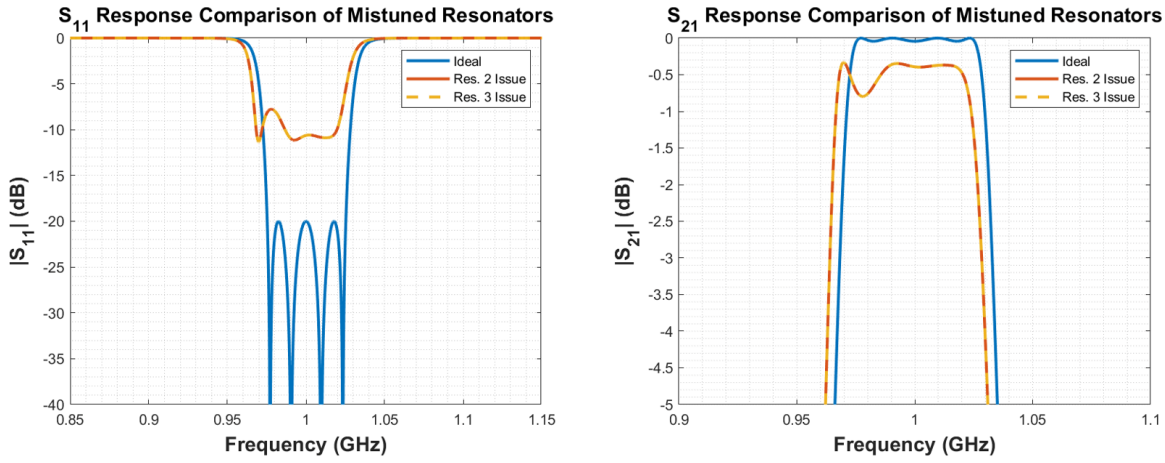

(a) (b)

Figure 4.2: S_{11} (a) and S_{21} (b) response of 4$^{\text{th}}$ order Chebyshev filter (f_0 = 1 GHz, Δf = 50 MHz, L_R = 20 dB). Each resonator at issue is tuned to 990 MHz instead of 1 GHz.

There exists a plethora of different ways to characterize a filter to figure out where in particular a problem exists. However, to the best of the author's knowledge, all but one rely on having access to both the input and output port of the filter. This presents an issue for a filtenna, where only one port is easily accessible; the second port for a filtenna is free space. It is technically possible to use another antenna to create a two port system, but that doubles the complexity of the system, making it that much more difficult to characterize the filtenna. With another antenna, specialized equipment, such as an anechoic chamber, is also necessary to limit outside interference and get accurate results.

The one method that relies on a single port is known as 'Time Domain Tuning' (TD tuning) and was created by Dunsmore [44] and expanded upon by Burger [45]. Given a complex valued return loss (S_{11}) of a filter, the time domain method can give insight into which resonator or coupling is mistuned and in which direction. The method takes the inverse Fourier transform of a windowed frequency domain signal to see these traits. There

are additional criteria that the data must meet, but if properly set up it is a powerful tool for filtenna design.

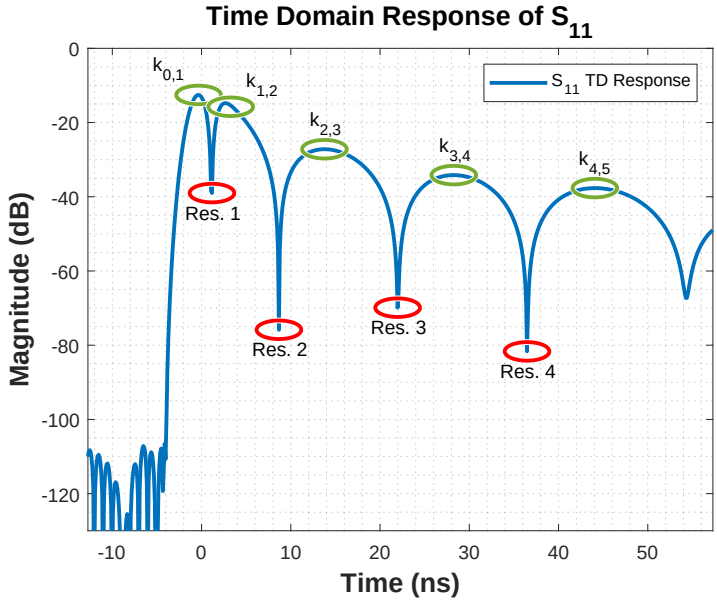

Figure 4.3: Time domain transform of frequency domain S_{11} with labels for particular points. The 'humps' of the signal correspond to coupling within the filter, while the nulls correspond to the resonators.

The TD response of the S_{11} of the example Chebyshev filter is shown in Figure 4.3. The peaks in the response each correspond to a single coupling. The first 'hump' is representative of the input coupling of the filter ($k_{0,1}$), while each hump in between a resonator null represents inter-resonator coupling ($k_{i,i+1}$). The hump after the last resonator is the output coupling of the filter ($k_{n,n+1}$). A filter is better tuned the more the humps line up with the ideal. The nulls in the response represent the resonant frequency of each of the resonators (f_{0i}). The deeper the null, the closer the resonator is to the center frequency of the filter. Unfortunately, this does not reveal which direction, higher or lower, that the resonator is mistuned. That detail is revealed in the 'group delay' of the time domain, shown in Figure 4.4.

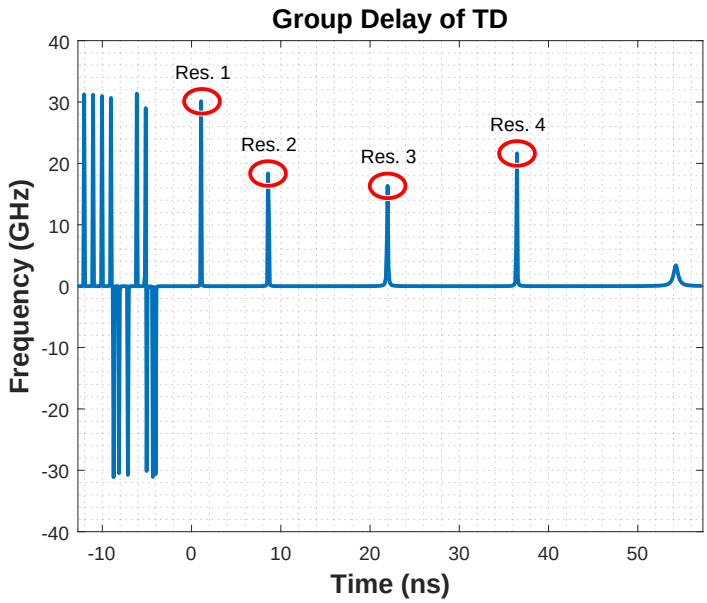

Figure 4.4: Group delay of time domain transform of S_{11}

Each peak in the group delay occurs at the same time as the nulls in the normal TD response. These peaks also correspond to a filter element resonating. The larger the magnitude of the peak, the closer to resonance. However, if the resonator is tuned below the center frequency, the peak will be negative. If the resonator is tuned above the center frequency, the peak will be positive, but lesser in magnitude. Typically, the peaks before time $t = 0$ are a result of ringing and can be ignored. Therefore, based on the sign and intensity of the peak, tuning of a filtenna can be accomplished intelligently by pattern matching.

To return to the previous example, the time domain response of each error trace compared to ideal is shown in Figure 4.5. Figure 4.5a depicts a response where everything is correctly tuned except for Resonator 2, which is set at 990 MHz by a higher than designed capacitance. Figure 4.5b depicts a response where everything is correctly tuned except for Resonator 3, which is set at 990 MHz by a higher than designed capacitance.

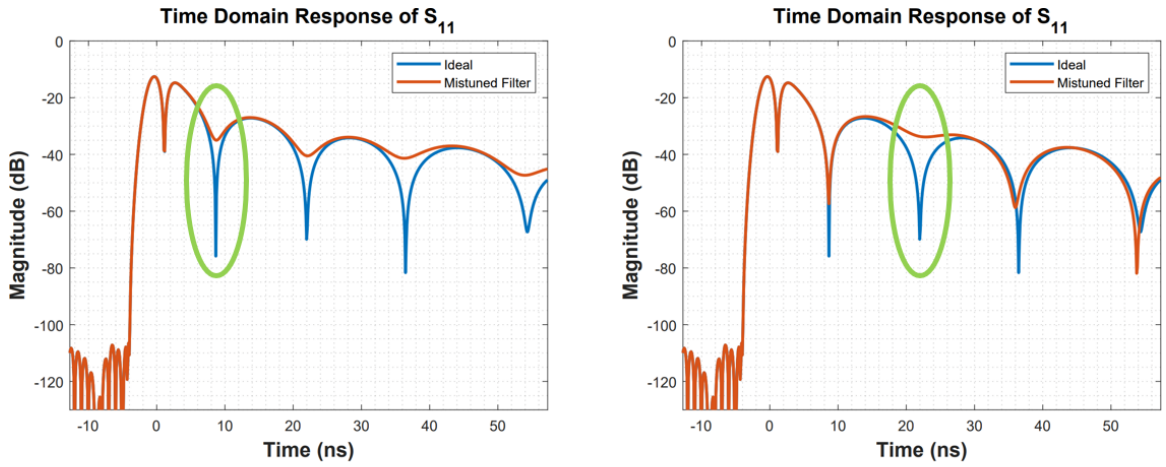

Figure 4.5: Time domain transform of S_{11} with Resonator 2 set to 990 MHz (a) and Resonator 3 set to 990 MHz (b). The mistuned resonator in each is indicated with a green oval.

Note that each of these plots in the frequency domain gave exactly the same result, yet in the time domain the responses are quite different. The response for a mistuned Resonator 2 diverges from ideal at the second zero, while the response for a mistuned Resonator 3 diverges greatly at the third zero, both indicating which resonator is out of tune.

With this brief introduction to the TD method, a more nuanced approach is warranted. First, the mathematical theory behind the method will be covered, along with the requirements for data shaping. Following the mathematical overview, there will be a deep dive into working with the TD method, showing how various errors can be identified in the TD response and corrected. These include examples of over and under coupling and examples of mistuned resonators. A few general considerations and limitations will also be discussed.

4.1 Time Domain Method Theory

The fundamental building block of the TD method is the inverse Fourier transform, more specifically, the inverse discrete Fourier transform (IDFT). This transformation allows the extraction of what is essentially the time domain reflectrometry of a banded pulse into the antenna. The IDFT for our purposes is defined as

$$T[t] = \frac{1}{N} \sum_{i=0}^{N-1} F_i e^{j2\pi f_i t}, \tag{4.1}$$

where F_i is the value of the frequency domain function at f_i frequency, where i represents the index value. The time domain function, $T[t]$, is sampled at t time and N is the number of points sampled of the frequency domain function. F_i and f_i are discretely sampled values, where the vectors containing all N samples are denoted $\boldsymbol{F}$ and $\boldsymbol{f}$, respectively.

Within this transform, if $\boldsymbol{F}$ is complex valued, the maximum range of time that can be represented, T_s, is identical to the sampling rate of the frequency domain function. So, assuming the condition of equally spaced an in order samples is met, the relation becomes

$$T_s = \frac{1}{\Delta f} = \frac{1}{f_1 - f_0}, \tag{4.2}$$

where Δf is the distance between frequency samples, and f_0 and f_1 are the first and second frequencies, respectively. Note that these are *not* the same as Δf_{3dB} and f_0 used in Chapter 2.

In addition, the time resolution, Δt, or the minimum gap in time that can be directly determined from the frequency domain function, follows from the bandwidth of the sampled signal, or

$$\Delta t = \frac{1}{BW} = \frac{1}{f_{N-1} - f_0} = \frac{T_s}{N}, \tag{4.3}$$

where BW is the bandwidth of the samples, and f_0 and f_{N-1} are the first and last frequencies, respectively. Dunsmore recommends having a frequency bandwidth that is two to five times the expected passband bandwidth of the filter in order to guarantee sufficient resolution to see individual resonators.

Traditionally, the range of t is stated as from 0 to T_s, but it can be between any two points of time as long as the difference in time does not exceed T_s. Going beyond that total range will lead to an aliased signal, where the signal repeats over again as the same value as at $t - T_s$. The bound of T_s also serves as an upper limit; it is not always necessary to go the full range. Therefore, for any given arbitrary starting time, t_0, the full IDFT becomes

$$T[t] = \frac{1}{N} \sum_{i=0}^{N-1} F_i e^{j2\pi f_i t} \qquad \text{for} \quad t = t_0 + k\Delta t, \quad k = 0, 1, ..., N-1. \tag{4.4}$$

However, despite a fundamental limit on the information available being in steps of Δt, the IDFT can be oversampled to increase the number of data points. This functions as interpolation between points, but is useful when trying to see narrow peaks, as will be necessary with the TD method. In this work, an *oversample factor* is included, which scales the number of points by some integer multiple x, resulting in

$$T[t] = \frac{1}{N} \sum_{i=0}^{N-1} F_i e^{j2\pi f_i t} \qquad \text{for} \quad t = t_0 + \frac{k\Delta t}{x}, \quad k = 0, 1, ..., x(N-1). \tag{4.5}$$

When the sampled frequency domain function, $\boldsymbol{F}$, is the reflection coefficient, S_{11}, there is another consideration that must be taken into account. For a bandpass filter/filtenna, S_{11} at the edges of the measured band converges to a magnitude of 1. When combined with the assumption of the IDFT that everything not in band is magnitude 0, this creates a sharp transition in the signal. Since many frequencies are required to represent a sharp transition, this creates an artifact called 'ringing' in the time domain response, obscuring much of

the information in the TD response. This problem can be addressed partially through a process called 'windowing', where the edges of the sampled response are gradually tapered down to zero, preventing the sharp transition and therefore significantly limiting ringing. Windowing comes with a trade-off of smoothing of the data, often hiding key pieces of information. Fortunately, due to the nature of the TD method, smoothing is not as much of a concern since pattern matching is the end goal. The window function, W is generated with the desired number of points and then multiplied point-wise by the frequency domain function.

A Nuttall defined, 4-term symmetric Blackman-Harris window was used as the window function, but the reader is encouraged to experiment with windowing functions and see the effects. The Nuttall defined, 4-term symmetric Blackman-Harris window is generated as

$$W_i = a_0 - a_1 \cos\left(\frac{2\pi i}{N-1}\right) + a_2 \cos\left(\frac{4\pi i}{N-1}\right) - a_3 \cos\left(\frac{6\pi i}{N-1}\right) \quad \text{for} \quad i = 0, 1, ..., N-1, \tag{4.6}$$

where a_0 = 0.3635819, a_1 = 0.4891775, a_2 = 0.1365995, and a_3 = 0.0106411. The windowed IDFT then becomes

$$T[t] = \frac{1}{N} \sum_{i=0}^{N-1} W_i F_i e^{j2\pi f_i t} \qquad \text{for} \quad t = t_0 + \frac{k\Delta t}{x}, \quad k = 0, 1, ..., x(N-1). \tag{4.7}$$

For the TD method used here specifically, there are a few more quirks that must be addressed. First, the signal in IDFTs is assumed to be baseband, that is, that the signal is centered around 0 Hz. When looking at bandpass filters/filtennas, the reflection coefficient, S_{11}, is almost always measured in a banded fashion, as in starting at some positive frequency and then ending at some other positive frequency. To correct for this problem, a frequency shift can be applied to the data (which is a phasor multiple in the time domain).

The only change in the plots generated will be a DC shift to zero in the group delay of the time domain plot, but this will allow the sign of that plot to determine the direction of tuning.

Second, the center frequency of the filter must be at the center of the sampled band of frequencies. *The TD method will tune the resonators in a system to whatever frequency appears as the center frequency of the data*, so for a traditional Butterworth or Chebyshev filter, the center frequency of the filter must also be the center of the data. Combining this center frequency condition with the above baseband shift, a frequency shift of the filter center frequency is required.

Third, with real systems, there is often a length of line in between the filter and the sampling point, leading to a phase offset in the data. This can be removed through deembeding, which is a time shift, t_d, in the data. Since a time shift is the same as a phasor multiplication in the frequency domain, this must also must be accounted for in the IDFT to ensure accurate tuning. In practice, deembeding is best performed by shifting t_d until the slope on the left (negative in time) side of the k_{01} coupling hump is lined up with ideal.

Lastly, in practice most of the full TD response is not needed to tune the filter. Only a small subsection of T_s is required. Given some filter with a center frequency f_0, a fractional bandwidth FBW, and an order n, Dunsmore gives an estimated start time, t_0, and end time, t_{end}, of

$$t_0 = -\frac{2}{\pi f_0 FBW} \tag{4.8a}$$

$$t_{end} = \frac{2n+1}{\pi f_0 FBW} \tag{4.8b}$$

Combining all of these criteria together, the full IDFT for the TD method becomes

$$T[t] = \frac{1}{N}\sum_{i=0}^{N-1} W_i F_i e^{j2\pi(f_i - f_0)(t-t_d)} \qquad \text{for} \quad t = t_0 + \frac{k\Delta t}{x}, \\ k = 0, 1, 2, ... \quad \text{where} \quad t_0 \leq t \leq t_{end}. \tag{4.9}$$

In the TD method, F_i is the complex, linear value of S_{11} at a particular f_i frequency. Thus, $T[t]$ is becomes the complex, linear, windowed, time domain transform of S_{11}. Taking the magnitude (in dB) will result in graphs like that of Figure 4.3, from which the resonator and coupling accuracy can be assessed. To determine the resonator tuning direction, a group delay plot like Figure 4.4 is needed. The group delay of the time domain is extracted identically to the group delay of the frequency domain, where it is the slope of the phase angle with respect to frequency. Therefore, the group delay of the time domain response , $\tau_{T[t]}$, is

$$\tau_{T[t]} = -\frac{\partial \arg\left(T[t]\right)}{\partial t}. \tag{4.10}$$

4.2 Tuning Coupling

As explained by Dunsmore, the coupling between elements of the filter directly appears in the TD response. However, Dunsmore only talks about the change in intensity of the coupling, not the accompanying resonator null time shift. Anecdotal evidence supports the idea that using resonator null time shift may be the best way to determine correct coupling.

In general, given that every element before is correctly tuned, over-coupling will result in a TD response that is *lower* than ideal and shift the following resonance zeros *earlier* in time. Under-coupling will result in a TD response that is *higher* than ideal and shift the following resonance zeros *later* in time. Intuitively, this can be explained by the idea that over-coupled systems are more broadband, so less energy is reflected and so the reflection

coefficient magnitude is smaller. It is worth noting that in Dunsmore's work, there is not a corresponding time shift with over/under coupling, yet it always seems to appear in practice. With these design guidelines in place, it becomes apparent when coupling is mistuned on a properly deembeded response.

To demonstrate case studies of common situations, a few examples of mistuned coupling follow. Input coupling and inter-resonator coupling are mistuned in both directions, and their resulting graphs are depicted.

4.2.1 Input Coupling Tuning

The first possible error (after mismatch loss) that can happen is mistuned input coupling, k_{01}. An under-coupled response is seen in Figure 4.6a, while an over-coupled response is seen in Figure 4.6b.

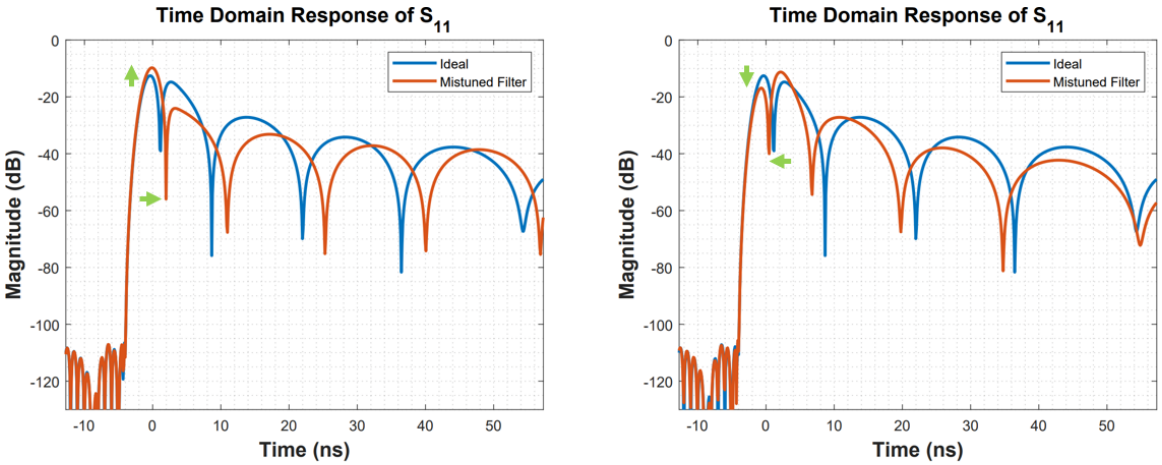

Figure 4.6: Time domain transform of S_{11} with the input coupling, k_{01}, decreased by 50% (a) and increased by 50% (b). The green arrows indicate the direction the mistuned filter response moved away from ideal.

Notice how in Figure 4.6a, the first hump overshoots the ideal hump, while in Fig-

ure 4.6b, the hump undershoots the ideal hump. These responses line up perfectly with what is expected from under/over coupling, and indeed, the coupling factor, k_{01}, is decreased by 50% in Figure 4.6a and increased by 50% in Figure 4.6b.

4.2.2 Inter-resonator Coupling Tuning

The other type of coupling error that can occur is inter-resonator coupling. Figure 4.7a depicts an error where Resonator 1 and 2 are under-coupled, while Figure 4.7b depicts a case where Resonator 1 and 2 are over-coupled.

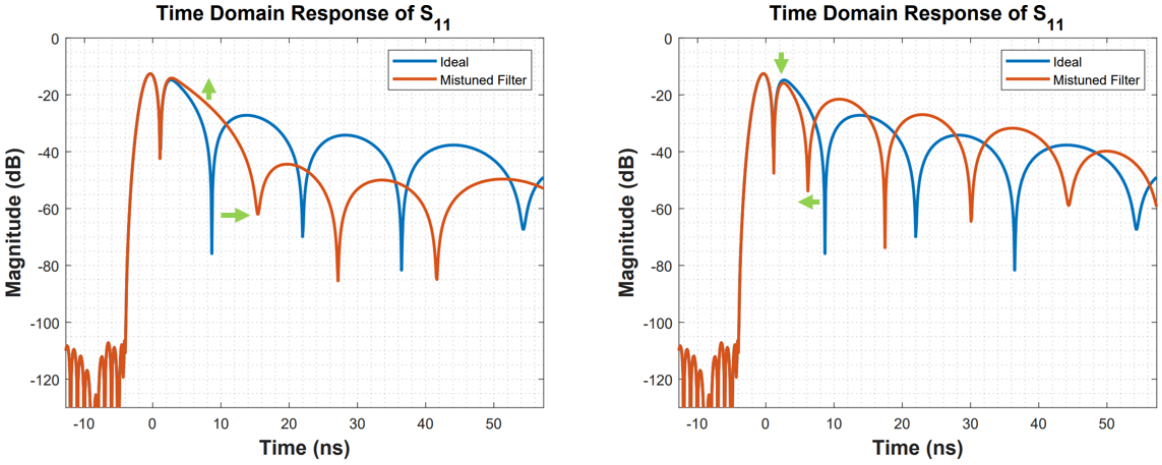

Figure 4.7: Time domain transform of S_{11} with the first inter-resonator coupling, k_{12}, decreased by 50% (a) and increased by 50% (b). The green arrows indicate the direction the mistuned filter response moved away from ideal.

Just as expected, in Figure 4.7a, the first hump overshoots the ideal hump, while in Figure 4.7b, the hump undershoots the ideal hump. These responses line up perfectly with what is expected from under/over coupling, and indeed, the coupling factor, k_{12}, is decreased by 50% in Figure 4.7a and increased by 50% in Figure 4.7b.

These examples give an indication of what to look for when applying the TD method

to coupling within a filter, but coupling is only part of the building block of a filter; tuning resonators is key for the filter performance.

4.3 Tuning Resonators

Resonator frequency is an essential part of the tuning performance. As shown before, it is relatively easy to tell which resonator is mistuned by where the time domain response first diverges from ideal, but seeing whether the resonator is tuned high or low requires more nuance. Figure 4.8 depicts the same filter as before with the first resonator mistuned. In Figure 4.8a, the resonator is tuned low by 5%, with a new frequency of 950 MHz. In Figure 4.8b, the resonator is tuned high by 5%, with a new frequency of 1050 MHz.

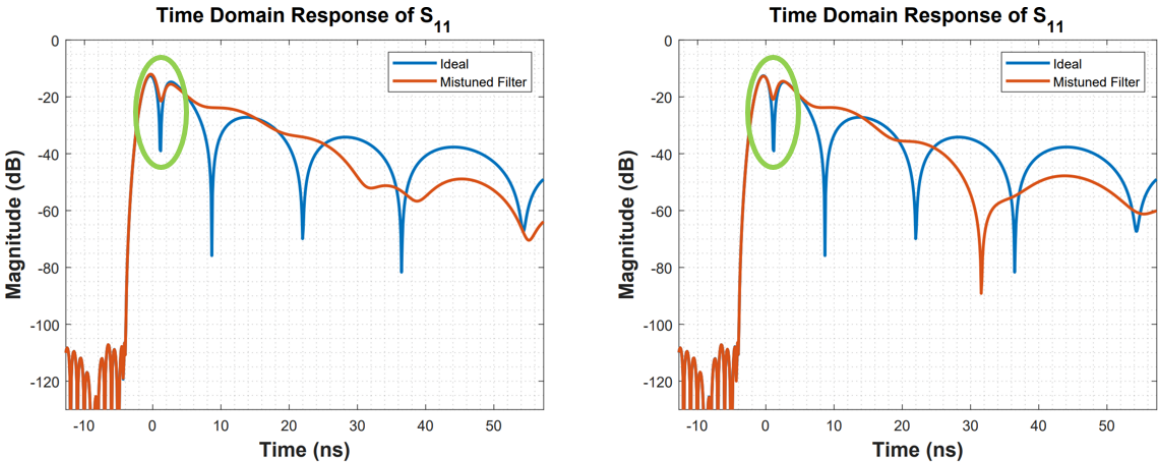

Figure 4.8: Time domain transform of S_{11} with the first resonator decreased in frequency by 5% (a) and increased in frequency by 5% (b). The mistuned resonator in each is indicated with a green oval.

While there are significant differences in the response after the 3rd zero, for the most part the TD response of both mistuned resonators looks similar. All that has changed to

indicate an issue is that the TD response in both has diverted from ideal by decreasing the depth of the zero.

However, by referencing the group delay of the time domain response (4.10), the direction of error can be determined. In Figure 4.9a, the peak associated with the first resonator is negative and less in magnitude than ideal, indicating the first resonator is below the ideal frequency. In Figure 4.9b, the peak associated with the first resonator is positive and less in magnitude than ideal, indicating the first resonator is above the ideal frequency.

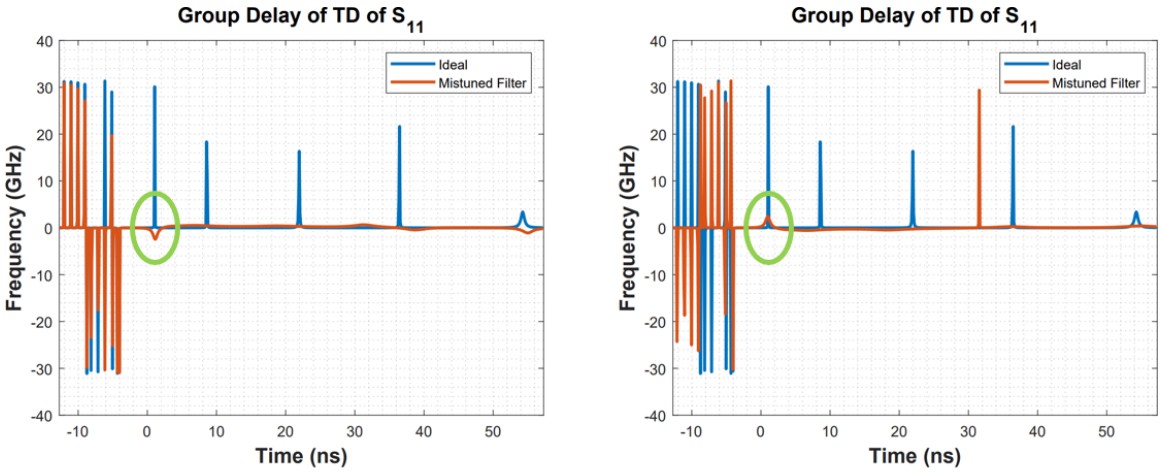

Figure 4.9: Group delay of TD transform of S_{11} with the first resonator decreased in frequency by 5% (a) and increased in frequency by 5% (b). The mistuned resonator in each is indicated with a green oval.

Using a combination of the TD response and the group delay of the TD response, it becomes a simple process to iterate through the resonators and see how they need to be adjusted to tune the filter design. Recommendations for this methodology are outlined in the following section.

4.4 Proposed Methodology for Tuning & Limitations

In practice, it is very helpful to have the first resonator already close to perfectly tuned, as this makes detecting the time and magnitude shifts much easier for input coupling. Luckily, this can be done even when the input coupling is slightly mistuned, as maximizing the depth of the zero makes the resonator more tuned, regardless of the input coupling.

Following the first resonator tuning, the input coupling can be tuned close to ideal. However, tuning the input coupling will necessarily change the loading of the first resonator, and may cause some degree of mistuning. This can again be adjusted for. This back and forth can continue for as long as the designer wishes, but normally stabilizes within two resonator tuning steps.

Next, it is helpful to jump ahead to the next resonator/coupling pair, k_{12} and Resonator 2. Again, adjusting Resonator 2 so that the zero is as deep as possible, then adjusting k_{12} is the easiest process. Another back and forth may happen as these adjustments mistune each other slightly, but they may also cause Resonator 1 and k_{01} to change in tuning. Again, this can be stepped back through, and will converge in few steps, but repeated tuning is necessary for best performance. In addition, the further the particular element is from another, the less effect it will tend to have on the loading of the other element. So, tuning Resonator 2 will barely affect k_{01} compared to k_{12}, but if Resonator 2 is out of tune by a large margin, adjustments will need to be made across the board.

This iterative process of continually stepping up in resonator/coupling pairs continues until the last resonator. Then, all that is left is the output coupling. This can be tuned on a typical filter, but it is unknown how to tune the output coupling on a filtenna.

It is absolutely necessary that resonators and coupling earlier in the chain are tuned as well as possible before proceeding down the chain, or the further information will be obscured by earlier errors. For this reason, the TD method is limited for higher order

filters. In practice, one cannot perfectly tune a filter, and so later resonators/couplings will become more and more obscured by accumulated error. In a traditional filter, this can be partially solved by looking at the reflection response from the second port, but with a filtenna that is not an easy option. Therefore, the TD method becomes less powerful as the order increases. However, it is more than capable of tuning filtennas of 2nd or 3rd order, and is likely to be extendable beyond that.

Additionally, the best of the author's knowledge, the TD method does not have any expedient method of parameter extraction. It is purely a pattern match method and thus cannot be used to easily figure out how much each particular element is mistuned. This limitation combined with the inherently iterative nature of the TD method can make it more time intensive than other filter tuning techniques. In the case a filter is excessively badly tuned, the TD method may also struggle to provide insight. However, for the purposes of tuning a filtenna, it is unrivaled.

4.5 Conclusions

The time domain method provides a look into the inner workings of filters using only the S_{11} magnitude and phase data. Specific element error can be isolated without access to a second port, and direction relative magnitude of that error can be determined.

The method has several requirements: the center frequency of the filter must be at the center of the sampled band, the sampled band must have sufficient bandwidth, and there must be enough samples to cover the time range of interest. Additionally, there are a few limitations. The method suffers from error accumulation and is iterative in nature, increasing time that is required to use it.

The TD method, however, offers a look inside the inner workings of a filtenna like no other known method. Multi-order filtennas, which previously were typically tuned by trial

and error, can be tuned intelligently and with purpose. This is a powerful tool that has far reaching implications for the future of filtenna design.

Chapter 5

Filtenna Concept, Theory, and Prototype

Traditionally, wide-band microwave systems rely on a single wide-band antenna connected to a switchable bank of filters. This filter bank provides excellent frequency response characteristics, but at discrete steps in frequency. More recently, there has been a large amount of research into tunable filters, as they allow an entire filter bank to be replaced by a single filter that can change its frequency response. This saves on size, weight, and often power (SWaP), which is ideal in a plethora of applications from smartphones to satellites. It is common in these systems to treat the antenna as a separate entity, bolted on and entirely disjoint from the filter system.

Breaking from this norm allows for the conceptualization of a filtenna, which couples the fields of the filter and antenna together to get better performance in a smaller package. A filtenna consists of a filter and antenna coupled together in a unique way. In previous chapters, tunable resonators and tunable antennas were demonstrated, so the creation of a tunable filtenna should only be a matter of creating an adequate electromagnetic coupling mechanism.

In order to fully realize a filtenna, there are a few key steps. First, an abstract model is helpful to design the desired response. Fortunately, filter design theory is already well established and can be applied directly to filtenna design. The maturity of the filter design work-flow allows it to be readily applied, making filtenna design much easier. There are

many great resources for filter design theory, such as [46] and [12], but an overview will be given below.

Second, a method of coupling into the fields of the antenna must be developed. Doing so allows the antenna to act as a resonator in a traditional filter design. This can be accomplished in many ways, but a cavity backed tunable slot design will be presented.

Third, a method of coupling into the resonators from outside the system must be developed and explored. A shorted CPW line has been used to feed evanescent-mode cavities [4], [6], [12], but the design space has not been thoroughly documented. An exploration of the various design parameters and their impact will be explored.

Fourth, the inter-resonator coupling must be tuned. This can be an arduous process, especially for cavities that are not symmetric. A method based on Eigenmode simulations will be presented that is quick and does not rely on symmetry.

Lastly, all of these lessons will be combined to create an example filtenna. The antenna will be tuned from 2-4 GHz, display a 2^{nd} order frequency response in both S_{11} and broadside realized gain, and be manufacturable using PCB design techniques. A time-domain method will be applied for final tuning of the filtenna. Previous work has applied the method to tuning filtennas [21], [24], but to the best of the author's knowledge, this is the first time the TD method has been applied to frequency agile filtennas.

5.1 Prototype Filters

Filter design theory has progressed to the point where one can go from a simple set of requirements to a fully fledged filter with relative ease. The first step is to design an abstract prototype. The abstract prototype filter response is filter geometry independent, with the mathematical equivalents of ideal capacitors and inductors used as building blocks. This overview will expressly be covering how to design basic, mainline-coupled prototypes,

with the 'why' being left up to the reader to search for within themselves. References [7], [46], [47] were used for the creation of this material.

The design a prototype filter follows three steps. First, a low-pass prototype is generated based on the order (n) and, if a Chebyshev, the desired ripple. This low-pass prototype is defined by a set of values known as 'g-coefficients', of which there are $n + 2$. Second, the low-pass prototype is scaled to the desired frequency range and response type. The filter prototype at this stage is represented in a structure known as a coupling matrix. Lastly, the complex scattering parameters (S-parameters) are extracted from the coupling matrix, showing the final filter design.

5.1.1 Low-Pass Prototype Generation

To create a low-pass prototype, all that is needed is n in the case of a maximally flat, or Butterworth type filter. In the case of a Chebyshev, either passband ripple (L_A) or return loss ripple (L_R) must also be known. For a Butterworth filter, the g-coefficients can be found as

$$g_0 = g_{n+1} = 1, \tag{5.1a}$$

$$g_r = 2\sin\left(\frac{(2r-1)\,\pi}{2n}\right) \qquad \text{for } r = 1, 2, ..., n. \tag{5.1b}$$

For a Chebyshev design, the process is a little more complicated. The g-coefficients are defined following

$$g_0 = 1, \tag{5.2a}$$

$$g_1 = \frac{2}{\eta}\sin\left(\frac{2}{2n}\right), \tag{5.2b}$$

$$g_{r+1} = \frac{4\sin\left(\frac{(2r-1)\,\pi}{2n}\right)\sin\left(\frac{(2r+1)\,\pi}{2n}\right)}{g_r\left(\eta^2 + \sin^2\left(\frac{r\pi}{n}\right)\right)} \qquad \text{for } r = 1, 2, ..., n-1, \tag{5.2c}$$

$$g_{n+1} = \begin{cases} 1 & \text{for } n \text{ odd} \\ \varepsilon + \sqrt{1+\varepsilon^2} & \text{for } n \text{ even and } S_{11}(0) \geq 0\ , \\ \dfrac{1}{\varepsilon + \sqrt{1+\varepsilon^2}} & \text{for } n \text{ even and } S_{11}(0) \leq 0 \end{cases} \tag{5.2d}$$

where η is defined as

$$\eta = \sinh\left(\frac{1}{n}\sinh^{-1}\left(\frac{1}{\varepsilon}\right)\right). \tag{5.3}$$

The ripple factor, ε, depends on the desired ripple, and can be defined by either L_A or L_R following

$$\varepsilon = \sqrt{10^{\frac{L_A}{10}} - 1} \tag{5.4a}$$

$$\varepsilon = \frac{1}{\sqrt{10^{\frac{L_R}{10}} - 1}} \tag{5.4b}$$

where L_A and L_R are expressed in decibels (dB). The ripple factor, ε, is completely separate from the ε_r and ε_0 relating to dielectric permittivity. It is important to note that Chebyshev coefficients differ from Butterworth in that they must be solved iteratively, as the g_{r+1} coefficient relies on the g_r coefficient.

These g-coefficients represent the non-scaled inductor or capacitor values of a low-pass filter prototype. This prototype has a cutoff frequency (f_c or ω_c) of 1 rad/s and input impedance of 1 Ω. The next step is to scale the prototype to the desired frequency range and response type.

5.1.2 Frequency Scaling and Coupling Matrix

A low-pass filter prototype can be scaled to a low-pass filter, high-pass filter, bandpass filter, or bandstop filter at any arbitrary cutoff or center frequency, fractional bandwidth, and impedance. Since the end goal of this prototype synthesis is to generate idealized S-parameters, the system is assumed to be perfectly matched and capacitor and inductor

values will not be calculated. Therefore, impedance scaling is not necessary and will be skipped over. Further discussion of impedance scaling can be seen in [12], [46], [47]. The range of desired frequencies, f_{sweep}, needs to be normalized, or scaled, to be incorporated with the g-coefficients. Also, in order to model the response computationally, f_{sweep} must be discretely sampled into a frequency vector, $\boldsymbol{f}$ with length m. For low-pass and high-pass filters, a frequency vector ($\boldsymbol{f}$), and cutoff frequency (f_c) are necessary for frequency scaling. For bandpass and bandstop filters, a frequency vector ($\boldsymbol{f}$), center frequency (f_0), and fractional bandwidth (Δ) are necessary for frequency scaling. The scaled frequency vector, $\boldsymbol{F}$, follows

$$\boldsymbol{F} = \begin{cases} \dfrac{\boldsymbol{f}}{f_c} & \text{for Low-Pass Filters} \\ -\dfrac{f_c}{\boldsymbol{f}} & \text{for High-Pass Filters} \\ \dfrac{1}{\Delta}\left(\dfrac{\boldsymbol{f}}{f_0} - \dfrac{f_0}{\boldsymbol{f}}\right) & \text{for Bandpass Filters} \\ -\Delta\left(\dfrac{\boldsymbol{f}}{f_0} - \dfrac{f_0}{\boldsymbol{f}}\right)^{-1} & \text{for Bandstop Filters} \end{cases}, \tag{5.5}$$

The scaled filter can be represented in matrix format, a design referred to as an *extended coupling matrix*, denoted here as $\boldsymbol{A}$. The extended coupling matrix is an $(n+2) \times (n+2)$ matrix and is made up of several distinct parts,

$$\boldsymbol{A} = \boldsymbol{R} + S\boldsymbol{U} + j\boldsymbol{M}, \tag{5.6}$$

where $\boldsymbol{R}$ represents the normalized port impedances, $S\boldsymbol{U}$ represents the scaled frequency values *at a single point*, j is the imaginary unit, and $\boldsymbol{M}$ represents the coupling matrix. $\boldsymbol{A}$ is only valid at a single frequency. Incorporating $\boldsymbol{F}$ into a third dimension creates an extended coupling matrix with some bandwidth. The matrix has dimensions $(n+2) \times (n+2) \times m$

with components

$$\boldsymbol{A}_{3D} = \boldsymbol{R}_{3D} + \boldsymbol{\Omega} + j\boldsymbol{M}_{3D}. \tag{5.7}$$

$\boldsymbol{R}_{3D}$ and $\boldsymbol{M}_{3D}$ are identical to $\boldsymbol{R}$ and $\boldsymbol{M}$, but have been duplicated m times across the third dimension, while $\boldsymbol{\Omega}$ represents the frequency scaled values matrix.

R_S	0	0	$\cdots$	0	0	0
0	0	0	$\cdots$	0	0	0
0	0	0	$\cdots$	0	0	0
$\vdots$	$\vdots$	$\vdots$	$\ddots$	$\vdots$	$\vdots$	$\vdots$
0	0	0	$\cdots$	0	0	0
0	0	0	$\cdots$	0	0	0
0	0	0	$\cdots$	0	0	R_L

Figure 5.1: Representation of $\boldsymbol{R}$. In a perfectly matched system, $R_{0,0} = R_{n+1,n+1} = 1$.

For this project, the ports are always assumed to be ideally matched, and so $\boldsymbol{R}$ is an $(n+2) \times (n+2)$ zero matrix except for $R_{0,0} = R_{n+1,n+1} = 1$. A representation of this is seen in Figure 5.1.

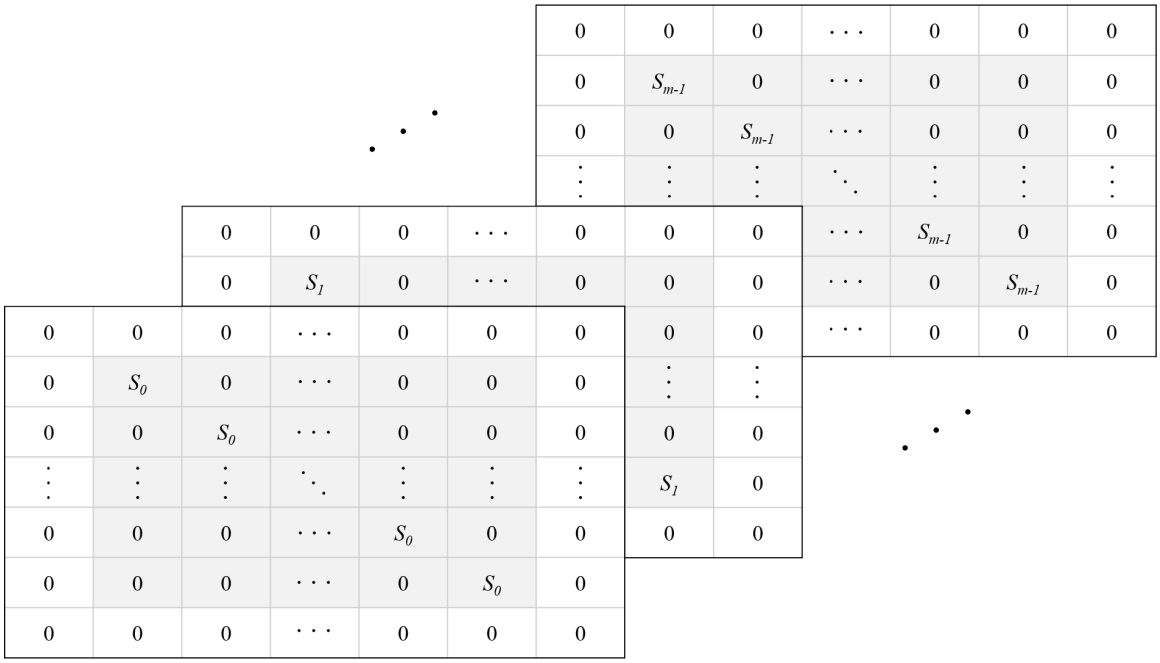

Figure 5.2: Representation of $\boldsymbol{\Omega}$, where each individual $(n+2) \times (n+2)$ matrix is an $S\boldsymbol{U}$ matrix.

$\boldsymbol{\Omega}$ is effectively a vector of $S\boldsymbol{U}$ matrices of length m. Each $S\boldsymbol{U}$ matrix is a modified identity matrix ($U_{0,0}$ and $U_{n+1,n+1} = 0$, all else the same) multiplied by a single value of $\boldsymbol{S}$, creating a scalar multiple. $\boldsymbol{S}$ takes into account frequency scaling, becoming

$$\boldsymbol{S} = j\boldsymbol{F}. \tag{5.8}$$

In the bandpass case, the finite Q of each resonator can be taken into account by adding on a real component to $\boldsymbol{S}$, where

$$\boldsymbol{S} = j\boldsymbol{F} + \delta, \tag{5.9a}$$

$$\delta = \frac{1}{\Delta Q_u}. \tag{5.9b}$$

The resolution can be broken down further, where each δ represents the unique Q_u of each

resonator. However, filters often have identical resonators and the Q's are often treated as equal, hence one value for δ. To show an example, in the bandpass case with finite Q resonators, $\boldsymbol{S}$ becomes

$$\boldsymbol{S} = \frac{j}{\Delta}\left(\frac{\boldsymbol{f}}{f_0} - \frac{f_0}{\boldsymbol{f}}\right) + \frac{1}{\Delta Q_u} \tag{5.10}$$

$\boldsymbol{M}$ is the coupling matrix, and is a powerful tool in filter design. It can be used to model any given coupling between elements of the filter, allowing for the creation of non-symmetric filter patterns, additions of transmission zeros, and much more. This $(n+2) \times (n+2)$ full matrix is seen in Figure 5.3a. However, for this initial filter response generation, only mainline coupling, or coupling from element to element in a single path through the filter, needs to be represented. Therefore, most of the values of $\boldsymbol{M}$ go to zero, with only the diagonal above and below the main diagonal having non-zero value. This reduced coupling matrix is seen in Figure 5.3b.

$M_{0,0}$	$M_{0,1}$	$M_{0,2}$	$\cdots$	$M_{0,n-1}$	$M_{0,n}$	$M_{0,n+1}$
$M_{1,0}$	$M_{1,1}$	$M_{1,2}$	$\cdots$	$M_{1,n-1}$	$M_{1,n}$	$M_{1,n+1}$
$M_{2,0}$	$M_{2,1}$	$M_{2,2}$	$\cdots$	$M_{2,n-1}$	$M_{2,n}$	$M_{2,n+1}$
$\vdots$	$\vdots$	$\vdots$	$\ddots$	$\vdots$	$\vdots$	$\vdots$
$M_{n-1,0}$	$M_{n-1,1}$	$M_{n-1,2}$	$\cdots$	$M_{n-1,n-1}$	$M_{n-1,n}$	$M_{n-1,n+1}$
$M_{n,0}$	$M_{n,1}$	$M_{n,2}$	$\cdots$	$M_{n,n-1}$	$M_{n,n}$	$M_{n,n+1}$
$M_{n+1,0}$	$M_{n+1,1}$	$M_{n+1,2}$	$\cdots$	$M_{n+1,n-1}$	$M_{n+1,n}$	$M_{n+1,n+1}$

(a)

0	$M_{0,1}$	0	$\cdots$	0	0	0
$M_{1,0}$	0	$M_{1,2}$	$\cdots$	0	0	0
0	$M_{2,1}$	0	$\cdots$	0	0	0
$\vdots$	$\vdots$	$\vdots$	$\ddots$	$\vdots$	$\vdots$	$\vdots$
0	0	0	$\cdots$	0	$M_{n-1,n}$	0
0	0	0	$\cdots$	$M_{n,n-1}$	0	$M_{n,n+1}$
0	0	0	$\cdots$	0	$M_{n+1,n}$	0

(b)

Figure 5.3: Representation of $\boldsymbol{M}$, comparing the full coupling matrix (a), to the reduced coupling matrix (b).

For the case of passive networks, $\boldsymbol{M}$ is a symmetric matrix, meaning $M_{i,j} = M_{j,i}$ for any two given values of i and j. Therefore, the upper triangular values will be the values discussed from here on, with the understanding that they are symmetric.

For mainline coupling, $M_{0,1}$ and $M_{n,n+1}$ represent the external coupling, with $M_{0,1}$

representing the input coupling and $M_{n,n+1}$ the output coupling. $M_{r,r+1}$ for $r = 1, 2, ..., n-1$ represents the internal coupling, or resonator to resonator coupling in a bandpass filter. Conveniently, since this is mainline coupling, $M_{k,k+1}$ can be represented as a function of g-coefficients, becoming

$$M_{k,k+1} = \frac{1}{\sqrt{g_k g_{k+1}}} \qquad \text{for } k = 0, 1, ..., n. \tag{5.11}$$

Given all these relations, every part of $\boldsymbol{A}_{3D}$ can be calculated. The final matrix, represented in Figure 5.4, fully holds all the information about the filter prototype. From this matrix, the magnitude and phase data of the S-parameters can be readily extracted.

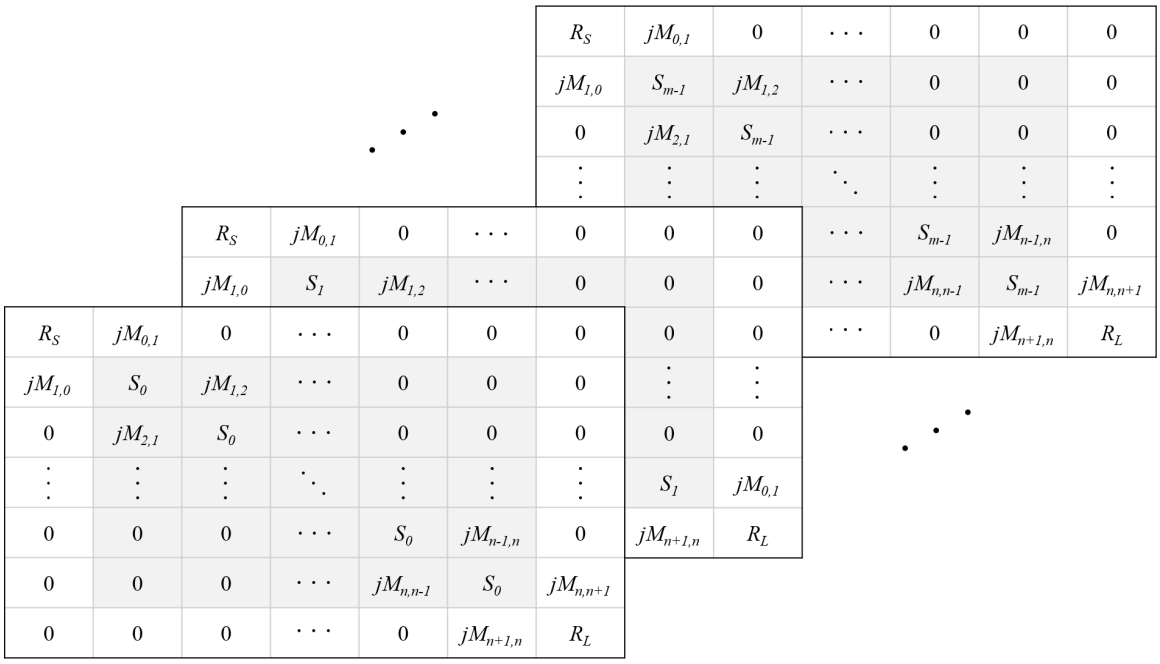

Figure 5.4: Representation of $\boldsymbol{A}_{3D}$, made up of a vector of $\boldsymbol{A}$ matrices, showing how all of the sub-matrices combine to form the whole.

5.1.3 Parameter Extraction

Once the extended coupling matrix is fully generated, getting the S-parameter data is only a matter of matrix inversion. For each discrete frequency point, or equivalently, each $\boldsymbol{A}$ matrix inside of $\boldsymbol{A}_{3D}$, the inverse of the matrix is taken such that $\boldsymbol{B} = \boldsymbol{A}^{-1}$. The S-parameters for a two port network become

$$S_{11} = 1 - 2B_{0,0} \tag{5.12a}$$

$$S_{12} = 2B_{0,n+1} \tag{5.12b}$$

$$S_{21} = 2B_{n+1,0} \tag{5.12c}$$

$$S_{22} = 1 - 2B_{n+1,n+1} \tag{5.12d}$$

Additional helpful values that can be extracted at this step for bandpass filters are the input and output coupling Q's (Q_{ext}) and the coupling coefficients (k), between resonators. Both can be extracted from g-coefficients and FBW. The external input coupling Q is

$$Q_{ext} = \frac{g_0 g_1}{\Delta}, \tag{5.13a}$$

while the output coupling Q is

$$Q_{ext} = \frac{g_n g_{n+1}}{\Delta}. \tag{5.13b}$$

The coupling coefficient is

$$k_{r,r+1} = \frac{\Delta}{\sqrt{g_r g_{r+1}}} \qquad \text{for } r = 1, 2, ..., n-1. \tag{5.14}$$

With these equations, an ideal filter curve can be generated, allowing for comparisons and educated decisions about tuning to be made. However, the g-coefficients of a measured

system are not readily extractable, so methods of getting Q_{ext} and k values from a measured or simulated system are necessary.

Q_{ext} is extractable from the group delay of the reflection coefficient, τ_{S11}. The relation between the two becomes

$$Q_{ext} = \frac{2\pi f_0 \tau_{S_{11}}(f_0)}{4}, \tag{5.15}$$

where $\tau_{S_{11}}(f_0)$ is defined as

$$\tau_{S_{11}}(f_0) = -\frac{\partial \arg(S_{11})}{\partial f}. \tag{5.16}$$

Note that the rest of the filter must be tuned accurately for this relation to hold. Generally, when working with Butterworth filters, the maximum of the group delay function is where the filter is tuned to. Thus, if the group delay maximum is offset in frequency from f_0, the filter is likely mistuned in input coupling, resonator frequency, or even inter-resonator coupling. Using this method of finding Q_{ext} from S_{11}, the input coupling can be tuned to the exact value described by (5.13a).

A way of deriving inter-resonator coupling from simulation is also necessary to quickly design a filtenna. The coupling coefficient, k, can be extracted using a method called the split-pole technique. This method relies on the idea that as two resonators become more coupled, two resonances increasingly interact, generating multiple modes of resonance that diverge. These modes are called the 'even' and 'odd' resonant modes, and the difference between them can be used to determine the coupling coefficient. The resonators can couple electrically, magnetically, or a mixture of both. In addition, they may have different resonant frequencies. In general, [46] gives the relation as

$$k = \pm\frac{1}{2}\left(\frac{f_{02}}{f_{01}} + \frac{f_{01}}{f_{02}}\right)\sqrt{\left(\frac{f_{p2}^2 - f_{p1}^2}{f_{p2}^2 + f_{p1}^2}\right)^2 - \left(\frac{f_{02}^2 - f_{01}^2}{f_{02}^2 + f_{01}^2}\right)^2} \tag{5.17}$$

where f_{01} is the resonant frequency of the first resonator, f_{02} is the resonant frequency of the second resonator, f_{p1} is the frequency of the lower frequency split mode, and f_{p2} is the frequency of the higher frequency split mode. For systems where the resonators are synchronously tuned ($f_{01} = f_{02}$), this general relation simplifies to

$$k = \frac{f_{p2}^2 - f_{p1}^2}{f_{p2}^2 + f_{p1}^2} \tag{5.18}$$

At no coupling, k = 0, and all frequencies align. However, as coupling increases, f_{p1} and f_{p2} get further apart, increasing the value of k. Coupling can increase up until the resonators are directly connected, at which point k reaches 1 and the system becomes a single resonator.

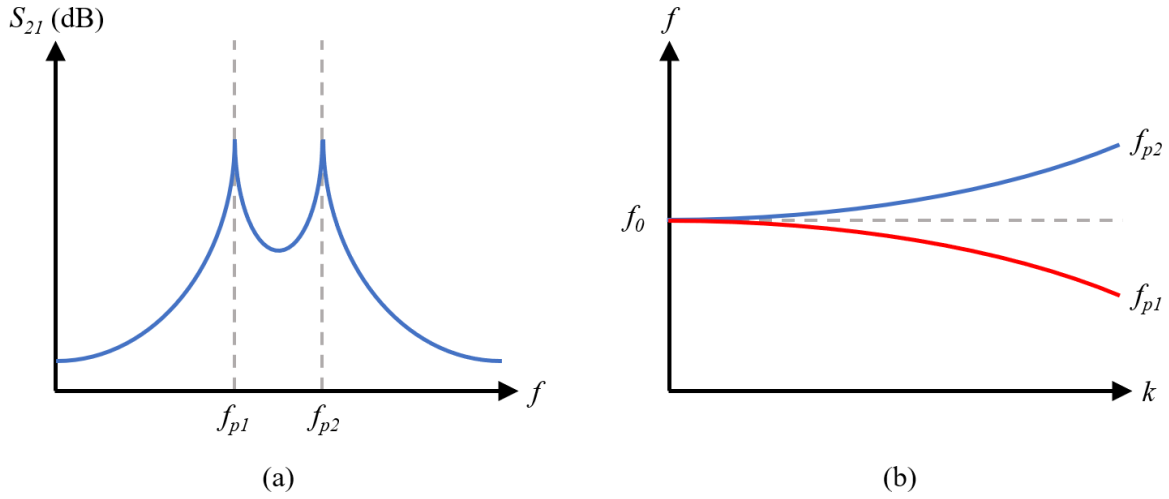

Figure 5.5: Pole splitting as a result of coupling. The effect of a single value of inter-resonator coupling on S_{21} is shown in (a), while the divergence of f_{p1} and f_{p2} as coupling increases is shown in (b).

For a system with weak input coupling, f_{p1} and f_{p2} can be extracted from peaks in S_{21}, shown in Figure 5.5a. However, f_{p1} and f_{p2} can also be extracted from modal analysis using Eigenmode simulations, a typical response shown in Figure 5.5b. Depending on the

coupling mechanism, f_{p1} and f_{p2} may not diverge to symmetrically above and below the starting frequency. They can both diverge to above f_0, below f_0, or any partial mixture of above and below f_0. The way in which the frequencies diverge is dependent on the type of coupling. Assuming a zero size coupling mechanism, pure electric field coupling will cause an increase in f_{p2} while f_{p1} remains constant, while pure magnetic field coupling will cause a decrease in f_{p1} while f_{p2} remains constant. Therefore, to get even splitting, the coupling must be mixed. However, in any realistic system, the coupling mechanism itself affects the structure, often increasing the area and leading to a decrease in resonant frequency. Thus, the coupling of the resonators will likely shift the center frequency of the system, an effect which must be accounted for in the design.

With a method of generating ideal values, methods of extracting parameters from simulation and measurement, and considerations for tuning, it becomes possible to move forward in the filtenna design process. Each part of the filtenna must be characterized.

5.2 Cavity Backed Slot Antenna Design

In Chapter 3, a tunable slot antenna was demonstrated. However, with that antenna there is no simple way to couple into the fields. On top of that, it is typically ideal that an antenna that will be used in an array is cavity backed to enable radiation in only a single direction. Efforts were made to cavity back the antenna, but combined with a tuning mechanism, there was little room for any sort of field overlap to enable antenna-resonator coupling. A new look at the field patterns of the slot antenna and evanescent-mode cavity was taken, with the highlights shown in Figure 5.6.

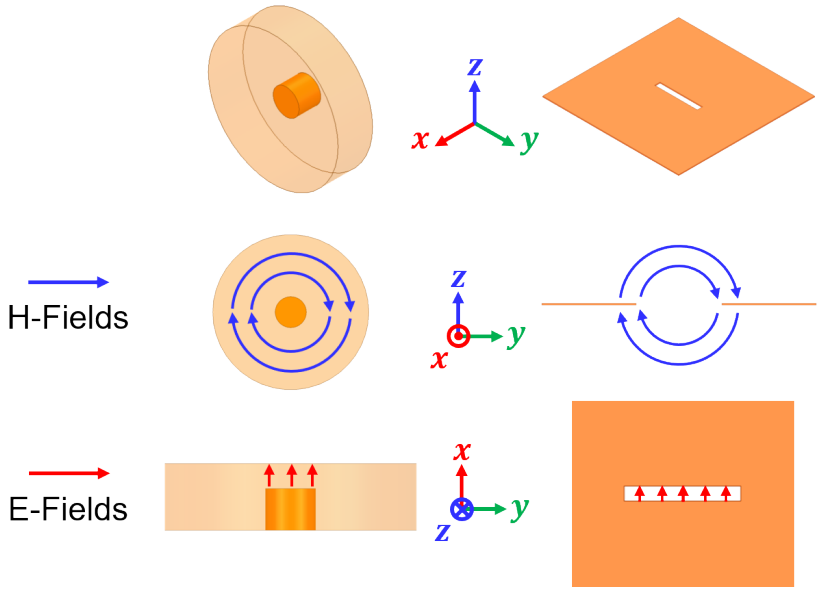

Figure 5.6: Field pattern similarities between an evanescent-mode cavity rotated 90° and a slot antenna

The magnetic and electric field patterns in a slot antenna and a rotated evanescent-mode cavity are very similar. They are so similar, in-fact, that it was theorized a slot could act as an open boundary condition on a bisected tunable evanescent-mode cavity. The bisected cavity would perform double duty as a cavity backing and as a tuning mechanism. The piezo-actuator used in the tunable antenna design could be used to move a copper rod in the cavity, effectively changing the height of the post and therefore changing the gap, allowing tunability. Additionally, coupling between evanescent cavities through irises is well established, so the field coupling problem would also be solved.

With this promising idea in place, a model was created in simulation with a very similar process to evanescent-mode cavity creation. The slot width is set by the substrate of the project, making the slot width and the cavity height both 3.175 mm. Based on this width, a slot length was determined to allow the slot to resonate without loading above the highest frequency, since capacitive loading will only decrease the resonant frequency. Ideally, this

slot length is as large as possible while still allowing tunability, as that guarantees the highest achievable antenna efficiency. A slot length of 30 mm, and thus b of 15 mm, was selected as a good balance of criteria. The fundamental limit of Δg comes from h, not the actuator capability. Since the model of these cavities relies on the assumption that $h >> g$, the total height available for the tuning range was halved, so that the maximum distance is half the cavity height. This still violates the assumption, but it is not as egregious as allowing for h to equal g. Assuming the 15:1 tuning ratio from the tunable antenna is necessary to tune an octave, the 1.5875 mm available for tuning would require a minimum gap size of 113 μm. Plugging these values into (2.11), the necessary post radius, a, to make the cavity resonate at 2 GHz is about 4 mm. Copper rods are commonly available in 3, 4, and 5 mm radius, so the design can be fabricated with tolerance for change on either side.

These design parameters serve as a first approximation, but further testing is necessary due to the violation of many of the assumptions presented in Chapter 2. The fields in the open half of the cavity are not bound, loading the cavity in ways not predicted by the model. The dielectric stack is also not present as modeled; there is only an air gap directly above the post to allow the copper rod to move and the rest of the cavity is filled with dielectric.

To get closer to the exact design dimensions, an Eigenmode model was constructed. This model included the changed air cavity and design dimensions discusses previously. An ideal magnetic conductor (Perfect H) boundary was used on the bisected face to mimic the open circuit boundary condition of the slot antenna. A mesh condition above the post was also included. The Eigenmode model is shown in Figure 5.7. Results from Eigenmode indicated a lowering of the radius of the post would be possible, so the next step down was taken to a 3 mm radius copper rod.

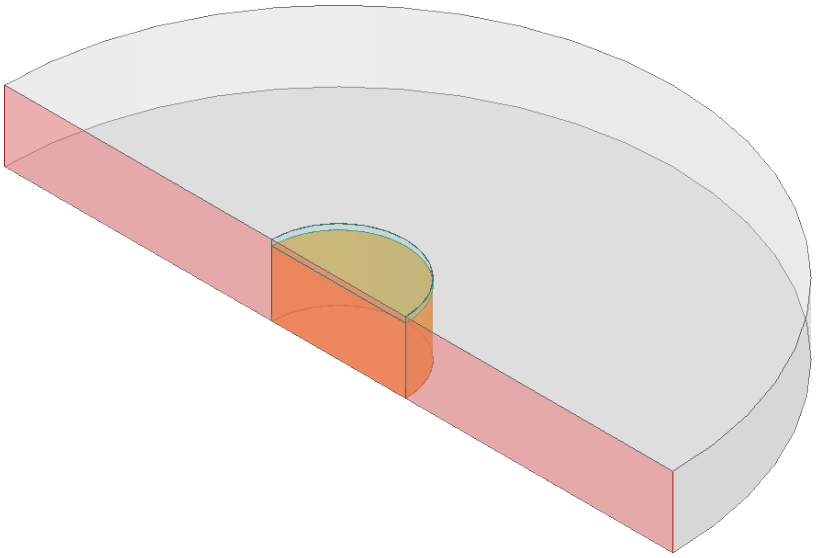

Figure 5.7: Eigenmode model of cavity backed antenna. Grey is TMM3, orange is copper, light blue air, and the red tinted bisected surface represents the Perfect H boundary. The rest of the outside facing surfaces are Finite Conductivity boundaries set to copper to allow for measurement of Q.

The next step was to simulate it as an antenna. Several refinement steps were taken, but eventually, the realistic antenna depicted in Figure 5.8 was created and simulated.

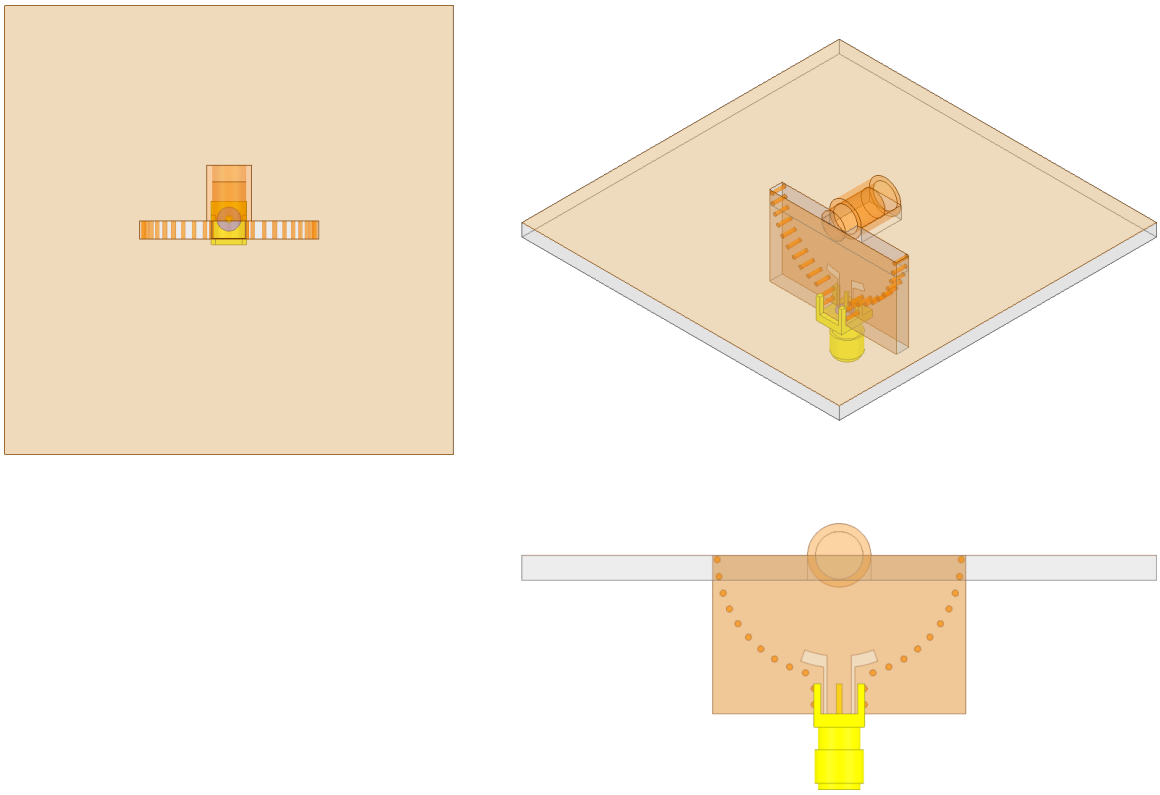

Figure 5.8: Driven Model simulation of cavity backed antenna. Grey is TMM3, orange is copper, and the coax feed is PEC and Teflon.

A CPW line is used to couple into the slot. The specific nature of that coupling will be covered in Section 5.3. The simulated antenna demonstrates ability to tune across all of S-band, with the gap size varying from 120 µm to 1740 µm, a tuning ratio of 14.5:1. This is on par with the tuning ratio expected from the tunable antenna experiments. The antenna also maintains in excess of 10 dB return loss, indicating a good match across all of S-band. The tunability and match can be seen in the S_{11} response shown in Figure 5.9.

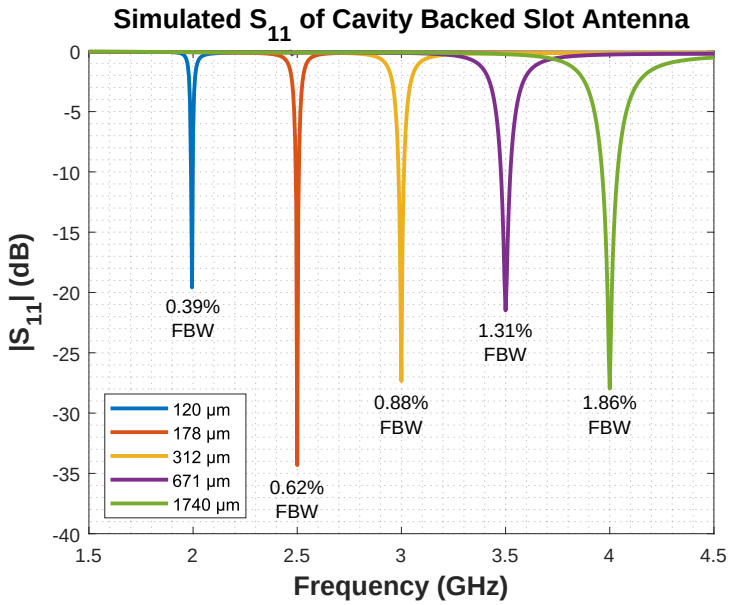

Figure 5.9: Simulated reflection response (S_{11}) of the cavity backed slot antenna. Legend shows the gap distance for each response. 10-dB return loss fractional bandwidth is denoted below each curve.

Cavity backing the slot does cause a significant change in the radiation pattern. The gain in the broadside direction opposite the cavity doubles, while there is significantly less gain in the broadside direction on the side of the cavity. The broadside realized gain opposite the cavity was 3.31 dBi at 2 GHz, 5.85 dBi at 3 GHz, and 6.56 dBi at 4 GHz. The pattern is similar to the pattern of a patch antenna. A sampling of realized gain pattern cuts can be seen in Figure 5.10.

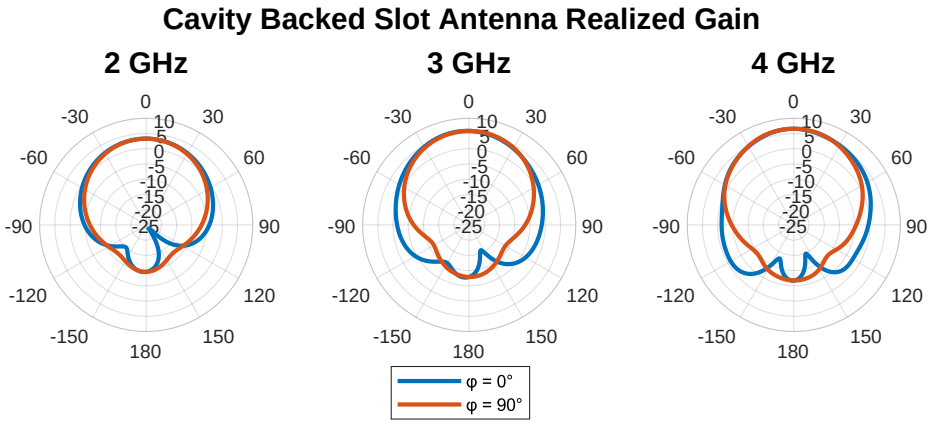

Figure 5.10: Realized gain magnitude patterns at 2, 3, and 4 GHz of a cavity backed slot antenna at two different cut planes

Evanescent-mode cavity backing of the slot seems to have solved all of the problems initially presented, but that is not to say it did so without some sacrifices. Most notably, increasing the width of a slot antenna decreases the polarization purity. In addition to the already thick slot, a large metal piece in the middle with large current flow also likely disrupts polarization purity. A summary of simulated results is seen in Figure 5.11 and a more detailed numerical summary is provided in Table 5.1. At broadside, polarization purity always remains high, but in the $\varphi = 90°$ cut plane, the polarization purity rapidly degrades to less than 20 dB at 30° off broadside. This is likely not good enough for dual-polarized systems, but could be improved with a thinner substrate and therefore a thinner antenna.

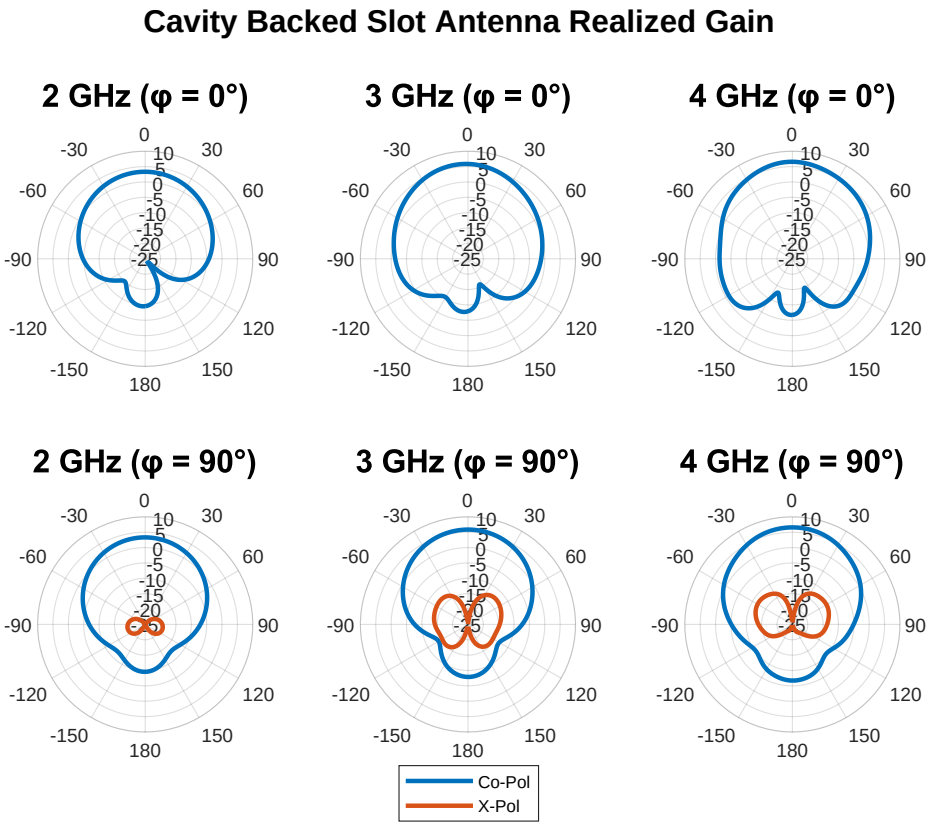

Figure 5.11: Realized gain patterns at 2, 3, and 4 GHz of cavity backed slot antenna. Includes co-polarization and cross-polarization cuts, high polarization purity in the $\varphi = 0°$ cut plane (X-Pol is always below -25 dBi, so it is not visible) but low polarization purity in the $\varphi = 90°$ cut plane.

Table 5.1: Summary of broadside realized gain values for the cavity backed slot antenna, including co and cross polarization.

	2 GHz	3 GHz	4 GHz
Realized Gain Co-Pol ($\theta = 0°$)	3.31 dBi	5.85 dBi	6.56 dBi
Realized Gain X-Pol ($\theta = 0°$)	-60.59 dBi	-48.37 dBi	-42.91 dBi
Realized Gain Co-Pol ($\theta = 180°$)	-9.58 dBi	-7.91 dBi	-6.73 dBi
Realized Gain X-Pol ($\theta = 180°$)	-55.34 dBi	-42.63 dBi	-50.71 dBi

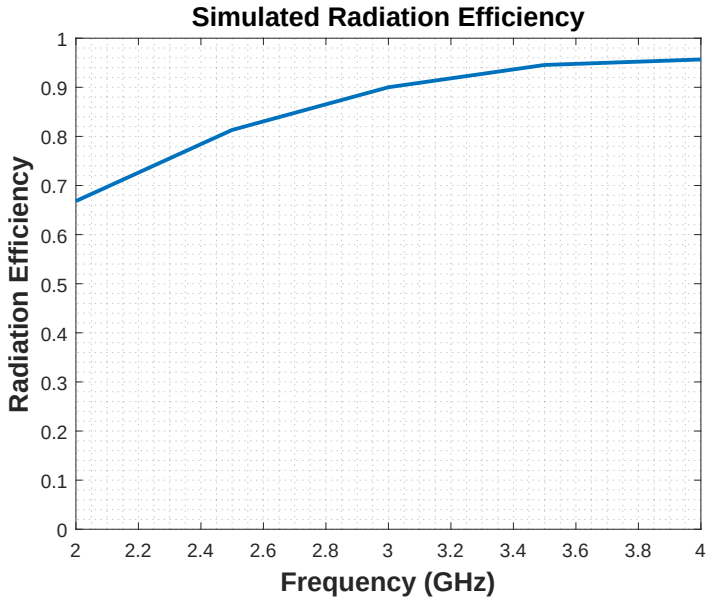

Figure 5.12: Simulated radiation efficiency of the cavity backed slot over the 2-4 GHz tuning range. The antenna demonstrated a minimum of 66.83% radiation efficiency and a maximum of 95.67% radiation efficiency.

Following the analysis of radiation pattern and match, radiation efficiency was investigated as a figure of merit, shown in Figure 5.12. As with the previous antenna, the minimum radiation efficiency occurs at the highest loading, reaching a minimum of 66.83% at 2 GHz.

The radiation efficiency increases as the antenna is tuned across S-band, eventually reaching a maximum of 95.67% radiation efficiency, which is a similar result to the previous tunable antenna.

5.2.1 Power Handling Investigation

As done previously, an investigation into the power handling of the antenna was warranted to determine its feasibility within a high-power setup. A Driven Modal simulation was used to find the maximum electric field strength in the design. The input power was left at the default of 1 W. The fields were extracted from the center of the capacitive gap to limit simulation artifacts that result in unrealistic peaks in electric field at sharp conductor/dielectric boundaries.

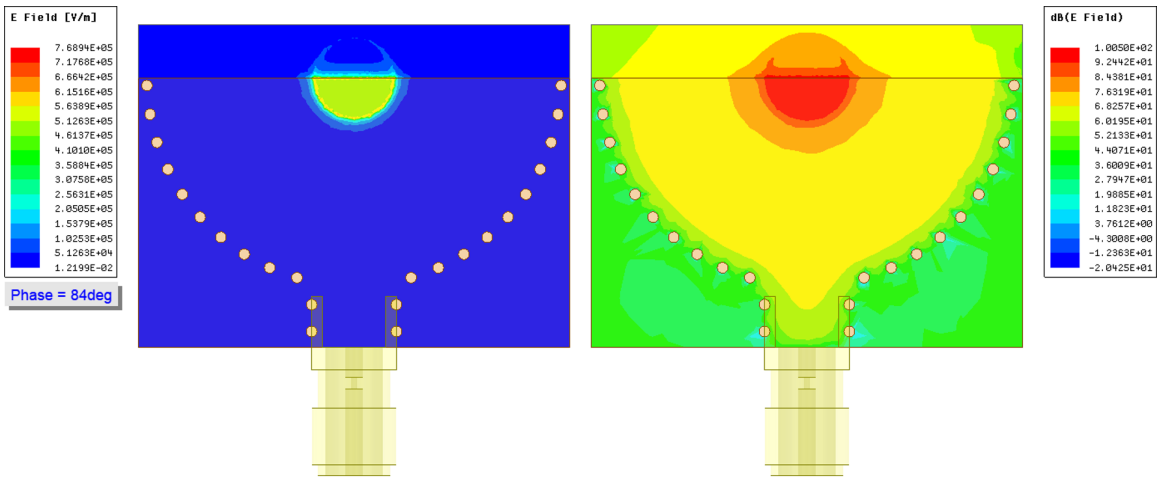

Figure 5.13: Electric field strength and distribution in cavity backed slot antenna tuned to 2 GHz. The electric fields are represented in V/m (a) and in dB of V/m (b), highlighting the large concentration of fields in the gap created by the capacitive post.

The resulting field distribution at 2 GHz can be seen in Figure 5.13. The electric field energy is highly concentrated in the capacitive gap of the antenna, and is correspondingly

the location of highest field strength. Due to the sharp edges of the capacitive post, current crowding occurs on the outer ring, leading to a stronger electric field presence. The maximum electric field in the capacitive gap seen in simulation was 0.7689 V/μm (768.9400 V/mm) at 2 GHz, 0.2874 V/μm (287.3700 V/mm) at 3 GHz, and 0.0286 V/μm (28.5990 V/mm) at 4 GHz. Note that at roughly 3.26 GHz, the gap becomes larger than the CPW line gap. The CPW line gap remains the smallest gap for any frequency higher than 3.26 GHz. However, the electric field magnitude within the CPW gap remains much lower than the electric field strength in the antenna gap for the entire tuning range. This is due to the much higher Q of the antenna and therefore much more energy stored.

As before, (3.1) was used to scale the power up to breakdown. The maximum power handling was predicted to be 105.5527 W (50.2347 dBm) at 2 GHz, 755.7381 W (58.7837 dBm) at 3 GHz, and 76.3049 kW (78.8255 dBm) at 4 GHz. Again, the power handling increases exponentially with frequency, leading to a rapid decrease in power handling for a highly loaded antenna. The breakdown electric field strength was assumed to remain at 7.9 V/μm for all gap sizes [36], but this assumption is likely to cause some error at the higher frequencies. However, due to the large amount of power handling predicted at higher frequencies, failure may come from resistance heating or some other mechanism before gas discharge could come into effect, limiting the impact of this error. Regardless, the antenna should be able to handle at least a kilowatt at higher frequencies without suffering from gas discharge effects, and a kilowatt is a significant amount of power to fit in such a small area.

With the polarization purity problem noted and promising power handling predictions, the decision was made to move forward with the rest of the filtenna design, incorporating the lessons learned from the simulation of this cavity backed tunable antenna. With this design, any order of filter would technically be possible. To limit the complexity for this proof of concept, a 2nd order filtenna was decided upon.

5.3 External Coupling Design

When feeding any filter structure, the coupling of the feed to the resonators needs to be tunable in a predictable manner. The Q_{ext} of the external coupling needs to match the ideal filter structure. However, how Q_{ext} is tuned depends highly on the feeding structure used. Characterization of the feeding structure must be done to understand how to adjust the geometry to change Q_{ext} and how those changes impact the rest of the filter structure.

There are many ways one can go about feeding an evanescent-mode cavity, but one of the easier methods is using a flared-wing, shorted CPW line. It is single layer and easily adjusted to increase or decrease external coupling. However, cutting groves into a cavity to form the CPW lines does have an effect on its resonant frequency and quality factor. There has been some work on how different design changes impact the coupling and performance of the resonator [48], but further investigation for this particular resonator was deemed necessary due to the different geometry of the cavity. That is what this section will attempt to address.

For a flared-wing, shorted CPW line in this work, there are three parameters that are used to describe the entire structure: the radius to the center of the wings ($feed_R$), the angle the wings sweep out of the cavity before the short ($feed_{angle}$), and the width of the cutout ($feed_w$). To see how these parameters affected the resonant frequency and Q of the cavities they coupled into, several Eigenmode simulations were run. The cutouts for the CPW lines were represented by Perfect H boundaries to ensure the proper boundary condition.

5.3.1 CPW Feed Radius

The feed radius is measured to the center of the feed lines, as demonstrated in Figure 5.14. The feed radius was varied from 3 to 6 mm.

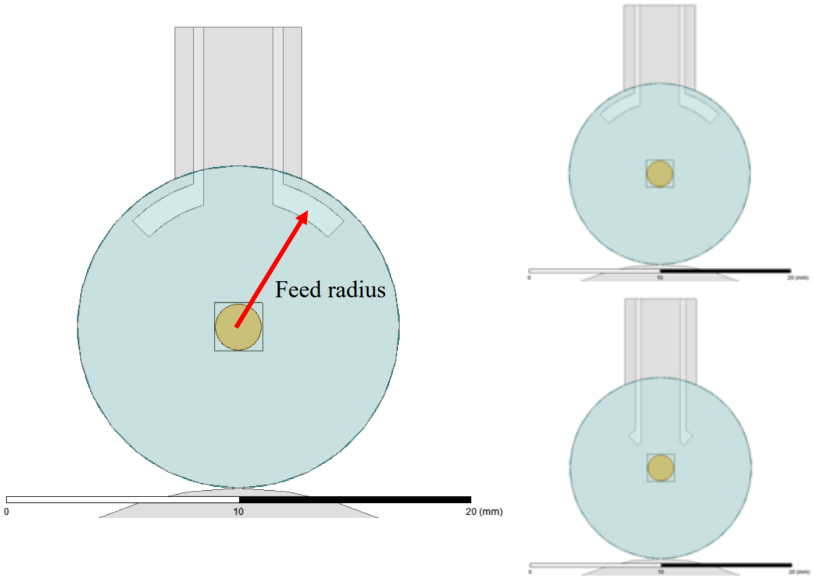

Figure 5.14: Geometric representation of $feed_R$ (left), with the two extremes of $feed_R$ also shown (right).

Feed radius changes have very small effects on the resonant mode or Q of the cavity. The mode changed from 2.9787 GHz at a feed radius of 3 mm to 2.9811 GHz at a feed radius of 6 mm (0.08% increase). The Q changed from 765 at 3 mm to 787 at 6 mm (2.8% increase). The resonant mode increase is within simulation noise bounds, while there appears to be a very slight gain in Q from increasing the feed radius. For this reason, picking a feed radius to make the wings close to the outer edge seems desirable. Also, changing the feed radius would not be a good option for tuning, as it seems to have little effect, shown in Figure 5.15. As this would be the most difficult parameter to change post fabrication, the lack of effect is a helpful finding.

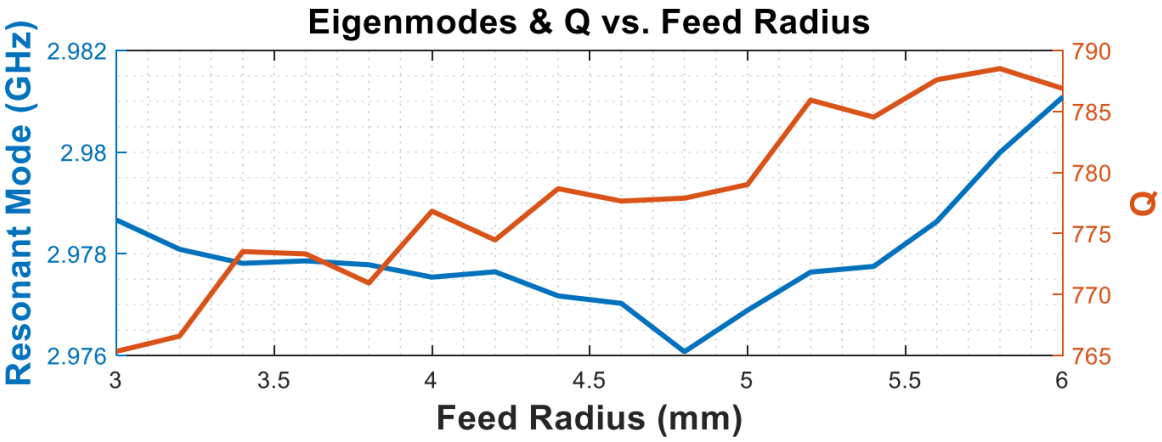

Figure 5.15: Eigenmode resonant frequency and Q as a function of changing $feed_R$.

5.3.2 CPW Feed Angle

The feed angle is the angle the feed wings cover measured from the center of cavity, or the angle from 'wingtip to wingtip.' This is demonstrated in Figure 5.16. The feed angle was swept from 40 degrees to 180 degrees.

Feed angle by far had the largest combined effect on the resonant mode and Q of the cavity, notably in a non-linear fashion. The total response for both resonant mode and Q can be seen in Figure 5.17. In summary, the resonant mode decreased from 3.0300 GHz at 40 degrees to 2.7407 GHz at 180 degrees (9.5% decrease) and the Q decreased from 831 at 40 degrees to 646 at 180 degrees (22.3% decrease). Feed angle changes can get close as far as tuning the resonant frequency and Q, but it is *not* a good tool if you want to tune both independently. It is therefore recommended to set the feed angle early in the design process so the cavity operates as expected, and then only tune it again if absolutely necessary, as it will require starting over if changed.

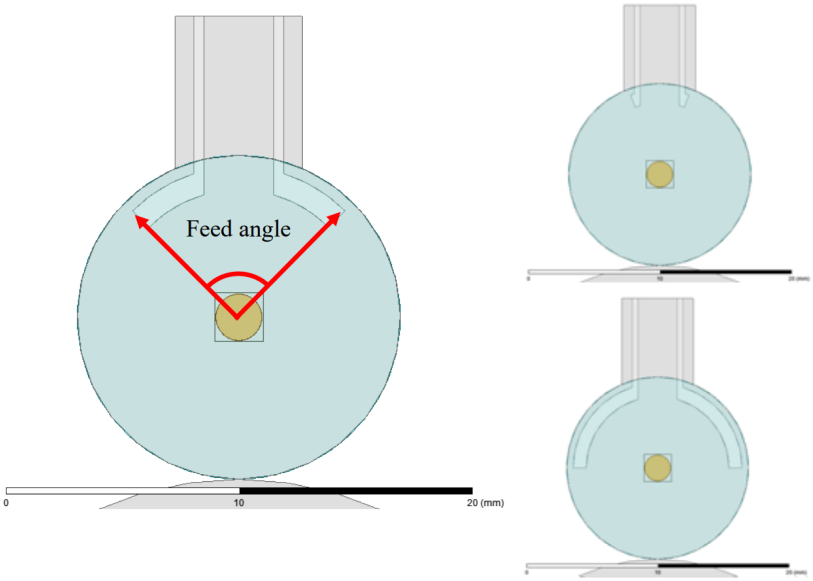

Figure 5.16: Geometric representation of $feed_{angle}$ (left), with the two extremes of $feed_{angle}$ also shown (right).

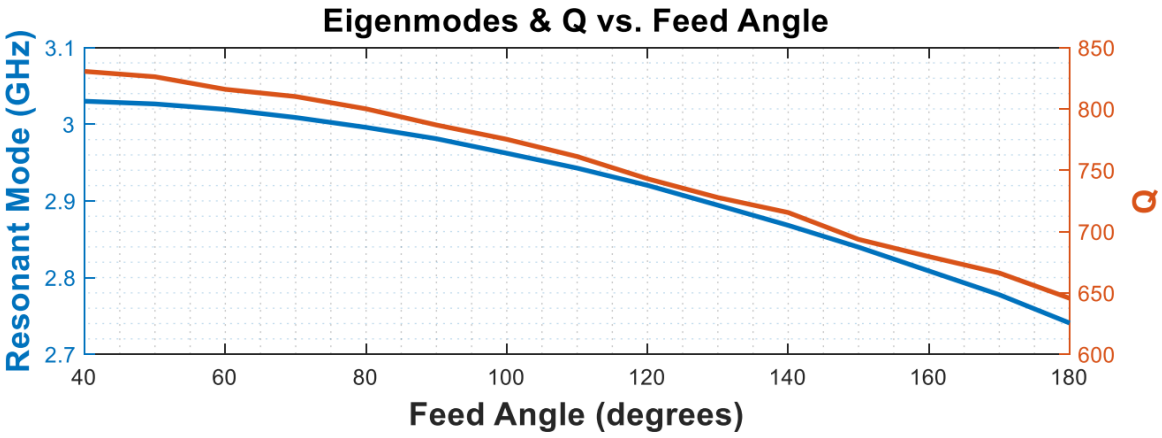

Figure 5.17: Eigenmode resonant frequency and Q as a function of changing $feed_{angle}$.

5.3.3 CPW Feed Radius

The feed width is the width of the gaps in the CPW line in the wings, shown in Figure 5.18. Feed width was varied from 0.5 mm to 1.5 mm in this test.

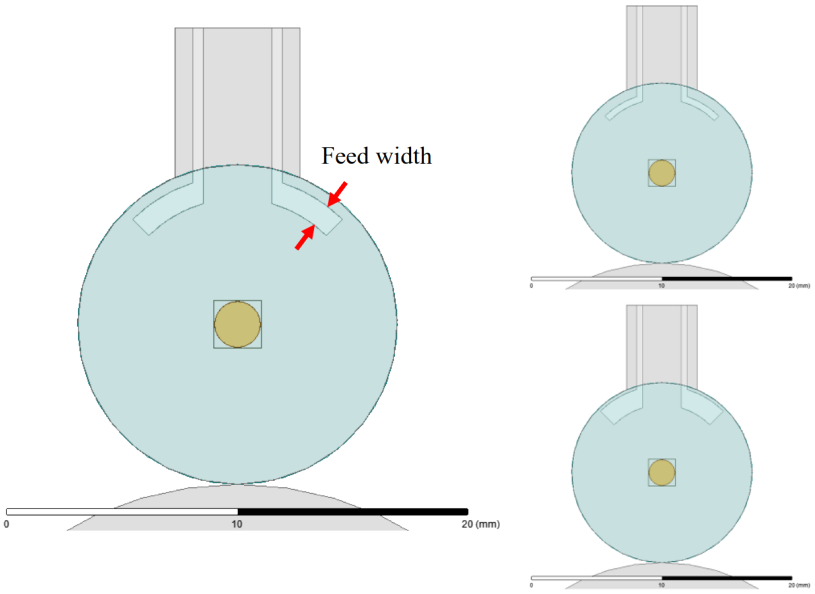

Figure 5.18: Geometric representation of $feed_w$ (left), with the two extremes of $feed_w$ also shown (right).

Feed width changes had very small effects on the resonant mode or Q of the cavity. The resonant mode change appears linear, decreasing from 2.9913 GHz at 0.5 mm to 2.9743 GHz at 1.5 mm (0.57% decrease). The Q showed slight random variation, likely due to simulation artifacts, but it remained mostly constant. The trends of both resonant mode and Q are shown in Figure 5.19. When trying to tune external coupling, varying feed width is a great option for minimally affecting the parameters of the cavity. Feed width variations should be used for fine tuning once the feed angle is set, allowing for dialing in of precise input coupling.

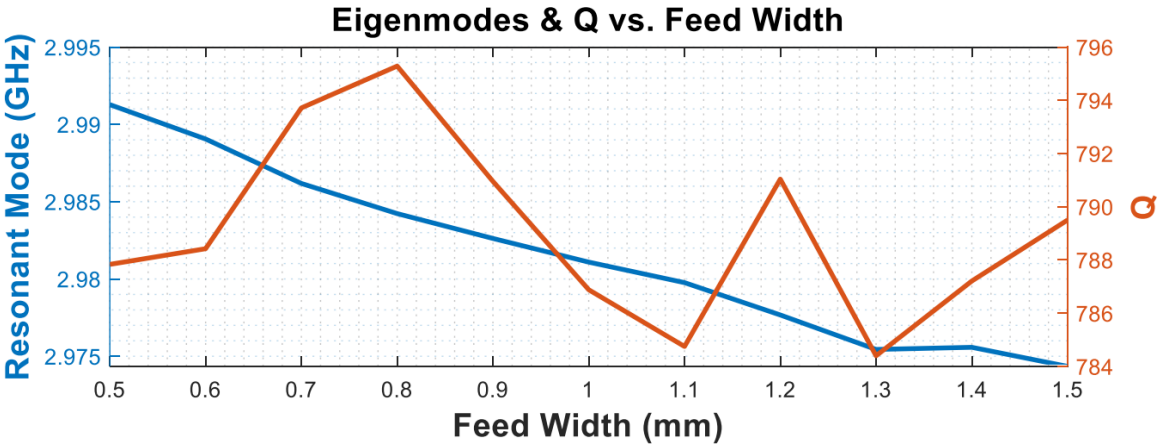

Figure 5.19: Eigenmode resonant frequency and Q as a function of changing $feed_w$.

5.3.4 HFSS Modeling

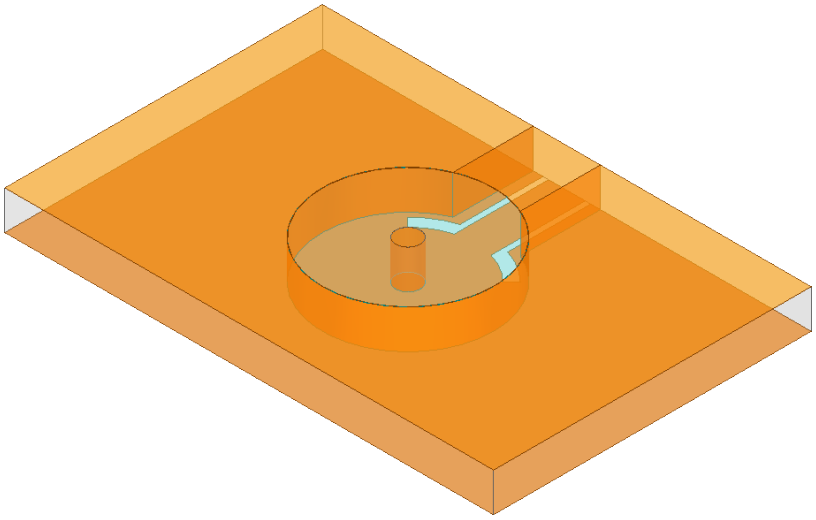

Figure 5.20: HFSS Driven Modal simulation to extract Q_{ext} of CPW fed evanescent-mode cavity.

With all of this information as how to properly tune the input coupling of a CPW fed evanescent-mode cavity, the tuning can be performed on a reduced complexity system of a single resonator and feed. An example reduced complexity system is shown in Figure 5.20.

A Driven Modal simulation in HFSS can be readily used to extract the complex S-parameter data needed to derive the group delay and Q_{ext}.

5.3.5 External Coupling to Free Space

For a filtenna, the second external coupling is from the antenna aperture to free space. Antenna researchers typically only refer to total antenna Q, analogous to Q_L in filter theory [37]. Since the Q of antennas does not typically include the two Q_{ext} values and a Q_u value, there is little developed theory on Q_{ext} of antennas, and therefore little theory on coupling to free space. It is not currently known how to tune this value without significantly affecting the rest of the filtenna design. It is likely that the physical size of the antenna aperture has a large effect on external coupling, and is undoubtedly frequency dependent, but it is not known at this time what form that relation takes.

For this filtenna design, the filtenna was tuned to an estimated fractional bandwidth. After fully tuning, the true Q_{ext} was extracted from the TD transform by creating an ideal LC ladder model with an admittance inverter at the output port. The value of the admittance inverter was altered until the response lined up with that seen in the simulated TD transform. The required FBW to create that derived Q_{ext} was then used as the design FBW of the filtenna and the system was retuned.

5.4 Internal Coupling Design

In addition to input coupling, the inter-resonator coupling needs to be tuned to specification. The coupling coefficient, k, can be extracted from the ideal response using (5.14). The coupling coefficient can be extracted from a simulated response by (5.18). For this filtenna design, coupling is accomplished through iris coupling between cavities. Increasing the size of the iris corresponds to a larger overlap of the fields, increasing the coupling between

the resonators. To the best of the author's knowledge, there is no closed-form expression for deriving the coupling coefficient based solely on the geometry of two evanescent-mode cavities of differing size. In [46], Hong gives a general form for calculating k based on the fields as

$$k = \frac{\iiint \varepsilon \underline{E}_1 \cdot \underline{E}_2 dv}{\sqrt{\iiint \varepsilon |\underline{E}_1|^2 dv \times \iiint \varepsilon |\underline{E}_2|^2 dv}} + \frac{\iiint \mu \underline{H}_1 \cdot \underline{H}_2 dv}{\sqrt{\iiint \mu |\underline{H}_1|^2 dv \times \iiint \mu |\underline{H}_2|^2 dv}} \tag{5.19}$$

where $\underline{E}$ and $\underline{H}$ represent the electric and magnetic fields of each resonator, respectively.

Since both resonators in the filtenna act like evanescent-mode cavity resonators, the coupling between cavities is primarily magnetic coupling, and so the equation can be reduced to a decent approximation by only including the magnetic fields. However, this still leaves the equation in a fairly complicated state. Instead of further trying to alter the math, it is faster to create a simplified model in an Eigenmode simulation, shown in Figure 5.21. Eigenmode simulations with simple geometry are fairly rapid simulations to run.

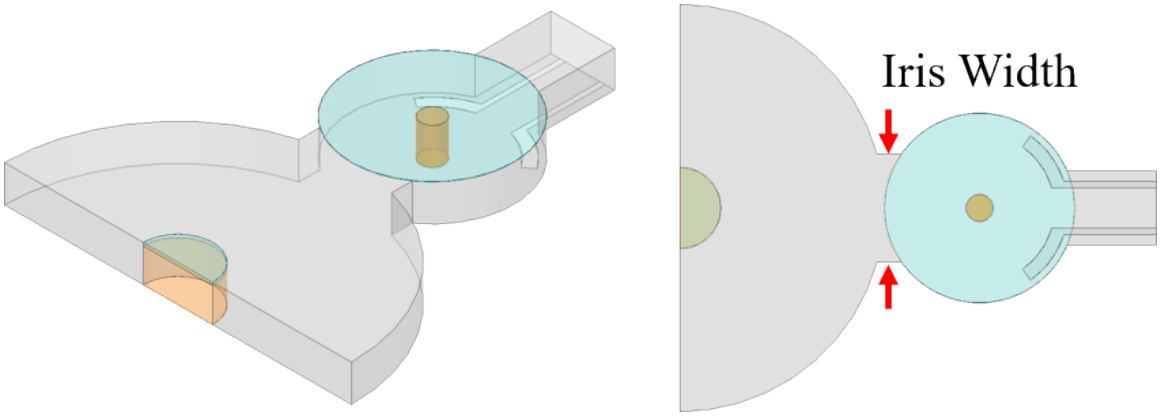

Figure 5.21: HFSS Eigenmode model used to extract inter-resonator coupling as a function of iris width.

Notice in Figure 5.21, the Eigenmode model includes the feed. Since introducing the feed has a significant impact on the resonant frequency of the cavity, it was included to

get accurate coupling information. Thus, it is recommended that a first attempt at external coupling tuning is attempted before pursuing inter-resonator coupling. All of these systems affect each other, so some back and forth will still be necessary. The cut face of the antenna cavity and the CPW line gaps are also set as Perfect H boundaries to ensure proper boundary conditions. Mesh operations are also in place above the posts.

After creation of an Eigenmode model, the iris width can be swept, causing a corresponding change in coupling between the antenna and cavity. This can be seen in the first two Eigenmodes, which diverge as the iris width increases, representing a splitting of f_{p1} and f_{p2}. For resonators tuned to 3 GHz, the resulting change is shown in Figure 5.22.

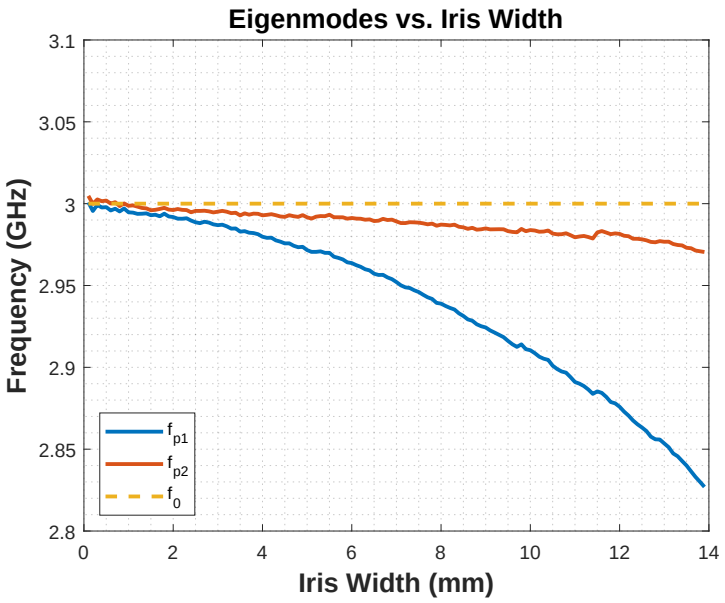

Figure 5.22: Eigenmode simulation showing a divergence of modes as the iris width increases and coupling correspondingly increases. The filtenna was tuned to 3 GHz.

For this particular coupling structure, the inter-resonator coupling resulted in an overall decrease in the center frequency of the system. The almost purely magnetic coupling is responsible for most of the decrease in f_{p1}, while the slight decrease in f_{p2} is predominately due to the total area of the resonators increasing as the iris widens. An iris width of 10 mm

would create a k_{12} value close to ideal, but the center frequency needed to be shifted back up to 3 GHz.

The new center frequency of the structure can be found using the geometric mean of the split mode frequencies, or

$$f_0 = \sqrt{f_{p1} f_{p2}}. \tag{5.20}$$

Using this relation, it was found that the new f_0 at an iris width of 10 mm was 2.9504 GHz, or a 1.6539% decrease from 3 GHz.

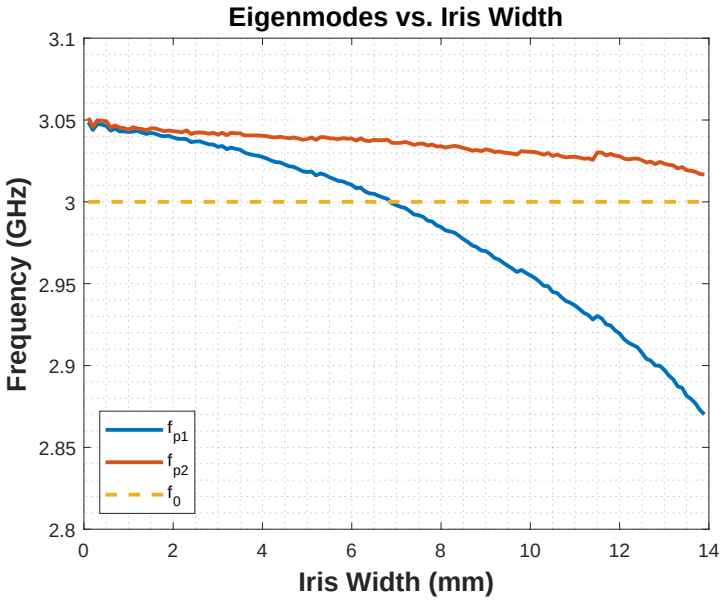

Figure 5.23: Eigenmode simulation showing a divergence of modes as the iris width increases and coupling correspondingly increases, but with compensation for decreased center frequency due to coupling. The filtenna was tuned to 3 GHz.

To compensate for the change, the resonators were tuned to 3.0505 GHz, a 1.6539% increase from 3 GHz, when there is no coupling. The resonators can be tuned to this value quickly by working backwards with (2.11) or by curve fitting Eigenmode versus gap size curves. Either way, once the resonators were adjusted, the new splitting of modes compared

to iris width was generated, as seen in Figure 5.23. In the adjusted case, the ideal coupling still happens when the iris width is at 10 mm, but now the center frequency, found using (5.20), aligns with the desired center frequency of the filtenna of 3 GHz.

5.5 Simulated Filtenna

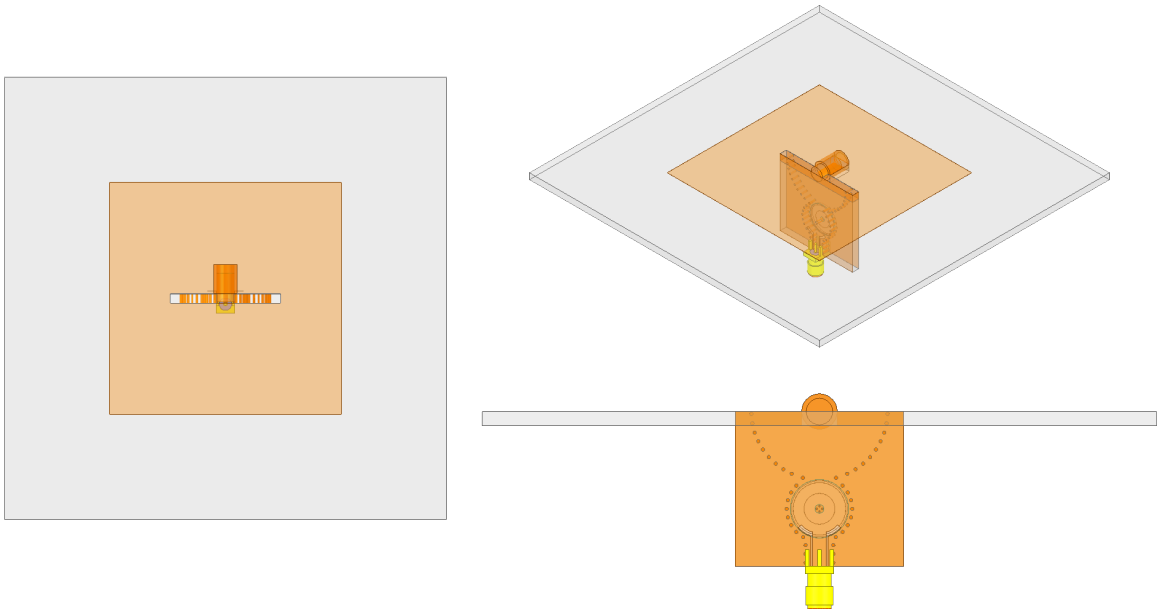

Figure 5.24: HFSS model of filtenna, with vias, actuating metal, and other features to add realism.

With a way to quickly and effectively get close to ideal values for external coupling, internal coupling, and resonator frequency, all that remains is to design a full filtenna. This can be done by applying the design dimensions from simplified simulations to a full filtenna structure, then further tuning the design using the TD method. This can itself be done in several steps of complexity, but the full model with vias, coaxial feed, and copper thickness (assumed to be half-ounce, or 18 µm) is presented here. The model created in HFSS is seen in Figure 5.24 and a zoomed in look with final design dimensions is seen in Figure 5.25.

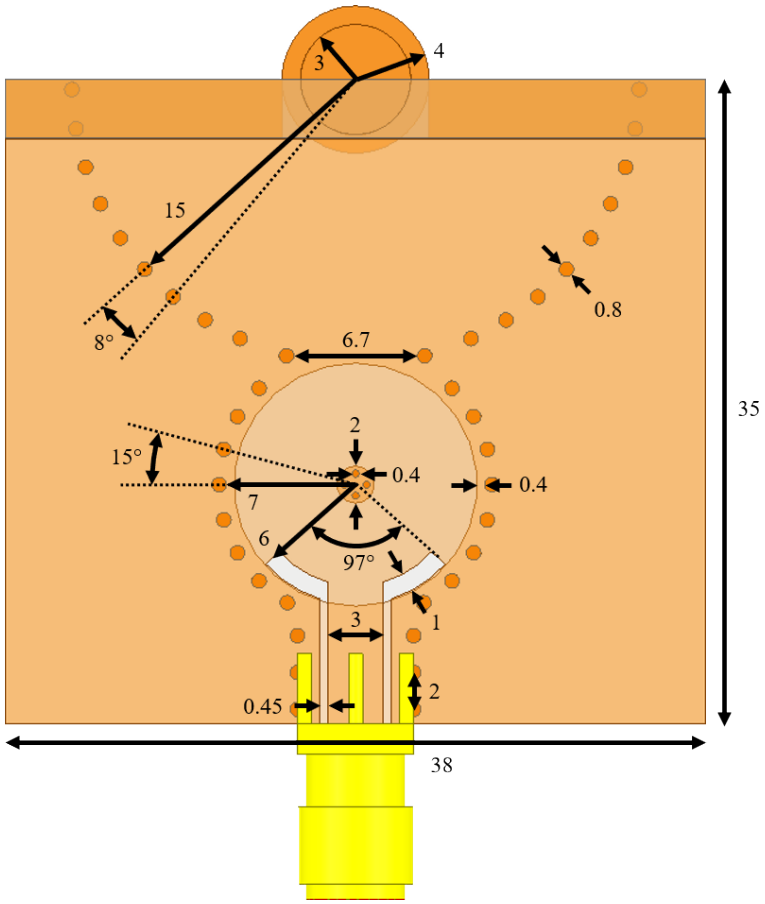

Figure 5.25: HFSS model of filtenna with measurements. All values are in millimeters unless otherwise notated.

5.5.1 Tuning a 3 GHz Filtenna

Following the creation of a realistic model in HFSS, TD tuning was performed. An ideal response for a 2nd order Butterworth filter (f_0 = 3 GHz, FBW = 2%) with a cavity Q_u of 630 was generated. A Q_u of 630 was the average value observed in Eigenmode simulations. It took nine steps to fully tune the filtenna. A step by step process is shown in Figure 5.26. Filtenna 00 represents the filtenna without any tuning, directly taking the model with design dimensions informed from Eigenmode and simpler Driven Modal models. Seeing that

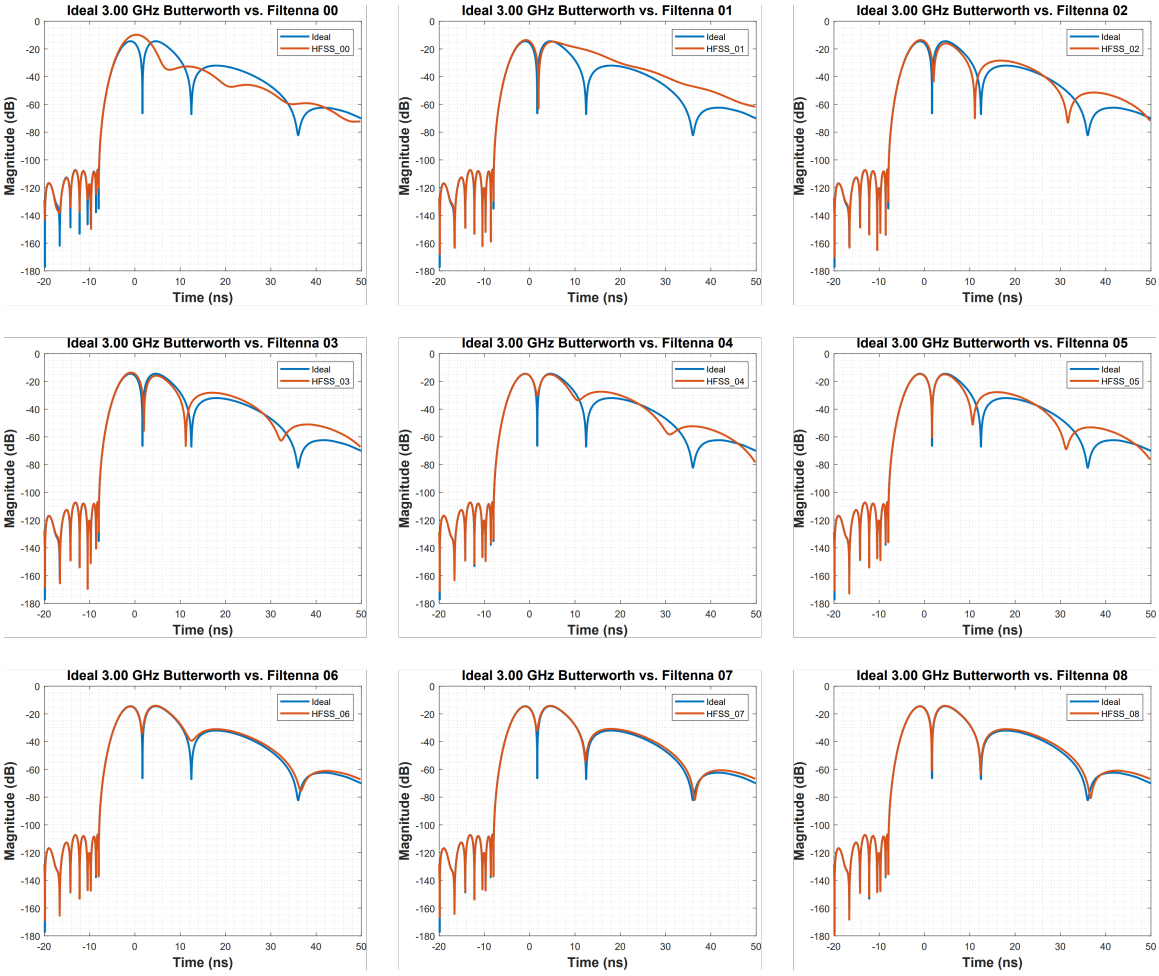

Figure 5.26: Time domain tuning of HFSS filtenna. In each step one physical value was adjusted to bring the filtenna closer to ideal. See Table 5.2 for details on which dimensions were adjusted for each step.

Table 5.2: Summary of tuning dimensions for a 3 GHz filtenna. The changed value between iterations is denoted by an asterisk.

Filtenna	Antenna Gap	Cavity Gap	Iris Width	Feed Angle
00	248 µm	18.18 µm	7.4 mm	90°
01	248 µm	*20.20 µm	7.4 mm	90°
02	*275 µm	20.20 µm	7.4 mm	90°
03	275 µm	*20.25 µm	7.4 mm	90°
04	275 µm	20.25 µm	7.4 mm	*97°
05	275 µm	*20.40 µm	7.4 mm	97°
06	275 µm	20.40 µm	*6.7 mm	97°
07	*272 µm	20.40 µm	6.7 mm	97°
08	272 µm	*20.30 µm	6.7 mm	97°

the first resonator, or the evanescent-mode cavity, was mistuned, the gap was decreased to lower the resonant frequency, which became Filtenna 01. Next, the second resonator, the antenna, was also seen to be badly mistuned, so the antenna gap size was increased to increase the resonant frequency, becoming Filtenna 02. The tuning of the second resonator affected the first resonator. To correct for this, the gap of the first resonator was increased slightly, becoming Filtenna 03. With both resonators fairly well tuned, input coupling was seen to be too low, since the hump is higher than ideal and the first zero is later in time than ideal. This was adjusted in Filtenna 04 by increasing the feed angle, thereby increasing coupling. The increased coupling loaded the first resonator, requiring an increase in frequency to compensate. In Filtenna 05, the first resonator gap was again increased slightly. Due to the second hump being lower than ideal and the second zero being earlier in time than ideal, the inter-resonator coupling was determined to be too high. This was corrected in Filtenna 06, where the iris width was decreased. Decreasing the iris size increased the resonant frequency of both resonators. The second resonator was fixed first in Filtenna 07, where the gap size was lowered. Lastly, in Filtenna 08, the gap size of the first resonator was also lowered slightly to bring it in line. A summary of the adjusted parameters can be seen in Table 5.2.

Following the tuning of the filtenna using S_{11}, the broadside realized gain of the filtenna versus frequency was simulated. This represents a close analog to S_{21} for a filtenna, and would give insight into if the filtenna was truly acting like a second order Butterworth filter. Since the S_{21} of an ideal filter peaks at 0 dB, the maximum ideal S_{21} generated was shifted so it matched the maximum realized gain. The broadband result is seen in Figure 5.27, while a zoomed in version on the passband is seen in Figure 5.28.

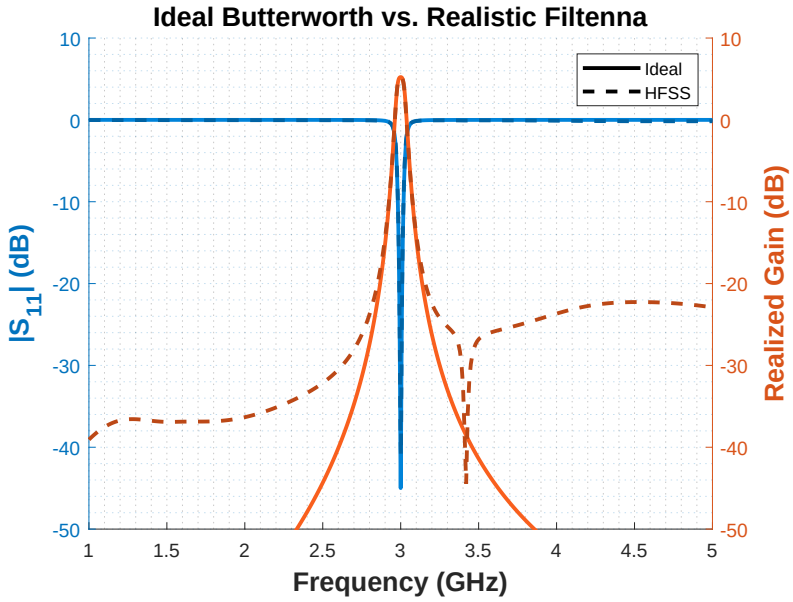

Figure 5.27: S_{11} response of filtenna with broadside realized gain over frequency compared to an ideal filter with finite Q.

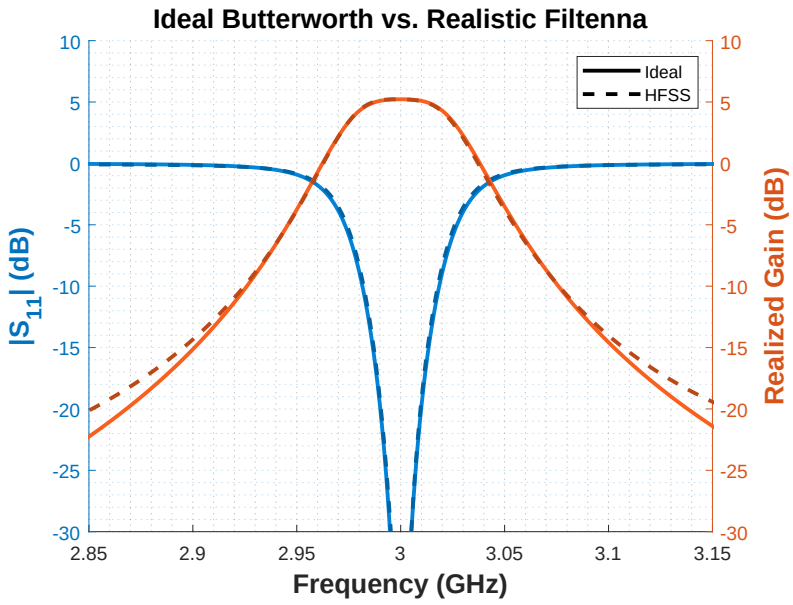

Figure 5.28: S_{11} response of filtenna with broadside realized gain over frequency compared to an ideal filter with finite Q, zoomed in on the pass-band.

As seen in Figure 5.28, the radiated frequency response of the filtenna matches up extraordinarily well with the ideal response of a 2nd order Butterworth filter in the passband. From the realized gain curve, the response has a 1.98% 3-dB fractional bandwidth, very close the the ideal 2.00%. Additionally, the center frequency was calculated from the 3-dB frequencies to be 3.00 GHz, exactly as designed. To be clear, this radiated frequency response was accomplished without ever looking at the radiated response; it came purely from S_{11}. This lends strong evidence to the fact that the filtenna is operating as a higher-order device, and that filter theory can be readily applied to filtenna modeling. Additionally, the close alignment indicates the power of the TD method to accurately tune filtennas.

5.5.2 Tuning across S-band

Following the success of creating a filtenna at 3 GHz, the design was modified to demonstrate that it could tune fully across S-band. However, only the resonant frequency of each resonator is tunable with this design, so the filtenna will fundamentally perform worse than at 3 GHz. There exists technology to tune the input and inter-resonator coupling of evanescent-mode cavities [4], which would allow for drastically increased performance at the edges of the band, but that application is outside the scope of this research and will be left to future work.

With these limitations in mind, the resonators were set to just above 2 GHz and 4 GHz based off of curve fitted data from Eigenmode simulations. They were set just above to compensate for the decrease in frequency resulting from the loading of inter-resonator coupling. Since external coupling and inter-resonator coupling are not tunable in this design, they were left at the design dimensions for 3 GHz. As a result, at frequencies lower than 3 GHz, the electrical size of the coupling apertures decreases, which should lead to under-coupling. At frequencies higher than 3 GHz, the electrical size of the coupling apertures increases, which should lead to over-coupling. Following initial setup, the designs were optimized to tune the resonators as close to ideal as possible by maximizing the depth of both of the zeros in the TD response. The TD results of efforts to tune to 2 GHz and 4 GHz are shown in Figure 5.29.

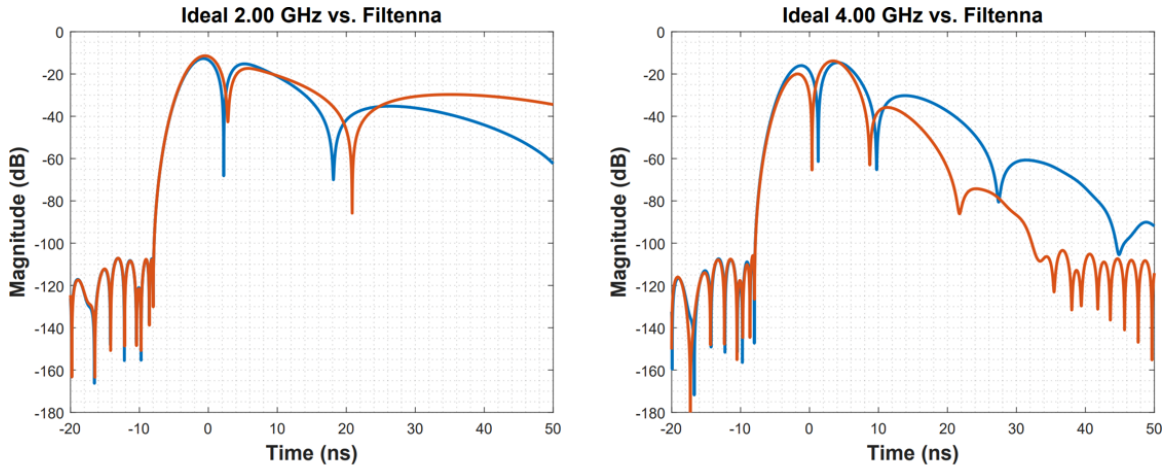

(a) (b)

Figure 5.29: Time domain response of filtenna with resonators tuned to 2 GHz (a) and 4 GHz (b), but with coupling dimensions designed for 3 GHz

In Figure 5.29a, the first and second hump are higher than ideal and the zeros are further in time than ideal, indicating under-coupling, as expected. In Figure 5.29b, the first and second hump are lower than ideal and the zeros are earlier in time than ideal, indicating over-coupling, also as expected. With the filtenna tuned to these frequencies, the resulting broadband realized gain and S_{11} plots were generated, seen in Figure 5.30. Zoomed in versions on the passband of each are shown in Figure 5.31.

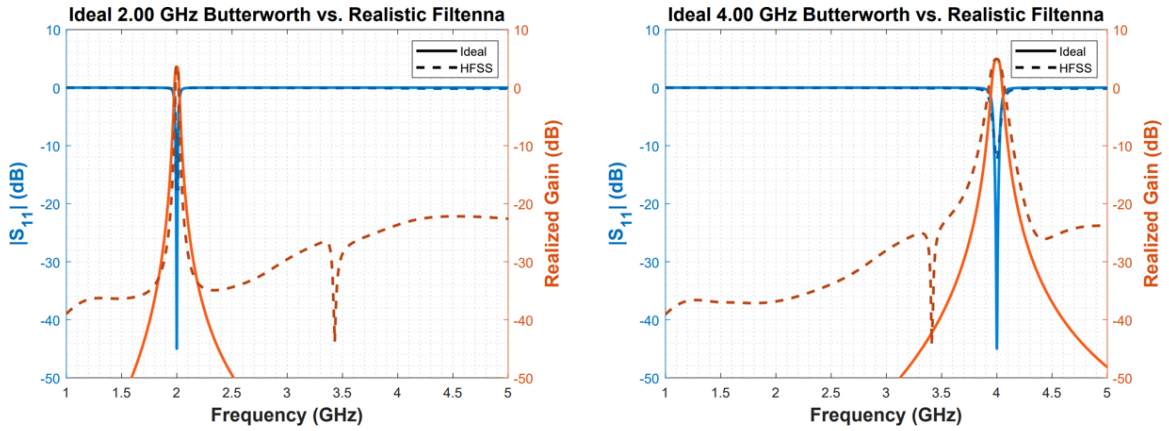

(a) (b)

Figure 5.30: 2 GHz (a) and 4 GHz (b) S_{11} response of filtenna with broadside realized gain over frequency compared to an ideal filter with finite Q.

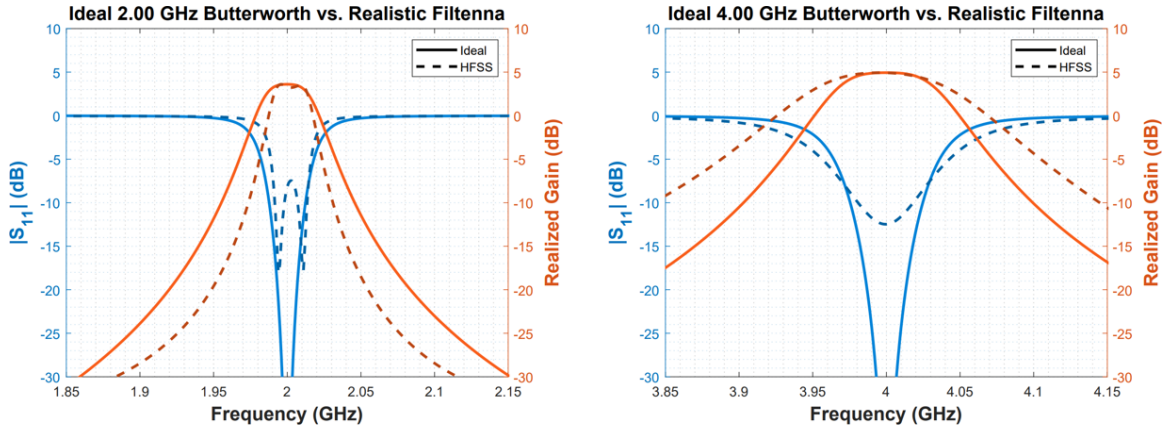

(a) (b)

Figure 5.31: 2 GHz (a) and 4 GHz (b) S_{11} response of filtenna with broadside realized gain over frequency compared to an ideal filter with finite Q, zoomed in on the pass-band.

Again, since the coupling was not adjusted, the responses of each differ from expected. The 2 GHz response is more narrowband in realized gain than ideal due to under-coupling, resulting in a 1.43% 3-dB fractional bandwidth. The 4 GHz response is more broadband in realized gain than ideal due to over-coupling, resulting in a 2.82% 3-dB fractional band-

width. Both responses also suffer in match across the passband due to the coupling errors, and this is reflected as a different than ideal S_{11}. However, the calculated center frequencies from the 3-dB points were 2.00 GHz and 4.00 GHz, exactly at the designed center frequencies. Both responses also display frequency characteristics indicative of a 2nd order filter (flat passband with steeper rejection out of band than possible with single resonator), indicating that both are still functioning as filtennas.

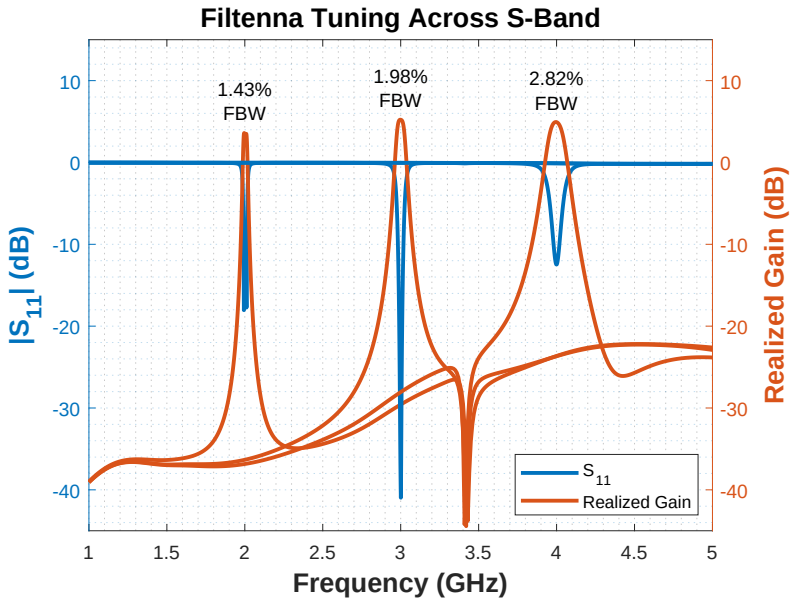

Figure 5.32: Filtenna S_{11} and realized gain tuned to 2, 3, and 4 GHz, demonstrating tunability across all of S-band. The 3-dB fractional bandwidths of each response are noted above the peaks.

The radiation pattern of the filtenna is also of interest. The filtenna maintains similar radiation patterns and levels of polarization purity to the cavity backed slot antenna. A summary of simulated results is seen in Figure 5.33 and a more detailed numerical summary is provided in Table 5.3. At broadside, polarization purity always remains high, but in the φ = 90° cut plane, the polarization purity rapidly degrades to less than 20 dB at 30° off broadside. This is not good enough for dual-polarized systems, which often need in excess

of 40 dB of polarization purity [49], but could be improved with a thinner substrate and therefore a thinner slot antenna.

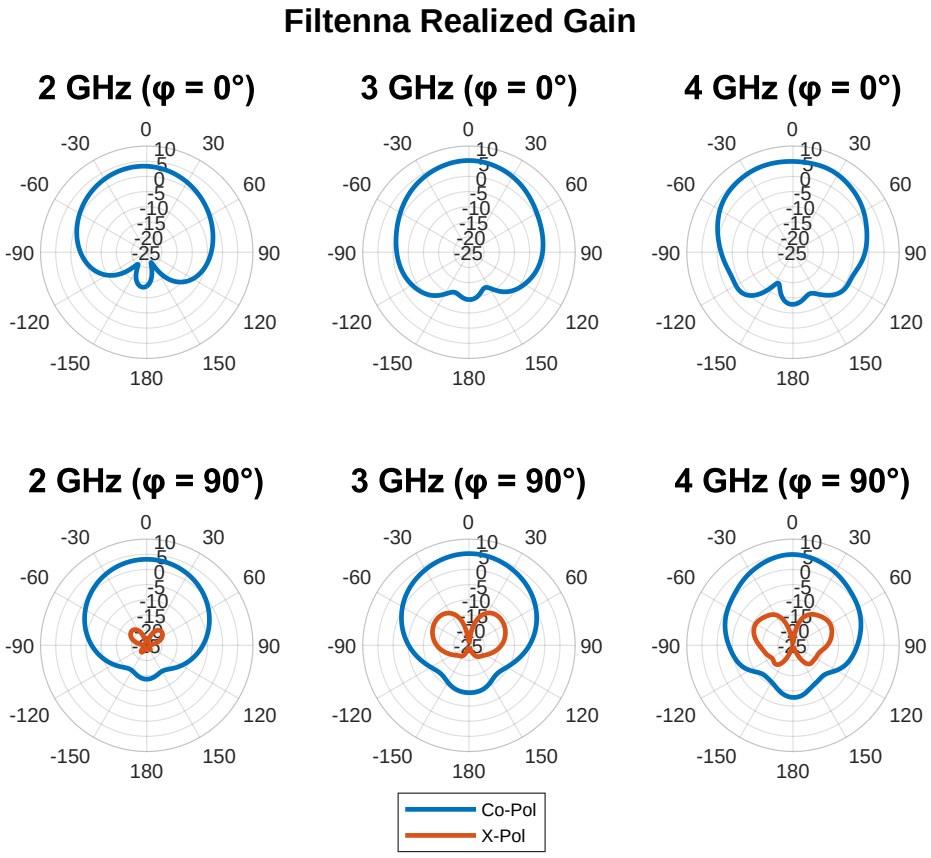

Figure 5.33: Realized gain patterns at 2, 3, and 4 GHz of the filtenna. Includes co-polarization and cross-polarization cuts, high polarization purity in the $\varphi = 0°$ cut plane (X-Pol is always below -25 dBi, so it is not visible) but low polarization purity in the $\varphi = 90°$ cut plane.

Table 5.3: Summary of broadside realized gain values for the filtenna across frequency, including co and cross polarization.

	2 GHz	3 GHz	4 GHz
Realized Gain Co-Pol ($\theta = 0°$)	3.34 dBi	5.22 dBi	4.92 dBi
Realized Gain X-Pol ($\theta = 0°$)	-46.61 dBi	-53.56 dBi	-40.05 dBi
Realized Gain Co-Pol ($\theta = 180°$)	-13.84 dBi	-9.39 dBi	-7.83 dBi
Realized Gain X-Pol ($\theta = 180°$)	-41.92 dBi	-52.64 dBi	-46.38 dBi

Following the analysis of radiation pattern and match, radiation efficiency was investigated as a figure of merit, shown in Figure 5.34. As with the previous antenna, the minimum radiation efficiency occurs at the highest loading, reaching a minimum of 66.83% at 2 GHz. The radiation efficiency increases as the antenna is tuned across S-band, eventually reaching a maximum of 87.01% radiation efficiency at 4 GHz. This is slightly less than the cavity backed antenna, contributing to the slightly decreased realized gain at 4 GHz.

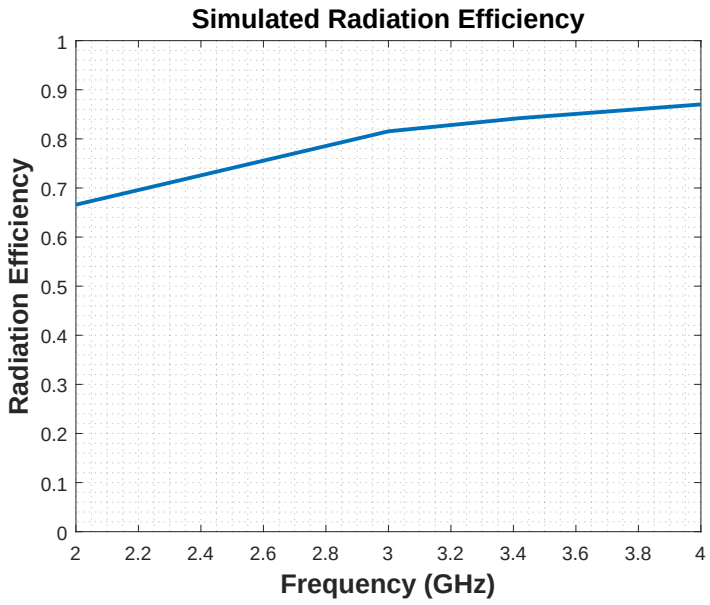

Figure 5.34: Course simulated radiation efficiency of the filtenna over the 2-4 GHz tuning range. The filtenna demonstrated a minimum of 66.59% radiation efficiency and a maximum of 87.01% radiation efficiency.

In summary, the filtenna was able to tune across all of S-band while maintaining high radiation efficiency, high gain, and a patch-like pattern. The realized gain remained above 3 dBi at broadside throughout all tuning ranges the entire band, getting as high as 5.2 dBi in the center of the band. The performance of the filtenna across S-band is depicted in Figure 5.32.

5.5.3 Transmission Zero at 3.42 GHz

As can be seen in Figure 5.32, there is a persistent 'zero' in realized gain at 3.42 GHz. To make sure this did not cause problem in the performance of the filtenna, the filtenna was tuned to a center frequency of 3.42 GHz. The resulting S_{11} and realized gain plots can be seen in Figure 5.35.

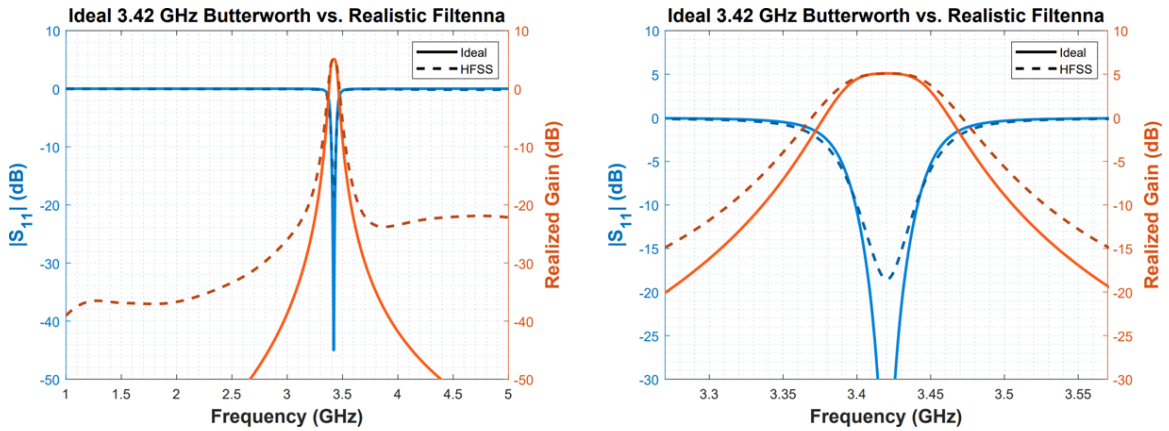

Figure 5.35: 2 GHz (a) and 4 GHz (b) S_{11} response of filtenna with broadside realized gain over frequency compared to an ideal filter with finite Q, zoomed in on the pass-band.

Notably, the response seems entirely unaffected by the realized gain zero present in the other frequency responses. Therefore, the effect is causing the zero is likely small. Additionally, the zero only appeared when the filtenna model was transitioned to a fully realistic model with vias and copper thickness. This supports a theory that some leakage interaction is causing the zero in realized gain.

As for the design, it is more broadband in realized gain than ideal due to over-coupling, resulting in a 2.36% 3-dB fractional bandwidth. This was expected since the frequency is higher than 3 GHz, meaning the coupling structures are electrically large. The response also has a slightly worse than ideal match across the passband due to the coupling errors, and this is reflected as a different than ideal S_{11}. However, the calculated center frequency from the 3-dB points is 3.42 GHz, exactly at the designed center frequency.

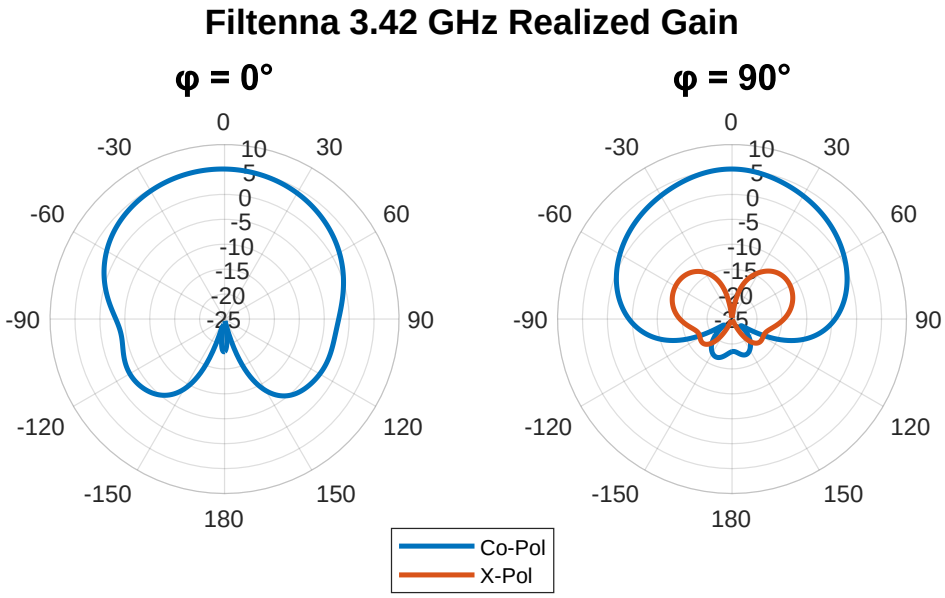

Figure 5.36: Realized gain patterns at 3.42 GHz of the filtenna. Includes co-polarization and cross-polarization cuts, high polarization purity in the $\varphi = 0°$ cut plane (X-Pol is always below -25 dBi, so it is not visible) but low polarization purity in the $\varphi = 90°$ cut plane.

Addionally, the radiation pattern at 3.42 GHz looks patch-like, shown in Figure 5.36. The broadside realized gain at $\theta = 0°$ is 5.0846 dBi in the co-polarization, and -65.1146 dBi in the cross-polarization. The broadside realized gain at $\theta = 180°$ is -18.4545 dBi in the co-polarization, and -47.5870 dBi in the cross-polarization. The 3.42 GHz pattern is notable in that at $\theta = 180°$ it has quite a deep radiation null. In general, the back radiation of the filtenna tuned to 3.42 GHz is much less than that seen at other frequencies.

5.5.4 Power Handling Investigation

As done previously, an investigation into the power handling of the filtenna was completed to determine its feasibility within a high-power setup. A Driven Modal simulation was used to find the maximum electric field strength in the design, again with input power of

1 W. The fields were extracted from the center of each of the capacitive gaps to limit simulation artifacts that result in unrealistic peaks in electric field at sharp conductor/dielectric boundaries.

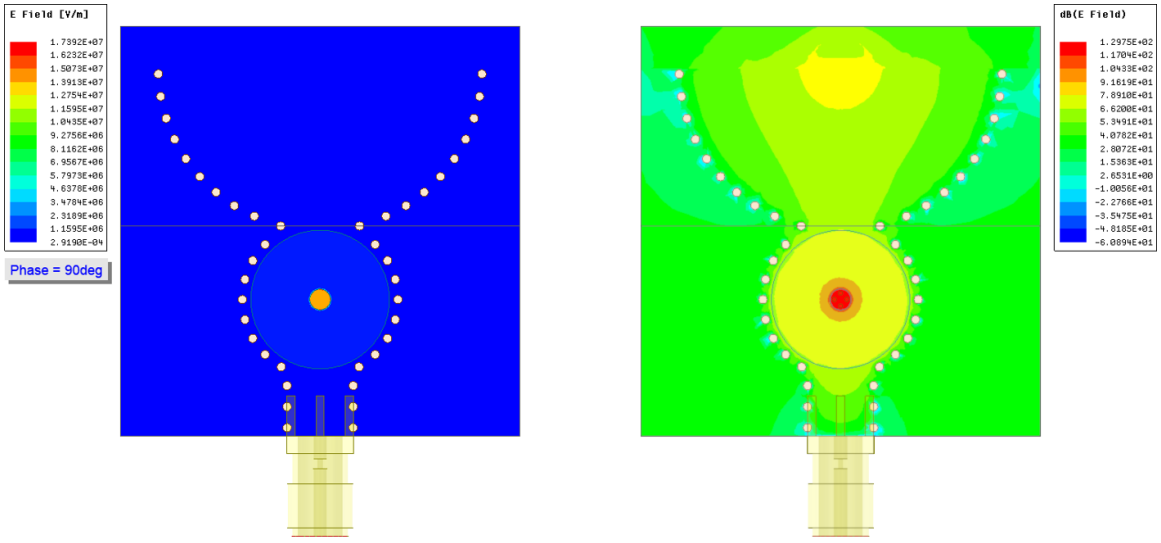

(a) (b)

Figure 5.37: Electric field strength and distribution in a filtenna tuned to 2 GHz. The electric fields are represented in V/m (a) and in dB of V/m (b), highlighting the large concentration of fields in the capacitive gap in cavity and the capacitive gap in the antenna.

The resulting field distribution at 2 GHz can be seen in Figure 5.37. The electric field energy is highly concentrated in the capacitive gap of the evanescent-mode cavity, and is correspondingly the location of highest field strength. The strength of the electric field in the capacitive gap of the antenna is an order of magnitude less than that in the cavity, reflecting the order of magnitude difference in gap size. The maximum electric field in the capacitive gap of the cavity was 17.3920 V/µm at 2 GHz, 3.7493 V/µm at 3 GHz, and 1.8235 V/µm at 4 GHz.

As before, (3.1) was used to scale the power to breakdown. The maximum power handling was predicted to be 0.2063 W (23.1456 dBm) at 2 GHz, 4.4397 W (36.4735 dBm)

at 3 GHz, and 18.7691 W (42.7344 dBm) at 4 GHz. Again, the power handling increases exponentially with frequency, leading to a rapid decrease in power handling for a highly loaded antenna. Notably, these power handling predictions are different than the predictions of the cavity by itself. The lower power handling prediction at 2 GHz (23.1 dBm filtenna vs. 29.1 dBm cavity) is due to the smaller gap size (7.84 μm filtenna vs. 8.4 μm cavity), the slightly smaller post radius (1.00 mm filtenna vs. 1.05 mm cavity), and the smaller bandwidth of the filtenna (1.43% FBW filtenna vs. 2.00% cavity). The slight increase in power handling prediction at 3 GHz (36.5 dBm filtenna vs. 36.0 dBm cavity) is likely due to a decrease in quality factor of the cavity from coupling into the antenna (630 filtenna vs. 700 cavity). The increase in power handling prediction at 4 GHz (42.7 dBm filtenna vs. 42.0 dBm cavity) is due to the decrease in quality factor and the larger bandwidth of the filtenna (2.82% FBW filtenna vs. 2.00% FBW cavity).

5.6 Conclusions

Tunable filtenna design previously relied on a large amount of trial and error to create a functional device. This created a problem both in limiting the achievable performance of a filtenna, but also in the large amount of time necessary to create and tune any given filtenna. Adding onto that the challenge of tunability, and the entire process becomes prohibitively time intensive. This limitation drastically reduces the feasibility of filtennas despite their various promises.

To address these concerns, filter design theory was applied to filtenna design. Generation of ideal S_{11} curves for both the frequency and time domain was discussed. Derivation of filter parameters was also discussed, as well as ways to extract them from a filtenna in simulation. Characterization of various filtenna structures was also shown, enabling tuning of the individual filtenna sub-structures with knowledge of how those adjustments will af-

fect the filtenna at large. Time domain tuning was applied to the filtenna, and the results agreed particularly well with ideal results. The filtenna was predicted to handle greater than 23 dBm across the entire tuning range, up to a maximum of 42 dBm at 4 GHz. Ultimately, a design process for a filtenna has been demonstrated that shows great promise in simulation.

Chapter 6

Conclusions and Future Work

6.1 Conclusions

Considering the increasing demands of RF systems, such as increased density of bands and the need for multi-band operation, higher performing RF systems are needed. While traditional systems of wideband antennas followed by a switchable filter bank offer an intermediary step, the large SWaP increases that come with those systems are undesirable.

Tunable systems offer a step in the right direction, and there has been much research into the creation of tunable antennas and tunable filters. Tunable antennas allow for improvements in rejection characteristics, and tunable filters allow for the replacement of a filter bank with a single tunable filter. However, one final step can be taken to further improve the SWaP concerns of these devices while maintaining all the rejection benefits and multi-band behavior so desired in modern RF systems. This step is a filtenna, which is a combined filtering and radiating device. If designed correctly, a filtenna can offer better noise figure performance and low SWaP compared to almost any other system, all while maintaining the same desired frequency response.

In this thesis, the building blocks of an example filtenna have been demonstrated. Theory, simulation, and fabrication of an evanescent-mode cavity was performed, demonstrating its feasibility in maintaining high Q while also offering a wide tuning range. A tunable

antenna was also demonstrated, again also showing high tunability while maintaining desirable radiation characteristics and match. Finally, the elements were combined to create a filtenna, with a discussion of applying filter theory, coupling considerations, and a time domain tuning method all presented in detail. The time domain tuning method showed high competence in tuning the filtenna to specification across a wide range of frequencies. The TD tuning method allowed accurate tuning despite only having access to S_{11}, an essential trait for rapidly tuning filtennas. The filtenna showed very close to the prescribed filter frequency response at the designed frequency. The filtenna was also simulated to tune widely, tuning from 2-4 GHz while maintaining above 65% radiation efficiency and above 3.3 dBi realized gain across the entire tuning range.

6.2 Scientific Impact

While the time domain tuning method had been applied to filtennas before, this was the first time it was applied to tunable filtennas. The method proved to be robust in predicting the radiation frequency characteristics of the filtenna with only access to S_{11}. The method was discussed in detail and is widely applicable and will make future development of tunable filtennas much simpler.

Additionally, a series of novel tunable antenna designs were presented, each an improvement on the last. All were able to tune widely (2:1 tuning ratio), with the final design capable of coupling into evanescent-mode cavities to enable filtenna design. The second iteration of the antenna was fabricated and measured, demonstrating that the device performs similarly to simulation and meets expectations.

Lastly, for the first time, the feasibility of a widely tunable, high-power handling, multi-order filtenna was shown in simulation. While this particular filtenna was not predicted to handle many Watts of power, changing of the evanescent mode cavity design would allow

for much higher power handling. Additionally, this filtenna was the first demonstrated to maintain high radiation efficiency, high gain, and boast a 2:1 tuning ratio. As stated before, a method of going from conceptualization to finished filtenna was outlined, with characterization of various coupling structures, resonators, and tuning trade-offs shown in detail. This will serve as a guide for future designers wishing to make a filtenna to serve their own unique purposes.

6.3 Future Work

When it comes to future work, there are many interesting tangents one could explore. For evanescent-mode cavities, a closed-form method of predicting the quality factor of the cavity, including dielectric loss, would be of high use. Previous work has looked at optimizing Q based on the ratio between the radius of the cavity and the radius of the post [12], but that work has not been extended to the case where the cavity contains a dielectric stack. This would allow for maximum Q cavities to be developed without the need for simulation sweeps to determine the best ratio of values.

For tunable antennas, investigations into limitations of radiation efficiency at higher loading should be performed, as there appears to be a 'knee' in the radiation efficiency plots that could be investigated and explained. Additionally, it is unknown what factors affect the external Q of any antenna. In antenna theory, antennas are treated as having a singular Q, but when filter theory is applied, there are three different quality factors in the system. The properties of the unloaded antenna control Q_u, the feeding mechanism controls the input coupling Q, but it is a mystery what affects the output coupling Q. Characterization of those factors that affect the output coupling Q would be helpful in developing a theory of antenna output coupling. This would open the door to adjusting output coupling, enabling the creation of any arbitrary bandwidth filtenna within the bounds of parameter control.

For the tunable filtenna shown, it should be fabricated and measured to verify simulated results. The evanescent-mode cavity design should be investigated further, ideally with an altered mechanical actuation mechanism to allow for a wider movement range. This would enable a larger starting gap and rapidly increase the power handling capability of the filtenna. Additionally, future work should focus on adding tuning mechanisms to the input and inter-resonator coupling, allowing for the performance at 2 and 4 GHz to be improved drastically. If the output coupling could also be characterized and tuned, the filtenna would be capable of tuning to any arbitrary frequency with any arbitrary filter response. This agile filtenna could be combined with an assessment method based on TD tuning, allowing for a feedback loop to automatically and quickly tune the filtenna to the desired response. It would be unrivaled as a bandwidth and frequency agile antenna with low SWaP, high linearity, and high power handling capability.

Further in the future, the filtenna could be redesigned to improve polarization purity and then incorporated into a dual-polarized phased array. This would allow for am extremely agile radiating element that is reconfigurable in frequency, bandwidth, radiation pattern, and polarization, all while maintaining comparatively low SWaP. An element that capable would open the door for many high performance applications.

References

[1] U.S. Department of Commerce, National Telecommunications and Information Administration, Office of Spectrum Management, *United states frequency allocations: The radio spectrum*, ntia.doc.gov, https://www.ntia.doc.gov/files/ntia/publications/january_2016_spectrum_wall_chart.pdf (accessed 28 July 2020).

[2] H. W. Jones, "The recent large reduction in space launch cost", in *48th International Conference on Environmental Systems (ICES)*, NASA, Jul. 2018.

[3] J. Uher and W. Hoefer, "Tunable microwave and millimeter-wave band-pass filters", *IEEE Transactions on Microwave Theory and Techniques*, vol. 39, no. 4, pp. 643–653, Apr. 1991. DOI: 10.1109/22.76427.

[4] H. Joshi, H. Sigmarsson, S. Moon, D. Peroulis, and W. Chappell, "High-Q fully reconfigurable tunable bandpass filters", *IEEE Transactions on Microwave Theory and Techniques*, vol. 57, no. 12, pp. 3525–3533, Dec. 2009. DOI: 10.1109/tmtt.2009.2034309.

[5] D. M. Pozar, *Microwave Engineering*. Wiley, 2011.

[6] S. Moon, H. H. Sigmarsson, H. Joshi, and W. J. Chappell, "Substrate integrated evanescent-mode cavity filter with a 3.5 to 1 tuning ratio", *IEEE Microwave and Wireless Components Letters*, vol. 20, no. 8, pp. 450–452, Aug. 2010. DOI: 10.1109/lmwc.2010.2050680.

[7] S. Saeedi, J. Lee, and H. Sigmarsson, "Prediction of power handling in tunable, high-Q, substrate-integrated, evanescent-mode cavity bandpass filters", *Electronics Letters*, vol. 52, no. 10, pp. 846–848, May 2016. DOI: 10.1049/el.2016.0567.

[8] S. M. Hou, J. H. Lang, A. H. Slocum, A. C. Weber, and J. R. White, "A high-Q widely tunable gigahertz electromagnetic cavity resonator", *Journal of Microelectromechanical Systems*, vol. 15, no. 6, pp. 1540–1545, Dec. 2006. DOI: 10.1109/jmems.2006.879709.

[9] H. Joshi, H. H. Sigmarsson, D. Peroulis, and W. J. Chappell, "Highly loaded evanescent cavities for widely tunable high-Q filters", in *2007 IEEE/MTT-S International Microwave Symposium*, IEEE, Jun. 2007. DOI: 10.1109/mwsym.2007.380346.

[10] K. Entesari, A. P. Saghati, V. Sekar, and M. Armendariz, "Tunable SIW structures: Antennas, VCOs, and filters", *IEEE Microwave Magazine*, vol. 16, no. 5, pp. 34–54, Jun. 2015. DOI: 10.1109/mmm.2015.2408273.

[11] K. Fujisawa, "General treatment of klystron resonant cavities", *IEEE Transactions on Microwave Theory and Techniques*, vol. 6, no. 4, pp. 344–358, Oct. 1958. DOI: 10.1109/tmtt.1958.1125205.

[12] S. Saeedi, "Frequency-agile microwave filters for radars with simultaneous transmission and reception", PhD Dissertation, University of Oklahoma, 2015.

[13] N. Behdad and K. Sarabandi, "Dual-band reconfigurable antenna with a very wide tunability range", *IEEE Transactions on Antennas and Propagation*, vol. 54, no. 2, pp. 409–416, Feb. 2006. DOI: 10.1109/tap.2005.863412.

[14] A. Khidre, F. Yang, and A. Z. Elsherbeni, "A patch antenna with a varactor-loaded slot for reconfigurable dual-band operation", *IEEE Transactions on Antennas and Propagation*, vol. 63, no. 2, pp. 755–760, Feb. 2015. DOI: 10.1109/tap.2014.2376524.

[15] B. Cetiner, G. Crusats, L. Jofre, and N. Biyikli, "RF MEMS integrated frequency reconfigurable annular slot antenna", *IEEE Transactions on Antennas and Propagation*, vol. 58, no. 3, pp. 626–632, Mar. 2010. DOI: 10.1109/tap.2009.2039300.

[16] F. Yang and Y. Rahmat-Samii, "Patch antennas with switchable slots (PASS) in wireless communications: Concepts, designs, and applications", *IEEE Antennas and Propagation Magazine*, vol. 47, no. 2, pp. 13–29, Apr. 2005. DOI: 10.1109/map.2005.1487774.

[17] J.-S. Row, W.-L. Liu, and T.-R. Chen, "Circular polarization and polarization reconfigurable designs for annular slot antennas", *IEEE Transactions on Antennas and Propagation*, vol. 60, no. 12, pp. 5998–6002, Dec. 2012. DOI: 10.1109/tap.2012.2211556.

[18] C.-Y.-D. Sim, T.-Y. Han, and Y.-J. Liao, "A frequency reconfigurable half annular ring slot antenna design", *IEEE Transactions on Antennas and Propagation*, vol. 62, no. 6, pp. 3428–3431, Jun. 2014. DOI: 10.1109/tap.2014.2314314.

[19] G. Marconi, "Transmitting electrical signals", U.S. Patent 586 193, Jul. 13, 1897.

[20] M. Yu, B. Yassini, B. Keats, and Y. Wang, "The sound the air makes: High-performance tunable filters based on air-cavity resonators", *IEEE Microwave Magazine*, vol. 15, no. 5, pp. 83–93, Jul. 2014. DOI: 10.1109/mmm.2014.2321102.

[21] Y. Yusuf and X. Gong, "Compact low-loss integration of high-Q 3-D filters with highly efficient antennas", *IEEE Transactions on Microwave Theory and Techniques*, vol. 59, no. 4, pp. 857–865, Apr. 2011. DOI: 10.1109/tmtt.2010.2100407.

[22] B. Froppier, Y. Mahe, E. M. Cruz, and S. Toutain, "Integration of a filtering function in an electromagnetic horn", in *33rd European Microwave Conference, 2003*, IEEE, Oct. 2003. DOI: 10.1109/euma.2003.341117.

[23] G. Q. Luo, W. Hong, H. J. Tang, J. X. Chen, X. X. Yin, Z. Q. Kuai, and K. Wu, "Filtenna consisting of horn antenna and substrate integrated waveguide cavity FSS", *IEEE Transactions on Antennas and Propagation*, vol. 55, no. 1, pp. 92–98, Jan. 2007. DOI: 10.1109/tap.2006.888459.

[24] H. Cheng, Y. Yusuf, and X. Gong, "Vertically integrated three-pole filter/antennas for array applications", *IEEE Antennas and Wireless Propagation Letters*, vol. 10, pp. 278–281, 2011. DOI: 10.1109/lawp.2011.2135833.

[25] Y. Yusuf, H. Cheng, and X. Gong, "A seamless integration of 3-d vertical filters with highly efficient slot antennas", *IEEE Transactions on Antennas and Propagation*, vol. 59, no. 11, pp. 4016–4022, Nov. 2011. DOI: 10.1109/tap.2011.2164186.

[26] R. Lovato and X. Gong, "A third-order SIW-integrated filter/antenna using two resonant cavities", *IEEE Antennas and Wireless Propagation Letters*, vol. 17, no. 3, pp. 505–508, Mar. 2018. DOI: 10.1109/lawp.2018.2799518.

[27] R. E. Lovato, T. Li, and X. Gong, "Tunable filter/antenna integration with bandwidth control", *IEEE Transactions on Microwave Theory and Techniques*, vol. 67, no. 10, pp. 4196–4205, Oct. 2019. DOI: 10.1109/tmtt.2019.2931560.

[28] Y. Tawk, J. Costantine, and C. G. Christodoulou, "A varactor-based reconfigurable filtenna", *IEEE Antennas and Wireless Propagation Letters*, vol. 11, pp. 716–719, 2012. DOI: 10.1109/lawp.2012.2204850.

[29] H. Nachouane, A. Najid, F. Riouch, and A. Tribak, "Electronically reconfigurable filtenna for cognitive radios", *Microwave and Optical Technology Letters*, vol. 59, no. 2, pp. 399–404, Dec. 2016. DOI: 10.1002/mop.30299.

[30] M. Mahatme and M. S. Narlawar, "Reconfigurable filtenna in UHF band for cognitive radio application", in *2016 World Conference on Futuristic Trends in Research and Innovation for Social Welfare (Startup Conclave)*, IEEE, Feb. 2016. DOI: 10.1109/startup.2016.7583946.

[31] R. Lovato and X. Gong, "A tunable SIW integrated filter/antenna", in *2017 IEEE International Symposium on Antennas and Propagation & USNC/URSI National Radio Science Meeting*, IEEE, Jul. 2017. DOI: 10.1109/apusncursinrsm.2017.8073133.

[32] D. Peroulis, E. Naglich, M. Sinani, and M. Hickle, "Tuned to resonance: Transfer-function-adaptive filters in evanescent-mode cavity-resonator technology", *IEEE Microwave Magazine*, vol. 15, no. 5, pp. 55–69, Jul. 2014. DOI: 10.1109/mmm.2014.2321103.

[33] D. Deslandes and K. Wu, "Accurate modeling, wave mechanisms, and design considerations of a substrate integrated waveguide", *IEEE Transactions on Microwave Theory and Techniques*, vol. 54, no. 6, pp. 2516–2526, Jun. 2006. DOI: 10.1109/tmtt.2006.875807.

[34] A. Semnani, A. Venkattraman, A. Alexeenko, and D. Peroulis, "Numerical evaluation of RF gas ionization effects in micro-and nano-scale devices", in *2012 International Conference on Electromagnetics in Advanced Applications*, IEEE, Sep. 2012. DOI: 10.1109/iceaa.2012.6328741.

[35] A. Semnani, A. Venkattraman, A. A. Alexeenko, and D. Peroulis, "Pre-breakdown evaluation of gas discharge mechanisms in microgaps", *Applied Physics Letters*, vol. 102, no. 17, p. 174 102, Apr. 2013. DOI: 10.1063/1.4803179.

[36] K. Chen, A. Semnani, and D. Peroulis, "High-power microwave gas discharge in high-Q evanescent-mode cavity resonators and its instantaneous/long-term effects", in *2013 IEEE MTT-S International Microwave Symposium Digest (MTT)*, IEEE, Jun. 2013. DOI: 10.1109/mwsym.2013.6697759.

[37] W. Stutzman and G. Thiele, *Antenna Theory and Design*, ser. Antenna Theory and Design. Wiley, 2012.

[38] L. J. Chu, "Physical limitations of omni-directional antennas", *Journal of Applied Physics*, vol. 19, no. 12, pp. 1163–1175, Dec. 1948. DOI: 10.1063/1.1715038.

[39] New Scale Technologies, *Micro linear actuator*, NewScaleTech.com, https://www.newscaletech.com/micro-motion-modules/m3-l-linear-smart-actuators/ (accessed 6 July 2020).

[40] J. Dyson, "The equiangular spiral antenna", *IRE Transactions on Antennas and Propagation*, vol. 7, no. 2, pp. 181–187, Apr. 1959. DOI: 10.1109/tap.1959.1144653.

[41] N. Duangrit, B. Hong, A. D. Burnett, P. Akkaraekthalin, I. D. Robertson, and N. Somjit, "Terahertz dielectric property characterization of photopolymers for additive manufacturing", *IEEE Access*, vol. 7, pp. 12 339–12 347, 2019. DOI: 10.1109/access.2019.2893196.

[42] Forecase 3D, *Sla materials*, Forecast3D.com, https : / / www . forecast3d . com / materials/sla (accessed 6 July 2020).

[43] RF Cafe, *Dielectric constant, strength, & loss tangent*, RFCafe.com, https://www.rfcafe . com / references / electrical / dielectric - constants - strengths . htm (accessed 6 July 2020).

[44] J. Dunsmore, "Tuning band pass filters in the time domain", in *1999 IEEE MTT-S International Microwave Symposium Digest (Cat. No.99CH36282)*, IEEE. DOI: 10.1109/mwsym.1999.779638.

[45] S. Burger and M. Hoeft, "Improved filter tuning in the time domain", in *2014 1st Australian Microwave Symposium (AMS)*, IEEE, Jun. 2014. DOI: 10.1109/ausms.2014.7017349.

[46] J.-S. Hong and M. J. Lancaster, *Microstrip Filters for RF/Microwave Applications*. John Wiley & Sons, Inc., Jun. 2001. DOI: 10.1002/0471221619.

[47] H. Sigmarsson, "Microwave filter class lecture", University of Oklahoma Lecture, 2019.

[48] E. J. Naglich, "Filter synthesis and design techniques for highly adaptable systems", PhD Dissertation, Purdue University, 2013.

[49] Microwaves101, *Polarization*, Microwaves101.com, https://www.microwaves101.com/encyclopedias/polarization (accessed 30 July 2020).

Appendix A

MATLAB Code

A.1 g-Coefficient Code

```
% Returns g-coefficients of desired filter in matrix
% ASSUMES BUTTERWORTH UNLESS OPTIONAL INPUTS ARE GIVEN
% Required Inputs:
%   n:      order of filter
% Optional Inputs (but still have to be in order)
%   type:   type of measurement for Chebyshev
%           RL = return loss, PR = passband ripple
%   ripple: max allowed ripple in return loss or passband (dB)
function g_coef = getGCoef(n,type,ripple)
    if nargin == 1 % Do Butterworth stuff
        g_coef = zeros(n+2,1);
        g_coef([1 end]) = 1; % set g_0 and g_n to 1
        g_coef(2:end-1) = 2*sin((2*(1:n) - 1)*pi./(2*n));
    elseif nargin == 3  % Do Chebyshev stuff
        g_coef = zeros(n+2,1);get
        g_coef(1) = 1; % set g_0 to 1
        switch type % obtain epsilon value
            case 'RL'
                eps = sqrt(1/(10^(ripple/10) - 1));
            case 'PR'
                eps = sqrt(10^(ripple/10) - 1);
            otherwise
                error('getGCoef: Unrecognized ripple type');
        end
        eta = sinh((1/n) * asinh(1/eps));
        g_coef(2) = (2/eta) * sin(pi/(2*n)); % find g_1
        for r = 1:n-1 % calculate the rest of the g values
            g_coef(r+2) = 4*sin((2*r-1)*pi/(2*n))*sin((2*r+1)*pi/...
                (2*n))/((eta^2 + sin(r*pi/n)^2) * g_coef(r+1));
```

```
        end
        if mod(n,2) == 1 % check even/odd-ness of n
            g_coef(n+2) = 1; % n is odd
        else % n is even
            g_coef(n+2) = (eps + sqrt(1+eps^2))^2;
        end
    else
        error('getGCoef: unrecognized number of inputs');
    end
end
```

A.2 Prototype S-Parameter Code

```
% Returns complex S-parameters of desired filter in S-parameter object.
% Band pass filters only.
% ASSUMES 50 OHM SYSTEM IMPEDANCE
% Required Inputs:
%   f0:     center frequency of filter (Hertz)
%   FBW:    fractional bandwidth of filter (expressed as a decimal)
%   n:      order of filter
%   fSweep: array of frequency points to sweep over
%   type:   type of filter
%               BUTT = Butterworth
%               C_RL = Chebyshev, Return Loss Specified
%               C_PR = Chebyshev, Passband Ripple Specified
% Optional Inputs (but still have to be in order)
%   Qu:     unloaded Q of the various resonators of the filter. Can be an
%           array of length n or a single value for all the resonators
function s_params = protoSParams(f0,FBW,n,fSweep,type,Qu,ripple)
    if nargin < 5
        error('protoSParams: f0, FBW, n, fSweep, and type are  all
            required inputs');
    end
    if nargin < 6
        Qu = Inf(1,n);  % 1/Inf in MATLAB returns 0 (what we want later)
    elseif numel(Qu) == 1
        Qu = repmat(Qu,1,n);
    elseif numel(Qu) ~= n
        error('protoSParams: The length of Qu must be 1 or match n');
    end

    switch type % check filter type
        case 'BUTT'
```

```
30            if nargin == 7
31                warning('protoSParams: Butterworth does not have a ripple
                      value. Ignoring.');
32            end
33            g_coef = getGCoef(n); % get g-coefficients with given order
34        case 'C_RL'
35            if nargin ~= 7
36                error('protoSParams: Chebyshev Return Loss specified is
                      lacking the correct number of inputs');
37            end
38            g_coef = getGCoef(n,'RL',ripple);
39        case 'C_PR'
40            if nargin ~= 7
41                error('protoSParams: Chebyshev Passband Ripple specified
                      is lacking the correct number of inputs');
42            end
43            g_coef = getGCoef(n,'PR',ripple);
44        otherwise
45            error('protoSParams: Unrecognized filter type');
46    end
47
48    % create empty s-parameter data matrix
49    sData = complex(zeros(2,2,length(fSweep)),zeros(2,2,length(fSweep)));
50
51    R = zeros(n+2,n+2);
52    SU = zeros(n+2,n+2);
53    M = zeros(n+2,n+2);
54    A_inv = zeros(n+2,n+2);
55
56    R(1,1) = 1;
57    R(n+2,n+2) = 1;
58
59    % Find S across frequency
60    if(f0 ~= 0)
61        normFreqs = 1/FBW * (fSweep/f0 - f0./fSweep);
62    else
63        normFreqs = 1/FBW * fSweep;
64    end
65    S = 1i*normFreqs;
66
67    % adjustment for finite Qu (d = 1/(FBW*Qu))
68    d = 1./(FBW*Qu);
69
70    % Find M assuming no self coupling and only mainline coupling
71    M(sub2ind(size(M),2:n+2,1:n+1)) = ...
```

```
        1i./sqrt(g_coef(1:end-1).*g_coef(2:end));
    M = M + M.';

    % Find A matrix
    for i=1:length(fSweep)
        SU(sub2ind(size(SU),2:n+1,2:n+1)) = S(i) + d;

        A_inv = inv(R + SU + M);

        % H's lecture slide equation
        sData(1,1,i) = 1-2*A_inv(1,1);
        sData(1,2,i) = 2*A_inv(1,n+2);
        sData(2,1,i) = 2*A_inv(n+2,1);
        sData(2,2,i) = 1-2*A_inv(n+2,n+2);
    end

    s_params = sparameters(sData,fSweep);
end
```

A.3 IDFT Code

```
% Returns complex, windowed IDFT of S-parameters
% Inputs:
%   f0:         center frequency of filter (Hertz)
%   fSweep:     vector of frequency points to sweep over (Hertz)
%   S11:        complex vector of linear S11 frequency response
%   oversample: multiplier on sampling rate to interpolate between points
% Optional Inputs:
%   timebounds: array of bounds on time domain sweep (seconds). Defaults
    to
%               assuming time starts at zero and max time is calculated
%   window:     window array to be used to reduce lobes in the system.
%               Defaults to Nuttall-defined Blackman-Harris window
% Outputs:
%   t:  time vector of points generated (seconds)
%   g:  IDFT vector of S11
%   ts: time vector of slope points generated (seconds)
%   s:  slope of phase response of time domain of S11
function [t,g,ts,s] = getIDFT(f0,fSweep,S11,oversample,timebounds,window)
    if (length(fSweep) == length(S11))
        N = length(fSweep);
    else
        error('getIDFT: frequency and S11 vector must be the same length'
            );
```

```
22      end
23
24      if(size(fSweep,1) == 1) % transpose fSweep if it's a row vector
25          fSweep = fSweep.';
26      end
27
28      if(size(S11,1) == 1) % transpose fSweep if it's a row vector
29          S11 = S11.';
30      end
31
32      % Check to see if center frequency is at center of frequency band
33      if(mod(N,2)) % frequency vector has an odd number of components
34          if(fSweep((N+1)/2) == f0)
35              disp(['Center of frequency vector for AWR aligned
                    appropriately at '...
36                   num2str(f0,'%.4e') ' Hz']);
37          elseif(f0 > fSweep(1) && f0 < fSweep(end))
38              error(['getIDFT: Center of frequency vector for AWR NOT
                    aligned. '...
39                   'Center of vector is ' num2str(fSweep((N+1)/2),'%.4e')
                        ...
40                   ' Hz when it should be at ' num2str(f0,'%.4e') ' Hz']);
41          end
42      else % frequency vector has an even number of components
43          if(mean(fSweep(N/2 + [0 1])) == f0)
44              disp(['Center of frequency vector for AWR aligned
                    appropriately at '...
45                   num2str(f0,'%.4e') ' Hz']);
46          else
47              error(['getIDFT: Center of frequency vector for AWR NOT
                    aligned. Center of '...
48                   'vector is ' num2str(mean(fSweep(N/2 + [0 1])),'%.4e') '
                        Hz '...
49                   'when it should be at ' num2str(f0,'%.4e') ' Hz']);
50          end
51      end
52
53      % Create Window (defaults to Nuttall-defined Blackman-Harris window)
54      if(nargin == 6)
55          if(length(window) == N)
56              W = window;
57          else
58              error('getIDFT: frequency and window vector must be the same
                    length');
59          end
```

```
    else
        W = nuttallwin(N); % default
    end

    % Multiply S11 with the Hamming Window
    G = S11.*W;

    % Create an appropriate Time Vector
    BW = fSweep(end) - fSweep(1);
    if(nargin == 4)
        maxTime = (N-1)/BW;
        t = 0:1/(BW*oversample):maxTime;
    elseif(or(nargin == 5,nargin == 6))
        t = timebounds(1):1/(BW*oversample):timebounds(end);
    else
        error('getIDFT: Incorrect number of inputs');
    end

    % Assuming frequency is a column vector and time is a row vector
    % (freq .* t) will return a Nf by Nt sized matrix
    % W will end up being your IDFT matrix
    % Subtract f0 to bring the signal down to baseband
    W = exp(1i*2*pi*(fSweep - f0).*t);

    % Multiply your signal with the IDFT matrix
    % Then sum along Dimension 1 to sum up along the frequency dimension
    % (done in matrix multiplication)
    % Lastly, divide by the number of frequency points
    g = (G.' * W) / N;
    % g = sum(G .* W , 1) / N;

    % Find slope of time domain
    phase = unwrap(angle(g.'));
    ts = t(1:end-1);
    s = -diff(phase)./diff(t).';
end
```